RUB

Study of Excited η Mesons in Photoproduction at CLAS

vorgelegt von
Cathrina Sowa
geboren in Dortmund

What is especially striking and remarkable is that in
fundamental physics a beautiful or elegant theory is
more likely to be right
than a theory that is inelegant.

--Murray Gell-Mann--

Abstract

The results presented in this work allow for new insights into the production of excited η mesons in photon-proton collisions measured with the CLAS detector. Results are presented for a meson of mass m = $1280.1 \pm 0.4\,\mathrm{MeV/c^2}$ seen in the $\pi^+\pi^-\eta$ invariant mass spectrum. For this state a differential cross section for center-of-mass energies up to $3.35\,\mathrm{GeV}$ is determined. For the enhancement at the lower mass two mesons are candidates, the $f_1(1285)$ and the $\eta(1295)$. For none of them a differential cross section has been measured in photoproduction up to this center-of-mass energy before.

Results for the mass and the width as well as an interpretation of the decay angular distribution are presented in order to gain insight on the identity of the resonance at $1280\,\mathrm{MeV/c^2}$.

Furthermore, a significant contribution of a resonance with a mass of $1400\,\mathrm{MeV/c^2}$ has been detected. This resonance might be identified as $\eta(1405)$. With respect to specific models the $\eta(1405)$ is negotiated as a glueball. Therefore this resonance is of huge importance, as glueball production is expected to be suppressed in photoproduction. The differential cross section for center-of-mass energies from $2.35\,\mathrm{GeV}$ up to $3.35\,\mathrm{GeV}$ in bins of the cosine of the production angle is presented.

Contents

1 Introduction

1.1 The Standard Model of Particle Physics

Physicists have been driven by the desire to understand the nature of the world on the most fundamental level and they are still on their quest to achieve a deeper understanding of matter. To obtain this knowledge physicists began to aim a beam of accelerated particles at a suitable target material, called it a scattering experiment and measured the emerging products with a system of detectors.

Nowadays the experiments are becoming more and more sophisticated than ever before to enable the experimentalists' search for new particles and other states of matter. Nevertheless there are a lot of questions remaining.

A multitude of subatomic particles were found, demanding some kind of sorting or classification scheme. The easiest way to sort found states is by mass. Therefore, the lightest, non-composed particles, e.g. electron and its neutrino, became classified as *leptons*. A variety of states which are not fundamental particles, because they are made of quarks, were sorted in an additional class named *hadrons*, which derives from the Greek word for heavy or bulky.

The large group of hadrons requires further classification into hadrons with integer and half-integer spin. Those particles with half-integer spin are termed *baryons* from the Greek prefix *bary-*, including for example proton and neutron, because of their weight tending to be heavy. Hadrons with integer spin were named *mesons*, from the Greek prefix *meso-* meaning middle, due to their tendency to be of medium weight.

Hadrons can decay via three of the four fundamental forces of nature, the gravitation is negligible because it has a nearly infinitesimal influence on particles with low mass in comparison to the other forces: electromagnetism, the weak interaction and the strong nuclear force.

Leptons for example only interact by the weak nuclear force and electromagnetism. The strong nuclear force is responsible for holding protons and neutrons together into nuclei. It is named that way because it is the strongest force in nature. Decays via the strong nuclear force happen fast (approximately in the order of 10^{-24} s, compared to the weak interaction which may decay times up to seconds).

Radiative decays or decays involving photons occur because of the electromagnetic force, which is responsible for binding electrons in shells around nuclei as well.

Finally the weak interaction allows hadrons to decay into lepton pairs or conducts the β decay mode of radioactive atoms. Furthermore, the weak nuclear force allows flavored mesons, like kaons, to decay into a meson and leptonic pairs or just lepton pairs.

There are more mesons that decay via the weak interaction than mesons which decay via strong interactions, giving us evidence that they have something special in common. In 1964 Murray Gell-Mann proposed a revolutionary idea: the *quark model*. He proposed

that hadrons are composed of smaller fundamental particles called quarks. At first the model involved three quarks with the flavors: *up*, *down* and *strange*. These quarks got properties assigned like spin and electric charge. Later Sheldon Lee Glashow and James Borken predicted the existence of a fourth quark, the *charm* quark. The charm quark prompted a mass formula to calculate the masses of the known mesons correctly and was needed to explain the suppression of flavor-changing neutral currents (GIM mechanism). The two last quarks were found in 1977 and 1995 at the Fermilab, called *bottom* and *top*. Due to the spin of 1/2 which is carried by each quark they underlie Paulis exclusion principle, which states that no two identical fermions simultaneously occupy the same quantum state. Additional to this they have other various intrinsic properties like mass and color. They are grouped like the leptons in three generations including two quarks and two leptons each. The first contains the *up* and *down* and the e and ν_e, the second generation contains the next heavier ones, the *charm* and *strange* and the μ and its neutrino, while the third generation contains the last two quarks and the τ lepton and its neutrino. Up to now every search for a fourth generation had no positive result. Particles which contain higher generation quarks tend to decay to particles containing quarks of the first generation which leads to the circumstance that only quarks of the first generation exist in our everyday-world.

Last there are the so called gauge bosons which are the carrier of the fundamental forces. The Higgs field gives particles mass, while the symmetries controlling their interactions suggest they should be massless. The electromagnetic force is carried by the uncharged photon. The electromagnetic force has an infinite range because of the zero photon mass. But its strength decreases with increasing distance. The electroweak force is mediated by the $W^\pm$ and Z^0 bosons. The W bosons are charged and each other's antiparticle while the Z is uncharged and is its own antiparticle. The W bosons are capable of changing the quark charge and weak isospin. They can also change the quark flavor. The neutral Z boson can change the energy, momentum or spin of a quark. The Quantum-Electro-Dynamics (QED) is the first theory which includes quantum mechanics as well as special relativity and describes the interaction between photons and matter. In the 1970's the electroweak force was integrated into the theory. But for the description of strong interacting particles, another theory was needed.

The QCD features an analogon to the electric charge of the QED, the color. In contrast to QED there are three "charges" of color: blue, red and green. The carrier of the strong nuclear force are the gluons and the theory describes the interactions inside hadrons and between quarks. Gluons are massless particles and carry a color and an anti-color simultaneously. Following the SU(3) group theory they form a color octet and a singlet which is symmetrically build of all three colors and three anti-colors. As a carrier of the color charge they are the intermediaries between quarks and the color charge allows them to self-interact.

As mentioned before the power of the electromagnetic force decreases with increasing distance. In QCD a similar, but inverse, effect happens. For small distances between the quarks they do not feel the binding force. They are quasi free and this is called *asymptotic freedom*. It is possible to describe QCD in this scale perturbatively. If the distance between quarks increases the strong force raises.

If one pulls two quarks contained in a meson apart the strength of the gluon flux be-

tween them increases. If this distance increases over a threshold a new quark anti-quark pair is formed out of the vacuum. This leads to the observation that no quark can be observed alone and free, but only in bound states. This phenomenon is called *confinement*. Information about the structure of hadrons and their interactions can be gained by spectroscopy.

1.2 Meson Spectroscopy

One part of spectroscopy is the study of properties of quantum-mechanical states to understand their interactions with the goal to gain further knowledge about QCD in the non-perturbative regime. Hadron spectroscopy measures the masses and widths of bound quark systems and compares them to QCD predictions. More resonances have been found than mesons are predicted by theory. Mesons are build of a quark and an anti-quark and have to be further classified into light and heavy mesons due to their different quark contents and the consequential different behavior. The light mesons are assembled from the three lightest quarks: *up*, *down* and *strange*. Heavy mesons consist of at least one *charm* or *bottom* quark.

It is much easier to distinguish the mass states of the heavy meson spectrum from one another, because those states are well separated from one another. The masses of light mesons are often overlapping due to their often large width. Assuming that they carry the same quantum numbers it is allowed that $s\bar{s}$ states as well as $u\bar{u}$ and $d\bar{d}$ mix. It is possible to form nine different quark compositions from the three quarks and their anti-quarks, according to the SU(3) group theory. These nine compositions form an octet and a singlet. Those formations can be further sorted and classified with the help of their quantum numbers. Quarks are fermions, and therefore carry a spin of 1/2 hence they can couple to a total spin S of either 0 or 1.

Their complete set of quantum numbers is expressed in the spin parity notation J^{PC}, where J is the total angular momentum and can be calculated with $|L - S| \leq J \leq L + S$. L is the orbital angular momentum and S is the spin angular momentum.

The other two quantum-numbers P and C are the parity $P = (-1)^{L+1}$ and the charge conjugation $C = (-1)^{L+S}$. If the quark and anti-quark do not have a relative angular momentum to each other (L=0), only quantum numbers of $J^{PC} = 0^{-+}$ and $J^{PC} = 1^{--}$ are allowed. Mesons with a $J^{PC} = 0^{-+}$ are called pseudo-scalar mesons whereas mesons with $J^{PC} = 1^{--}$ are vector-mesons. The analysis of this thesis deals mostly with pseudo-scalar mesons thus the pseudo-scalar meson spectrum is explained furthermore. In figure 1.1 the pseudo-scalar meson nonet containing the ground states is shown. The quark component of the mesons of the nonet are listed below

$$\pi^+ = |u\bar{d}\rangle \qquad\qquad\qquad K^+ = |u\bar{s}\rangle$$
$$\pi^- = |\bar{u}d\rangle \qquad\qquad\qquad K^- = |\bar{u}s\rangle$$
$$\pi^0 = \frac{1}{\sqrt{2}}|u\bar{u} - d\bar{d}\rangle \qquad\qquad K^0 = |d\bar{s}\rangle$$
$$\overline{K}^0 = |\bar{d}s\rangle$$
$$\eta_1 = \frac{1}{\sqrt{3}}|d\bar{d} + u\bar{u} + s\bar{s}\rangle \qquad\qquad \eta_8 = \frac{1}{\sqrt{6}}|d\bar{d} + u\bar{u} - 2s\bar{s}\rangle$$
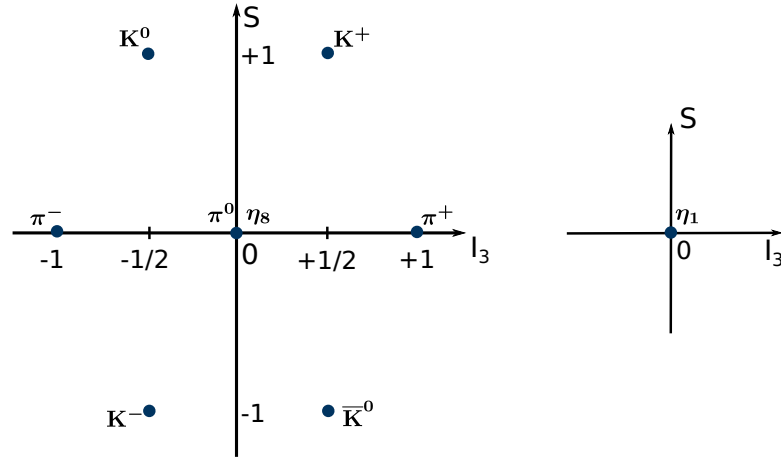
Figure 1.1: Nonet of lightest pseudoscalar mesons sorted by their strangeness S and the third component of Isospin I_3. Left: octet, Right: singlet.

The two wave-functions η_1 and η_8 mix to form the mesons η and η' and θ is the mixing angle.

$$\begin{pmatrix} \eta \\ \eta' \end{pmatrix} = \begin{pmatrix} cos(\theta) & -sin(\theta) \\ sin(\theta) & cos(\theta) \end{pmatrix} \begin{pmatrix} \eta_8 \\ \eta_1 \end{pmatrix}$$

The mixing angle of the pseudoscalar meson nonet is approximately $\theta = -11.5°$. Therefore, the observed particle η is near the η_8 and the η' is close to the η_1. Different meson nonets could be formed out of the same quark compositions as mentioned above. The only difference between them are the spin and angular momentum as well as radial excitations. An orbital angular momentum of larger than one and radial excitations of the valence quarks lead to different masses and decay characteristics.

As mentioned above, many of the predicted mesons were found as well as some additional resonances which do not fit into the underlying systematics and can not be integrated into one of the meson nonets. Those additional mesons can be explained with exotic particles which are described further in the next section.

1.3 Exotic Particles

Examples for exotic particles are compositions of quarks and anti-quarks as well as gluonic degrees of freedom: $q\bar{q}g$, $q\bar{q}gg$. These states are called hybrids. Also possible are so called multi-quark states like pentaquarks which consist of four or more valence quarks and antiquarks.

In the previous chapter the rules to figure out the quantum numbers for each particle have been discussed. Some particles happen to have quantum numbers which can not be constructed under these selection rules. Those states are called spin-exotics and they do not fit into the meson or baryon classification scheme. Some examples for exotic quantum numbers are

$$J^{PC} = 0^{--}, \, 0^{+-}, \, 1^{-+}, \, 2^{+-}, \, 3^{+-}, \, ...$$

Exotic quantum numbers are allowed due to more degrees of freedom (e.g. gluonic) than for a normal meson. One of the biggest challenges in their identification is, that exotic particles do not have to have exotic quantum numbers. This makes it rather difficult to separate meson states from exotic particles because the same quantum numbers allow for mixing of these states.

The third group of exotic particles are glueballs. Glueballs are particles which consist of two or three bound gluons, they are particles purely constructed from valence gluons. Gluons are the intermediary particles of the strong force. These types of particles are possible because they are a direct consequence from quantum chromo dynamics which allows for a self-coupling of gluons. They have no charge and no mass and they carry a color and an anticolor. They follow the same SU(3) symmetry as quarks, and therefore form a singlet and an octet. The singlet is a total symmetric wave function and is not able to change the color of a quark and it is purely colorless which enables the gluon to exist outside the confinement, but it has never been observed in nature.

A glueball of two gluons can have a spin of 0, 1, or 2 whereas it can only be 0 or 2 if the angular momentum is even and 1 if the angular momentum is odd. For a two gluon system this results in the following quantum numbers, cf. table 1.1.

Table 1.1: List of possible quantum numbers for glueballs.

L	S	J^{PC}
0	0,2	$0^{++}, 2^{++}$
1	1	$0^{-+}, 1^{-+}, 2^{-+}$
2	0,2	$0^{++}, 2^{++}, 4^{++}$
3	1	$2^{-+}, 3^{-+}, 4^{-+}$

As one can see in the second line of table 1.1 glueballs are allowed to have the same quantum numbers as pseudoscalar mesons. This makes an experimental proof difficult, because it allows for a mixing of ordinary mesons with glueballs. Glueballs decay differently than mesons. As they do not consist of any quarks they can not violate the OZI rule.

The OZI rule is named after Susumu Okubo, George Zweig and Jugoro Iizuka and explains the imbalance of certain decay modes. It says that if a Feynman diagram of a strongly occurring process can be split by just cutting internal gluon lines, this process is heavily suppressed. This leads to the characteristic of a flavor blind decay. Flavor blind decaying particles decay with the same branching fraction regardless of the flavor of the final state under the presumption that the available phase space does not influence the decay. This means that glueballs can decay to $\pi\pi$ modes as well as to $K\overline{K}$ modes, under the condition that the decay is not forbidden by conservation laws. Every mode is another possibility to identify probable glueball candidates.

A different approach is to make a theoretical prediction to be able to limit the search field for experimental measurements. Several different models have been developed and allowed to calculate possible masses of glueballs to compare to the experimental data.

The first is the *Bag* model [1] which considers gluons confined to a bag the same way as the quarks are confined in a hadron. The *Fluxtube* model has been established later and considers the glueball as a self-contained or closed fluxtube [2]. The results of these
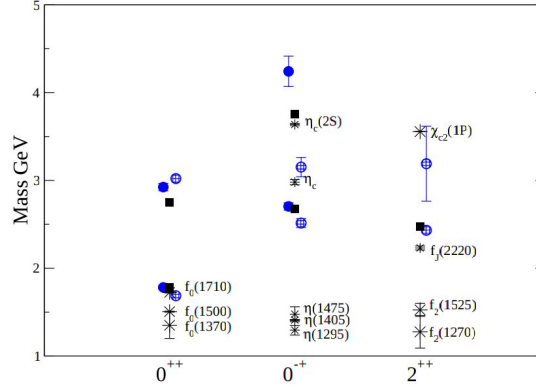
Figure 1.2: Glueball masses predicted by lattice QCD (blue), compared to the measured masses of established mesons (black). [3]

models are comparable to those of the lattice QCD calculations. Lattice QCD solves the QCD at discrete points in space and time positioned on a lattice. If the lattice becomes infinitely large and the points have an infinitesimal small distance from one another then continuum QCD is recovered. Nevertheless, LQCD is able to produce predictions for the masses of possible glueballs and one of those predictions can be seen in figure 1.2.

The blue markers are the predictions for the masses of glueballs of [3] and the black markers resemble the measured masses of known mesons. One resonance with isospin zero and spin zero is established for the scalar meson nonet: the $a_0(1450)$ which leaves two empty spaces. For these spaces three candidates are observed: $f_0(1370)$, $f_0(1500)$ and $f_0(1710)$. The $f_0(1370)$ is also well established, as the second highest mass state. The other two particles, from which only one fits into the nonet, are possible candidates for the scalar state with the biggest proportion of gluonic degrees of freedom. The first is the $f_0(1500)$ which has a much smaller decay width ($\Gamma = 109$ MeV [3]) as the other mesons of the nonet.

Furthermore glueballs can not couple electromagnetically, and therefore the decay into two photons in first order is suppressed strongly. On the other hand, the $f_0(1710)$ is much closer to the predicted mass of the lowest scalar glueball, but it couples to two photons, whereas the $f_0(1500)$ does not couple to two photons. Nevertheless the status of these resonances still remains ambiguous [4, 5, 6] . Similar conditions apply to the pseudoscalar meson nonet and the first angular excitations of its mesons, which are treated in the next section.

There are different experimental approaches for the identification of exotic particles. There is for example the circumstance that sometimes more mesons have been found than needed for the occupation of the nonet. This is helpful if the exotic particle has "normal" quantum numbers. Another way to clearly identify an exotic particle are its exotic quantum numbers. Furthermore exotic particles might show a different decay behavior as normal hadrons.

1.4 Experimental Status

For the pseudoscalar meson nonet of the first radial excitation more candidates have been found than expected. Three η-mesons have been observed in the mass region between 1.2 and 1.5 GeV/c^2. Two of them are considered to be the first radial excitation of the η and η', which leaves one resonance which does not fit into the classification scheme. The mesons are named $\eta(1295)$, $\eta(1405)$ and $\eta(1475)$. The $\eta(1295)$ and $\eta(1405)$ decay to $\pi^+\pi^-\eta$ each, while the latter one has been never seen before in photoproduction. Therefore, it is of particular interest to search for these resonances via photoproduction, as some ambiguities about theses resonances remain.

In this section the experimental situation of the higher η mass states as well as the status of the vector meson $f_1(1285)$ are discussed, because the $f_1(1285)$ is closely connected, from the experimental point of view, to the current discussion. At first an overview of experimental measurements is given and in the next step an overview over the current interpretation.

f$_1$(1285)

The $f_1(1285)$ was first observed in the middle of the 1960's at Brookhaven National Laboratory [7] as well as at CERN [8]. In both experiments the collision of two protons was used, and both detected an enhancement in $K\overline{K}\pi$ which was found to have the quantum numbers $J^{PC} = 1^{++}$.

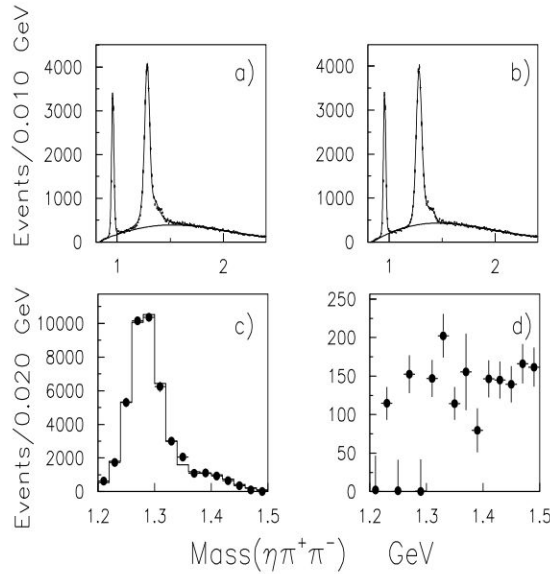**Figure 1.3:** Results of the spin parity analysis from the WA102 collaboration. a) shows the fits of a background function with three Breit Wigner functions for the η', $f_1(1285)$ and $f_1(1420)$, whereas b) illustrates the same, but under the condition of interference between the two f_1 resonances. c) and d) are the results for the hypothesis of a 1^{++} wave or a 0^{-+} wave. [9]
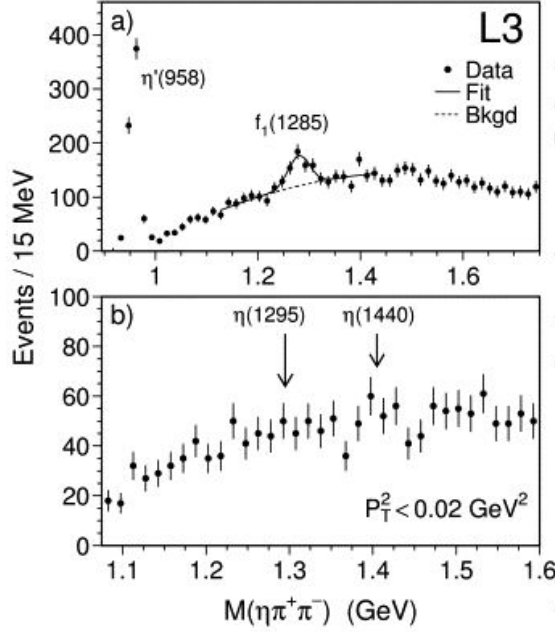
Figure 1.4: LE3 $\pi^+\pi^-\eta$ mass spectra: (a) total spectrum, the fit of a Gaussian plus polynomial background for the $f_1(1285)$ region is superimposed on the data; (b) for $P_T^2 < 0.02\,GeV^2$, arrows show the location of $\eta(1295)$ and $\eta(1440)$. [10]

The WA102 experiment at CERN was aimed to find non-$q\bar{q}$ states in central production in pp. On this data an analysis of the $f_1(1285)$ was performed in decays to $\pi\pi\eta$, $\pi\pi\pi\pi$, $\rho_0\gamma$ and $K\overline{K}\pi$. The $f_1(1285)$ is known to couple more strongly to the $\rho_0\gamma$ state than the $\eta(1295)$. The collaboration extracted a branching fraction $f_1(1285) \to \rho_0\gamma$ that is about 10 times smaller compared to $f_1(1285) \to \pi\pi\eta$, $\frac{\Gamma_{\rho_0\gamma}}{\Gamma_{\pi\pi\eta}} = 0.10 \pm 0.01 \pm 0.02$ [9], which aids the observation of $f_1(1285)$. In addition to this a spin-parity analysis was conducted of the $\pi\pi\eta$ final state. The results of this are presented in figure 1.3.

The authors of this publication have drawn the conclusion that central pp production is a clean production process for the $f_1(1285)$ and that they did not need a contribution of a 0^{-+} wave to describe the data. Central production is also under discussion as a good environment to produce glueballs, because two mesons are scattered diffractively and no valence quarks are exchanged.

The L3 experiment at LEP/CERN measured the $f_1(1285)$ in $\gamma\gamma$ fusion in $e^+e^- \to e^+e^-\gamma\gamma \to e^+e^- K_S K^{\pm}\pi^{\mp}$ and $e^+e^- \to e^+e^-\gamma\gamma \to e^+e^-\eta\pi^+\pi^-$. If the photons are real, meaning a $Q^2 \simeq 0$ where Q^2 represents the virtuality of the photons, the production of a spin 1 particle is strongly suppressed. If the photon becomes more and more virtual at high Q^2, the production of spin 1 mesons is favored in comparison to the spin 0 mesons. In figure 1.4 the invariant $\pi^+\pi^-\eta$ mass is presented. The upper plot presents a fit to the data using a Gaussian signal and a polynomial function for the background to the data. The fit yields a mean of $1280 \pm 4\,\text{MeV}/c^2$ and a width of $21 \pm 4\,\text{MeV}$, consistent with the values of $f_1(1285)$. In order to demonstrate that there is no contribution from a 0^{-+} wave, the mass spectrum is shown for a $\pi\pi\eta$ transverse momentum of $P_T^2 < 0.02\text{GeV}^2$,

whereas the P_T^2 equals Q^2 in good approximation. No contributions from $\eta(1295)$ and $\eta(1440)$ have been observed. An upper limit for the production of the two resonances with a confidence level of 95% for the $\pi^+\pi^-\eta$ decay was set [10].

$$\Gamma_{\gamma\gamma}(\eta(1440)) \times BR(\eta(1440) \to \eta\pi\pi) < 95\,\text{eV}$$
$$\Gamma_{\gamma\gamma}(\eta(1295)) \times BR(\eta(1295) \to \eta\pi\pi) < 66\,\text{eV}$$

$\eta(1295)$

The first hint for a new pseudoscalar resonance in the mass region of $1290\,\text{MeV/c}^2$ was found in 1979 at the Argonne National Laboratory. A $IJ^P = 00^-$ resonance with a mass of $1275\,\text{MeV/c}^2$ and with a width of $70\,\text{MeV}$ decaying into $\pi^+\pi^-\eta$ was seen in $\pi^-p \to n\pi^+\pi^-\eta$ with a production cross section three times higher than that of the $f_1(1285)$. A partial wave analysis was conducted and the mass spectrum could be well described by a Breit-Wigner shaped 0^{-+} resonance on top of a nearly flat background, as illustrated in figure 1.5a [11].

Secondly the E852 collaboration found further evidence for the $\eta(1295)$ [12]. The E852 experiment was located at the Brookhaven National Laboratory and studied pion proton scattering. The results of the analysis showed a low contribution from the $f_1(1285)$ decaying into $\pi^+\pi^-\eta$, but they found a large contribution from a 0^{-+} wave. The partial wave analysis was conducted on data taken at an momentum of $18\,\text{GeV/c}$ in the channel $\pi^-p \to n\pi^+\pi^-\eta$ as well. They observed two scalar resonances, the $\eta(1295)$ and the $\eta(1440)$ (discussed later in section 1.4). The $\eta(1295)$ was observed at a mass of $1282 \pm 5\,\text{MeV/c}^2$ with a width of $66 \pm 13\,\text{MeV}$. The extracted intensity of the $0^{-+}a_0\pi$ wave is shown in figure 1.5b. Their partial wave analysis also revealed that a weak contribution of a $1^{++}a_0\pi$ is needed to describe the enhancement in the $a_0\pi$ spectrum. Both resonances, the $\eta(1295)$ and $f_1(1285)$ were found to have nearly the same width which hints for

(a) Addition of intensity curves obtained by PWA in comparison to the mass spectrum in 5 MeV bins.[11]

(b) a) $0^{-+}a_0\pi$ intensity, b) $0^{-+}\sigma\eta$ intensity and c) total 0^{-+} intensity. [12]

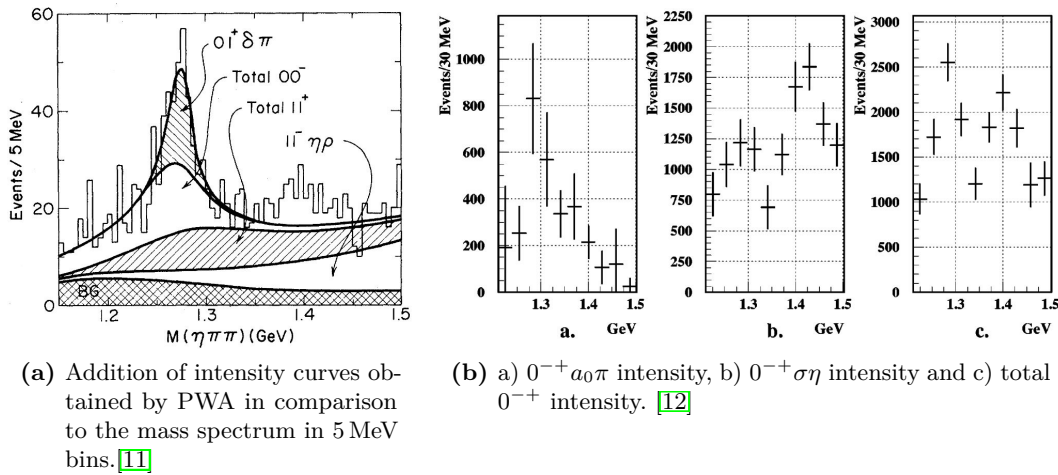**Figure 1.5:** E852 partial wave results for $\pi N \to N\pi\pi\eta$.

an ambiguity in the partial wave analysis (PWA). But an extended Monte Carlo study pointed out that the results were not an artifact of the PWA.

The Crystal Barrel collaboration used this wave in a partial wave analysis of $\overline{p}p \to \eta\pi^+\pi^-\pi^+\pi^-$ and achieved an improvement in the likelihood. But they optimized the fit with a mass of $1255 \pm 10\,\text{MeV/c}^2$ and a width of $90 \pm 23\,\text{MeV}$ and they did not observe an enhancement in the $\eta\pi\pi$ spectrum, neither at $1255\,\text{MeV/c}^2$ nor at $1295\,\text{MeV/c}^2$. For this reason and because the likelihood did not improve significantly they regarded the fitted signal as an upper limit [13].

The DM2 experiment at Orsay-DCI studied e^+e^- annihilations and saw a pseudoscalar resonance in $J/\psi \to \gamma\pi^+\pi^-\eta$ at a mass of $1265\,\text{MeV/c}^2$ [14]. They limited the partial wave analysis to angular momenta lower or equal to one and kept the 0^{-+} wave because it was subject to smaller fluctuations, but emphasized that this choice was arbitrary. Later analyses based on higher statistics could not reproduce this observation.

$\eta(1405)$

In the first observation only one enhancement at a mass of $1425\,\text{MeV/c}^2$ was found in 1967 at CERN PS with the Saclay 81 cm bubble chamber. The resonance was seen in $\overline{p}p$ decaying to $K\overline{K}\pi$ with the intermediate states $a_0(980)\pi$ and $K^*(892)\overline{K}$ where both channels contributed in equal measure [15]. The resonance with the quantum numbers $I^G J^P = 0^+0^-$ was named E and considered as the first radial excitement of the η' or as a glueball.

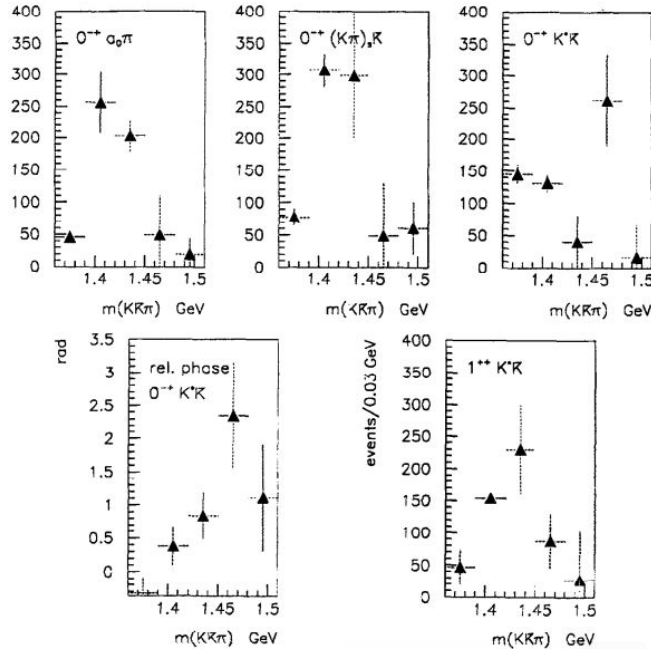In 1980 the resonance was seen by the Mark II collaboration at the Stanford Linear

Figure 1.6: Partial wave analysis results of the OBELIX collaboration: partial wave intensities and the $(0^{-+})K^*\overline{K}$ S-wave phase motion. [16]

Accelerator Center. In radiative decays $J/\psi \to K\overline{K}\pi$ a resonance was observed. Though the E was seen at the mass mentioned before they identified their enhancement at a mass of $1440^{+0.01}_{-0.015}$ MeV/c^2 preliminary as E [17]. Afterwards the particle was renamed to $\eta(1440)$. The successor experiment Mark III saw the same particle in the $\eta\pi\pi$ spectrum, but at a significantly lower mass of 1400 MeV/c^2 and named it ι. This controversy was named the E/ι puzzle. The region between 1400 MeV/c^2 and 1500 MeV/c^2 is named the E/ι region because two or three resonances have been seen in the $K\overline{K}\pi$, $\eta\pi\pi$ and $\rho_0\gamma$ final state.

It is now known that the E/ι is split into two states, namely the $\eta(1405)$ and the $\eta(1475)$, while the former tends to decay mainly through $a_0(980)\pi$ and the latter to $K\overline{K}\pi$.

The first indication for this split up was published by the DM2 collaboration in 1992. They identified two separate resonances utilizing a partial wave analysis. They also looked into radiative J/ψ decays and the same final states as mentioned above. They found the masses to be 1421 ± 14 MeV/c^2 and 1459 ± 5 MeV/c^2 for the $\eta(1405)$ and the $\eta(1475)$ and the widths to be 63 ± 18 MeV and 75 ± 9 MeV respectively. The quantum numbers are those of a pseudoscalar resonance for both states [14].

Another measurement was made by the OBELIX collaboration in $\overline{p}p \to K^{\pm}K^0_{miss}\pi^{\mp}\pi^+\pi^-$ at LEAR (CERN) [16]. They confirmed the existence of $\eta(1405)$ decaying mainly to $(K\pi)_s\overline{K}$ in the lower part of the E/ι region as well as $\eta(1475)$ decaying to $K^*\overline{K}$ and the $f_1(1420)$ decaying into the same final state. The intensities as a result of a PWA analysis are shown in figure 1.6.

1.5 Status of Excited η States

From the current point of knowledge, several scenarios to resolve the problem of too many resonances as candidates for the first radial excitation of the pseudoscalar meson nonet are discussed:

- The first scenario is, that the $\eta(1295)$ exists. If so then it would be the first radial excitation of the η. The characteristics of the $\eta(1405)$ would become dubious again. Due to its production in gluon rich environments and its decay to final states containing $\pi\pi\eta$ or $K\overline{K}\pi$, it might be dealt as a potential glueball or a particle with a large gluonic component. The remaining $\eta(1475)$ would then be the first radial excitation of the η'.

- The next explanation neglects the existence of the $\eta(1295)$, because it is degenerate in mass and width with the $f_1(1285)$. In this case the $\eta(1405)$ and $\eta(1475)$ are the first radial excitations of η and η' and the $\eta(1405)$ is not an exotic resonance.

- The last possible scenario is that the $\eta(1405)$ and $\eta(1475)$ are not two separate mesons, but the wave function of a meson called $\eta(1440)$ with two nodes leading to two apparently different states. Then the $\eta(1295)$ would be the excitation of the η and the $\eta(1440)$ would be the excitation of η'. If the $\eta(1295)$ does not exist an additional meson at a higher mass is missing as radial excitation for the η'.

As shown in the previous chapter there are a lot of ambiguities left for the first radial excitations of the mesons of the pseudoscalar ground states nonet. The η and η' are unmistakably identified. In contrast to this, the $\eta(1295)$ is questionable.

In the same mass region the axial vector meson $f_1(1285)$ is observed too. In addition to this the $f_1(1285)$ decays into the same final states as the $\eta(1295)$. The disentanglement of the $f_1(1285)$ and the $\eta(1295)$ can only be achieved with sophisticated methods like a partial wave analysis and a high statistic data set. Besides the difficulties of differentiating the two particles by mass is that the decay amplitudes of the decay of a pseudoscalar meson in three pseudoscalar mesons does not feature any specific characteristics. This means that the matrix elements are isotropic and flat. Therefore, it is possible to fake a 0^{-+} wave contribution if wrong assumptions for acceptance and resolution were made, statistics were too low or wrong assumptions in the partial wave analysis were made.

The $\eta(1405)$ has been seen in gluon-rich production processes only, like $\bar{p}p$ annihilation and radiative J/ψ decays.

All three particles decay to $\pi^+\pi^-\eta$ with a sufficiently large branching fraction, to be measurable in the decay channel $\pi^+\pi^-\eta$ if produced. The photoproduction offers an elimination criterion for some of the scenarios mentioned above as it provides a production process without a large gluonic component. Therefore, particles with a gluonic degree of freedom should be suppressed in first order production, as the photon only couples electromagnetically. If the $\eta(1405)$ is a glueball it should not be seen in photoproduction. Both the $\eta(1295)$ and the $f_1(1285)$ can be produced by this production mechanism, therefore this analysis yields a further measuring point to clarify the status of the $\eta(1295)$. To discuss further what production processes are possible in photoproduction a short introduction on these will be given

In particle physics, the Mandelstam variables are used to describe scattering processes with two incoming and two outgoing particles. The four-momenta of the incoming particles are labeled with p_1, p_2 and the outgoing ones with p_3, p_4. Then the Mandelstam variables s,t and u are defined as s is also known as the squared center of mass energy and

$$s = (p_1 + p_2)^2 = (p_3 + p_4)^2$$

$$t = (p_1 - p_3)^2 = (p_2 - p_4)^2$$

$$u = (p_1 - p_4)^2 = (p_2 - p_3)^2.$$
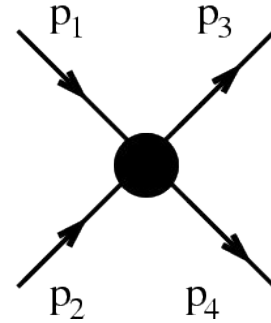
t as the four-momentum transfer. The sum of the four-momenta of the four participating particles squared is equal to the sum of the three Mandelstam variables. To describe the interaction between the incoming and outgoing particles, three Feynman graphs are needed.

During the s-channel process an intermediate resonance can be produced. In the case of photoproduction the incoming photon and proton can couple to a baryon resonance, for example a N^*, which is showed in figure 1.7a.
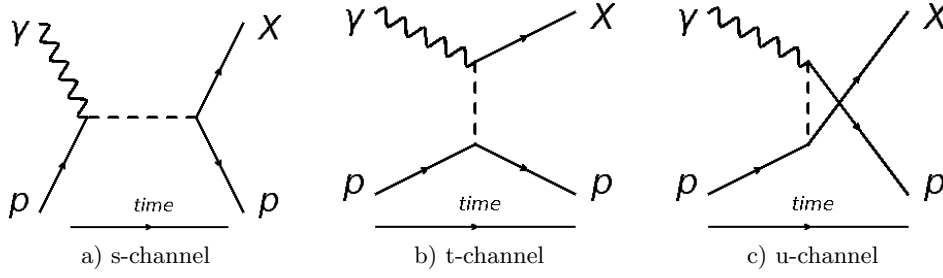
Figure 1.7: Production processes.

The *t*-channel process is also called meson-exchange process. In this case the incoming photon exchanges a virtual meson with the target proton. The process described by this diagram does not produce a peak in the cross section by itself, that can be experimentally observed. Imagine another diagram attached to this, where particle three and four form again the virtual exchange particle. This can be done again and again and is called "ladder" contributions. The sum of all these contributions can produce a peak in the cross section.

For the *u*-channel process the proton and the resonance are simply interchanged, in comparison to the *t*-channel process. The virtual particle in this process can be a baryon or a baryon resonance.

1.6 Motivation

So far no one has ever searched for excited η states in photon induced reactions. The CLAS experiment provides a high statistic, photoproduction data set and the possibility to examine the $p\pi^+\pi^-\eta$ final state for the $\eta(1295)$, $f_1(1285)$ and $\eta(1405)$, with the highest beam energy in photoproduction up to date.

The measurement of the $\eta(1295)/f_1(1285)$ and the $\eta(1405)$ in a photoproduction channel yields several advantages.

The $\eta(1405)$ has never been seen in $\gamma\gamma$ fusion or photoproduction. In contrast to this it has been seen in J/ψ decays which are classified as a gluon rich environment. Secondly the $\eta(1405)$ decays to final states containing pions as well as kaons. Both facts support the hypothesis of the $\eta(1405)$ having a significant gluonic content.

If one takes the possibility of the $\eta(1405)$ being a glueball into account, the photoproduction grants a perfect elimination criterion. Under the assumption the $\eta(1405)$ has a large gluonic component its production should be suppressed in photoproduction.

The t-channel process is hereby responsible for a gluon-poor environment and delivers a good exclusion criterion if the outgoing resonance is produced via this process. The process responsible for the production can be identified via the differential cross section in bins of the production angle of the produced resonance. The s-channel process is believed to produce a symmetric distribution, while the u- and t-channel process should produce peaks in the backward and forward direction, respectively.

Secondly the $f_1(1285)$ as well as the $\eta(1295)$ decay both to $\pi^+\pi^-\eta$ in the final state. Therefore, by analyzing this data set another measuring point is provided which of the

both particles is produced in photoproduction. For this identification it is possible to extract the mass and width of the resonance as well as the decay angular distribution. The decay angular distribution is interesting because the final state particles are all pseudoscalar mesons. If a pseudoscalar meson decays only to pseudoscalar mesons the decay angular distribution features different structures in contrast to an axial vector meson decaying into the same final state.

2 Experimental Setup

The analysis of this work was performed on data produced with an electron beam from the Continuous Electron Beam Accelerator Facility (CEBAF) converted to a photon beam and recorded by the CEBAF Large Acceptance Spectrometer (CLAS), located at the Thomas Jefferson National Accelerator Facility (JLab). At JLab three experimental halls (A, B, and C) are provided with a continuous-wave electron beam of up to 6 GeV in energy and $200\,\mu A$ in current from the CEBAF accelerator. The CLAS experiment is housed in Hall B and is perfectly suited to detect final states of multiple charged particles across a broad range of angles. Therefore, the 5.71 GeV electron beam is converted into a Bremsstrahlung photon beam by the Hall B photon tagger which incidents on a 40 cm long liquid hydrogen target. This analysis is based on a data set taken by the *g12* run group in 2009. The experimental proposals made for this runtime include meson spectroscopy, baryon spectroscopy and in-medium modification measurements.

2.1 CEBAF Accelerator

CEBAF is laid out as a multilevel recirculating linear accelerator (LINAC), shaped like an oval racetrack with a length of 1.4 km length in total. CEBAF was designed to deliver a high quality, continuous wave polarized electron beam of up to 6 GeV with currents of up to $200\,\mu A$ to the three experimental halls simultaneously. An aerial photograph of the accelerator site is shown in Figure 2.1a.

The location of the injector, linear accelerators and the experimental halls are illustrated as a schematic drawing (figure 2.1b). The accelerator was build in a new cost-saving design. In comparison to former accelerators, CEBAF uses superconducting radio-frequency cavities (SRF) to provide the acceleration gradient. Before that, only copper cavities have been used, which are expensive to operate due to resistive heating.

The electron beam is produced in the injector by a laser incident on a GaAs photo-cathode sample and is accelerated the first time to 67 MeV by the injector LINAC. The incidents are timed to pulses every 2 ns. These bunches pass an optical chopper to improve the separation of the bunches before they are accelerated further. Each bunch is $90\,\mu$m in length and separated 667 ps in time from the next bunch.

To gain an energy of ~ 6 GeV the electrons are accelerated by two LINACs on each side of the racetrack. One LINAC consists of 168 superconducting radio-frequency (SRF) Niobium cavities, a photo is presented in Figure 2.2a.

The injector supplies electrons in phase with the radio-frequency oscillating voltage. Standing radio-frequency waves form inside the cavity and the electrons feel always a force accelerating them in forward direction (cf. figure 2.2b).

This results in a positive electric force which accelerates each bunch simultaneously. Each LINAC is capable of providing 600 MeV of acceleration. Both LINACs are connected
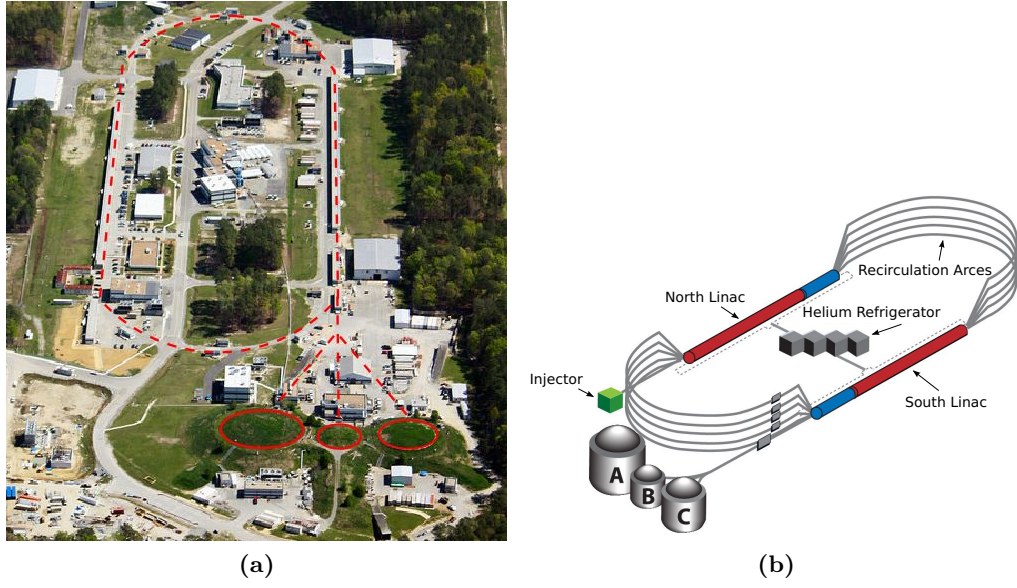
Figure 2.1: (a) Aerial view of the JLab accelerator site. The line in red indicates where the accelerator and the the three experimental halls are located.
(b) CEBAF [18].

by nine recirculating arcs, four on one side and five on the other, which results in five laps through the accelerator resulting in approximately 6 GeV beam energy, prior to extraction to the experimental halls. In each hall the beam energy can be controlled by choosing the number of laps completed before extraction, but every hall can get the highest energy, but not two the lower one. The beam switch-yard is capable of delivering bunches in turn to each experimental hall every 2.004 ns.
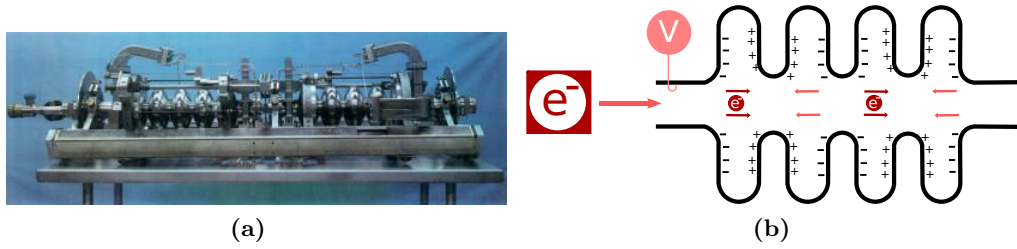

Figure 2.2: (a) A pair of CEBAF cavities [18]. (b) Schematic drawing of RF cavity.

2.2 Hall B Photon Tagger

The Hall B tagging system converts the CEBAF electron beam into a photon beam, a schematic diagram is shown in Figure 2.3. The incoming electrons pass through a gold-foil radiator. This radiator has a thickness of about 10^{-4} radiation lengths. While passing through the radiator, electrons can produce Bremsstrahlung, when they interact with the Coulomb field of the gold atoms. Thus the energy of the resulting photon is

corresponding to the deceleration of the electrons. A small, but negligible, amount of the electron energy is transferred to the nucleus of the gold atom. One can derive the energy of the photon by measuring the energy of the scattered electrons:

$$E_\gamma = E_e^{\text{CEBAF}} - E_e^{\text{scattered}},$$

where E_γ is the energy of the Bremsstrahlung photon, E_e^{CEBAF} the energy of the electron coming from CEBAF and $E_e^{\text{scattered}}$ the energy of the recoil electron. After passing through the radiator, the former electron beam is a mixture of non-scattered electrons, recoil electrons and photons. The photons proceed to the CLAS target, while the electrons are bend by a 1.75 T dipole magnet. The non-scattered, bended electrons proceed to the beam dump, while the recoil electrons get bend towards the two hodoscope planes, each made of overlapping arrays of scintillators.
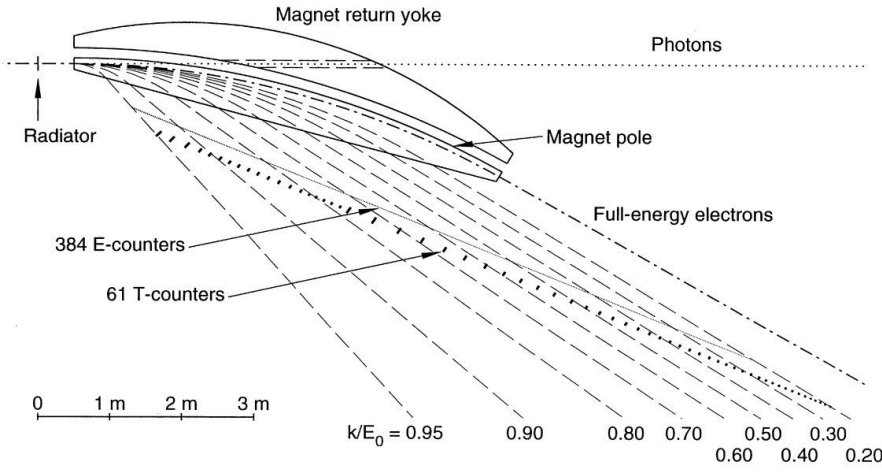

Figure 2.3: Schematic diagram of the Hall B photon tagger in profile. The scintillator arrays are marked with E- and T-counters, where the E-counters measure energy and T-counters provide timing information. The dotted line depicts the trajectories of the photons and the dashed line the trajectories of the electrons. [19]

The first layer of scintillators is used to determine the energy of the recoil electrons and are thus called E-counters. It consists of 384 paddles which are 20 cm in length, 4 mm thick and range from 6 to 18 mm in width. The overlapping design provides an increase in the number of logical paddles to 767. The trajectory of an electron inside a magnetic field is governed by its momentum. Consequentially we can measure the momentum of the electron by knowing which paddle it has passed. If the momentum of the electron is known, the energy of the emitted bremsstrahlung photon can be calculated. The energy resolution of the E-plane is 0.1% of the incident electron beam energy.

Below the E-plane is a second scintillator plane of 61 paddles for timing information, called the T-plane. These scintillators are 2 cm thick to provide a time resolution of 110 ps. A good timing resolution is crucial to allow for the deduction of the photon which caused the interaction at the CLAS target. It is also possible to identify the RF beam bucket, in conjunction with timing information from tracks in CLAS, each photon is associated with. The RF signal of the accelerator delivers the most accurate time measurement of

the experiment and allows to calculate the event vertex time by propagating the RF time from the radiator to the point in time where all final state particles were produced. The event vertex time is the time at which all final state particles that were produced are at the same point in space. Further information concerning the Hall B tagging system can be found in [19].

The beam is further refined using collimators to trim the beam halos. A sweeping magnet is installed to ensure that there are no charged particles left, which may have been created by a contact between beam and collimators.

One other essential part of the tagging system is the Total Absorption Shower Counter (TASC), located downstream of the target. The TASC is used to monitor the flux of the photon beam, but it needs a much lower beam current and a thinner radiator to avoid overload.

2.3 Experimental Target

During the *g12* run a target cell of the *g11* run group has been used. This cell is a tapered cylinder with a length of $40\,cm$ and $4-5.1\,cm$ in diameter, where the smaller radius is in downstream direction. The wall of the target is made of Kapton with a total thickness of $5\,\mu m$ and the beam windows on the ends of the cell are made of aluminum. In Figure 2.4 a computer graphic of the target cell can be seen.

For the *g12* run the target was placed $90\,cm$ upstream of the geometrical center of CLAS to reduce the angle subtended by the forward hole in CLAS and filled with unpolarized liquid hydrogen.

The density of the target is crucial for extracting a differential cross section. Therefore, the temperature and pressure of the target cell are monitored.

Figure 2.4: Target cell used for the *g12* run [20].

2.4 CLAS Detector

The CEBAF Large Acceptance Spectrometer (CLAS) detector is housed in Hall B at Jefferson Lab. The CLAS detector is suitable for multiple particle detection. Its shape is roughly spherical and divided azimuthally along the beamline into six individual parts

which can be operated as independent detector packages, as shown in Figure 2.5. The detector consists of the following subdetector components:

- **Start Counter**: The start counter surrounds the target cell and provides timing information and is described in Section 2.4.1.

- **Magnet**: The magnet is made of six lobes and produces a toroidal field and is described further in Section 2.4.2.

- **Drift Chambers**: The drift chambers are for charged particle tracking and momentum measurement, cf. Section 2.4.3.

- **TOF**: The time-of-flight system delivers timing information for the events and is explained in Section 2.4.4.

- **Čerenkov Counter**: The Čerenkov counter enables distinction between pions and leptons. Further information can be found in Section 2.4.5.

- **EMC**: The electromagnetic calorimeter (EMC) measures the energy of photons, leptons and neutrons, see Section 2.4.6.

These subdetectors sum up to $\sim 40,000$ readout channels for each trigger and their signals have to be recorded by the Data Acquisition System (DAQ) (Section 2.5). The offline reconstruction converts the digitized signals of all detectors into four-vectors and PID information by means of a specialized software and batch computing. Based on the results of the offline reconstruction the event selection and data analysis can be performed.
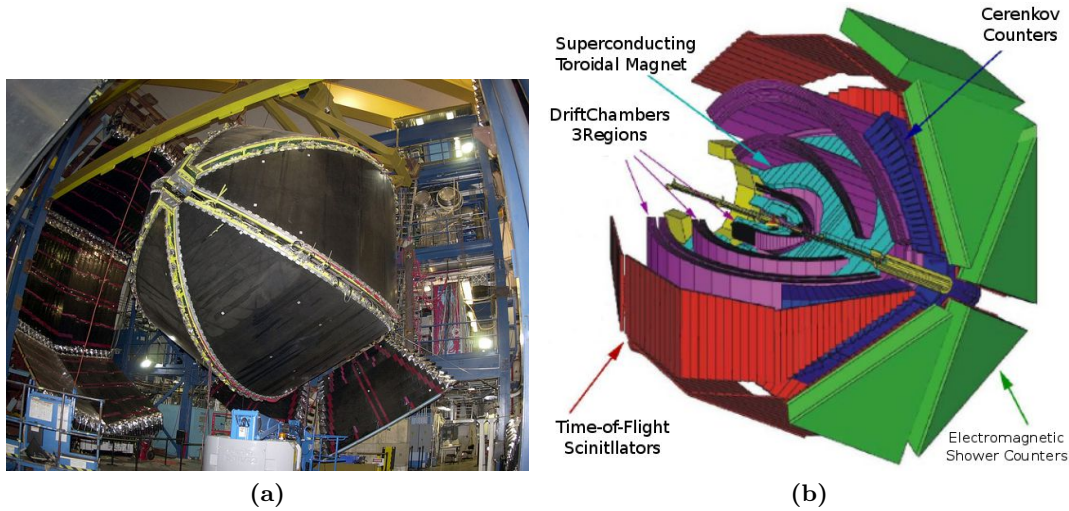

Figure 2.5: (a) A photo of the CLAS detector without the TOF. (b) A schematic drawing showing all subdetectors of CLAS ([18]).

2.4.1 Start Counter

Photons can interact with protons in the target and produce new particles. The first detector which these particles pass after leaving the target is the Start Counter (ST), which can be seen in Figure 2.6. The ST resembles the hexagonal symmetry of the CLAS detector. Each of the six parts is made up of four scintillator panels with a thickness of 2.2 mm, which leads to a total of 24 readout channels. Towards the downstream end of the start counter the scintillators are bent to the beamline and narrowed in width to cover the front end of the target. The light output of the scintillators is collected with phototubes which are attached to the upstream ends of the scintillators. The ST can achieve a time resolution of 350 ps.

The output of the phototubes is further processed by a Time-to-Digital Converter (TDC) and an Analog-to-Digital Converter (ADC), but only the time information is used in the offline reconstruction. The time information of the events from the ST can be used to associate hits in the photon tagger properly with tracks in CLAS to deduce the responsible beam photon.

Most of the tracks which caused a signal in the ST will later cause a hit in the Time-Of-Flight (TOF) as well. By combining the path length from ST to TOF and the time difference between the two hits one can derive the velocity of the particle. Knowledge of the particle velocity enables the propagation back to the event vertex inside the target and the determination of the time when the event took place. This is crucial for high multiplicity events, i.e., events with more than two tracks, to determine the correct beam photon for each event. The list of hits in the tagger for the event can be compared with an average of the times from the tracks' start times and used to select the photon which arrives at the event vertex at the same time as the tracks' averaged event start time.

It is possible to combine the logic of the timing counters of the tagger with the ST to record only events with a certain photon energy.
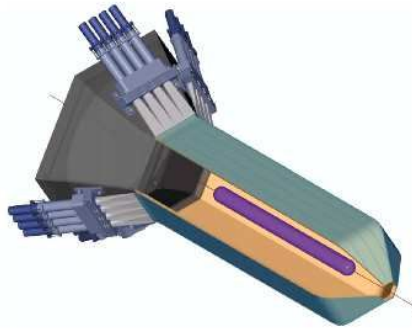

Figure 2.6: Drawing of the CLAS start counter. [21]

2.4.2 Superconducting Toroidal Magnet

An integral part of the detector is the toroidal magnet. The magnetic field forces charged particles to move along non linear paths through the detector. The trajectory of each particle is thereby traced by the tracking system (Section 2.4.3). Given the trajectory

and the strength and direction of the magnetic field, the momentum of the particle can be determined.

The magnet is made up of six kidney-shaped nonferrous superconducting coils, which are mounted every 60° in azimuthal direction. Tracks of charged particles are only bent in polar angle and thus charged particles rarely enter two different sectors. In normal operation mode the magnetic field causes negatively charged particles to be bent toward the beam line and positively charged particles to be bent away from the beamline. This results in a higher detection efficiency for positively charged particles, because the particles which are bent inward have a higher chance to get lost in the beamline or the forward hole. This makes a simplification of the tracking algorithms possible and allows for optimization of the design of the drift chamber in the expense of acceptance.

The field of 2.5 T is reached at its normal operating current of 3861 A. Two field maps of the magnet are shown in Figure 2.7a and Figure 2.7b. Figure 2.7a illustrates the strength of the magnetic field between two of the coils. The strength varies downstream as well as radially, the highest magnetic field strength is in forward direction behind the target and near the beamline and is lower in the downstream region and farther away from the detector in radial direction. In Figure 2.7b the field centered at the target in the x-y-plane is presented, the length of the lines are proportional to the field strength.
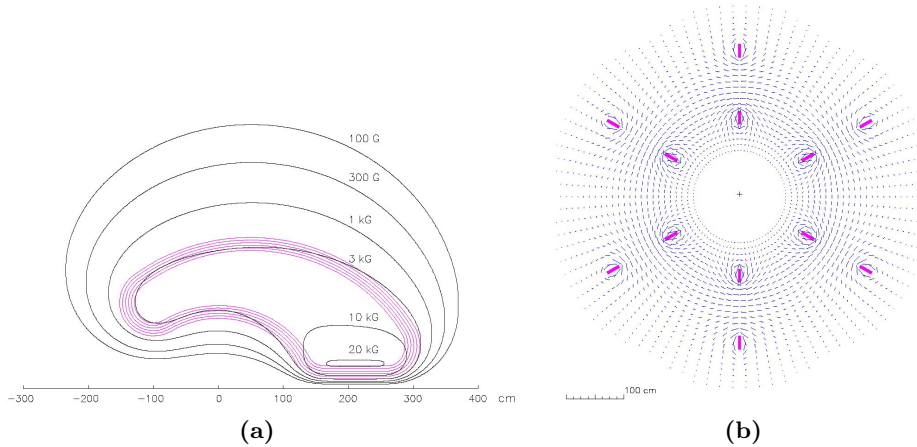

Figure 2.7: (a) Contour plot of the constant magnetic field for the main CLAS toroid between two coils.
(b) Magnetic field vectors for the CLAS toroid looking upstream in a plane centered at the target position.[22]

2.4.3 Drift Chambers

Each single sector of CLAS contains three sets of Drift Chambers (DC) which are located in three different regions R1, R2 and R3. A schematic drawing is shown in Figure 2.8. The R1 drift chamber, the smallest one, is located near the target and beneath the lobes of the torus and is, therefore, nearly field-free. The R1 drift chamber set is used to determine the initial direction of charged tracks. For a high resolution for the momentum measurement the R2 set of drift chambers is interleaved with the torus coils to measure at the point

of the strongest magnetic field strength to gain the highest possible track curvature of bent charged particles. The drift chamber set R3 is positioned at the largest radius of the three sets and is the biggest one. In this region the magnetic field is low so that the final direction of the charged track is measured.

Each region consists of six drift chambers corresponding to the six segments of CLAS. Each chamber contains one superlayer of axial orientated wires (relative to the magnetic field direction) and one stereo superlayer with sense wires in six layers at an angle of 6° with respect to the axial wires. The axial superlayer consists of six layers of sense wires (only four in the case of R1) and the stereo superlayer consists of six layers of sense wires as well. The wires of a superlayer are arranged in a hexagonal pattern with up to 192 wires per layer. Each layer is strung with $140\,\mu$m gold-plated aluminum alloy field wires interspersed with $20\,\mu$m gold-plated tungsten sense wires to form a layer with the sense wires in the middle, giving the chambers a good position measurement at a wide variety of tracks.

The field wires are operated with a high negative voltage, where the sense wires are kept on a positive potential. The chosen drift gas mixture contains 90% Argon and 10% CO_2, due to its ionization properties and additional non-flammable. The read out signals from the sense wires are processed by preamplifiers and amplifier discriminator boards and finally to the TDC to obtain the time information.

The single wire resolution is $330\,\mu$m and the momentum resolution is $\delta p/p \leq 0.5\%$ for $1\,$GeV/c. The resolution decreases with increasing polar angle, because of the magnetic field strength. More information concerning the CLAS drift chamber can be found in [23].
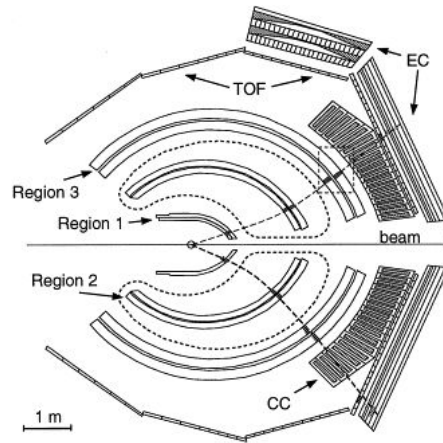

Figure 2.8: CLAS in x-z-plane showing the relative positions of the subdetectors. Three sets of drift chambers can be seen, the first one near the target (R1), the second one between the magnet coils (R2, dashed lines), and the third one outside the magnets (R3). [23]
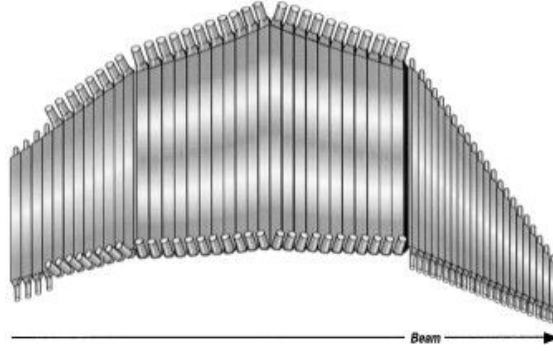
Figure 2.9: A single sector of the CLAS TOF. [24]

2.4.4 Time-of-Flight

The TOF system is used to measure the arrival time of charged tracks after they passed the detector. The TOF system is mounted 4 m from the cryotarget downstream. By dividing the path length of the particle by the time it needed to travel from the start counter to the TOF, its velocity can be deduced. Knowing the momentum and its velocity allows to calculate its mass, and thereby determine its identity. This characteristic makes the time-of-flight system a part of the Level 1 trigger (Section 2.5).

The TOF consists of six sets, with 57 scintillator paddles each. One set can be seen in figure 2.9.

These 57 scintillators are divided in three groups, based on the range in polar angle under which they detect particles. The detectable forward angle ranges from $8.6°$ to $45.9°$ and is covered by the first 23 scintillators. Paddles 24 to 53 cover an angular range of $45.9°$ to $131.4°$ and the last four paddles cover the angular range between $134.2°$ and $141°$. The paddles of the first and last set are 15 cm in width and instrumented with 2 inch photomultipliers. The middle set of paddles is 22 cm in width and instrumented with 3 inch photomultipliers. These photomultipliers are mounted on both sides of 5.08 cm thick Bicron BC-408 scintillating plastic paddles.

The paddles which cover the most-forward angles are optimized with respect to the time resolution, where as the scintillators for the larger angles are simply optimized for expense reasons. Therefore, the timing resolution varies between 80 and 160 ps. The photomultiplier signal is passed through leading-edge discriminators and readout by both TDC and ADC. The ADC information can be rudimentary used to perform particle identification, but is primarily used for calibration purposes. A more detailed description of the TOF systems and its construction and performance is given in [24].

2.4.5 Čerenkov Counter

The Čerenkov counter (CC) is crucial for the distinction of pions and leptons. Leptons traveling through the active volume of the CC can emit Čerenkov light, whereas light hadrons like pions are not traveling faster than the speed of light in the detection gas. The CC is made up of six identical modules, fitting to the CLAS design, and mounted just outside the R3 drift chambers. Eighteen light-collection fixtures are mounted in
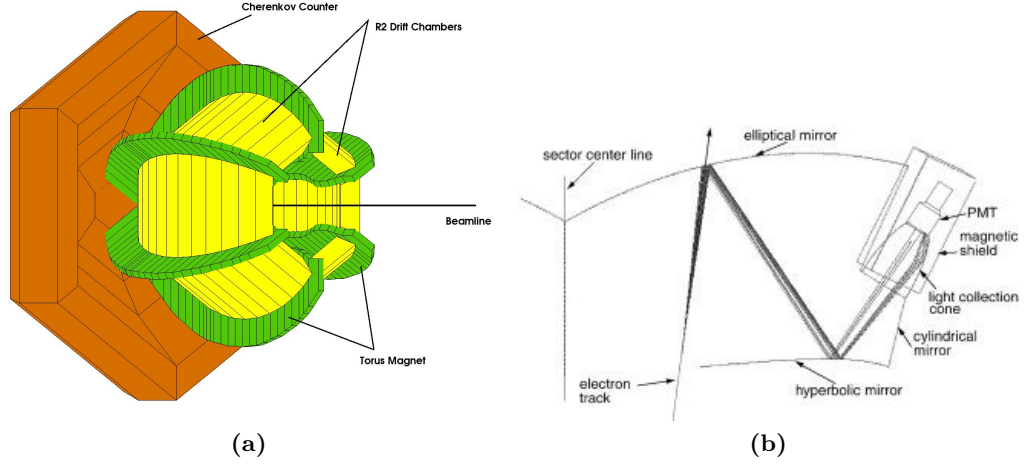
Figure 2.10: (a) The CLAS Čerenkov counter and the R2 drift chambers as well as the torus to give a sense of position and scale. (b) Schematic drawing of the inner construction of a single mirror pair. [26]

a single module. Each fixture covers a small range of the polar angle. One fixture is made of two pairs of mirrors opposed to one another along the axis of the CC module. The light emitted by the particles travels to the outer-surface mirrors which reflects and focuses the light back across the body of the module to the hyperbolic inner-surface mirrors which then reflect the light into photomultiplier tubes mounted along the edges of the CC module (figure 2.10). Perflourobutane (C_4F_{10}) is used as detection gas. The characteristics of perflourobutane allow a separation of leptons and pions only up to 2.5 GeV/c.

The CC is used to detect scattered beam electrons as well as for trigger setups because of its fast response time [25].

2.4.6 Electromagnetic Calorimeter

The outermost part of CLAS is the Electromagnetic Calorimeter (EMC). The EMC is used to detect neutral particles like photons or scattered leptons. The EMC is a sampling calorimeter with six panels in total. Each panel has the shape of a triangle and is a stack of 39 layers of plastic scintillators alternating with 2.2 mm lead sheets. Each scintillator (BC412) layer is segmented in 36 individual strips of 10 mm thickness. The direction of the strips of each layer is rotated by 120° with respect to the foregoing layer. These rotations create a u-v-w geometry and make position measurements possible. A schematic drawing of one panel is shown in figure 2.11.

The ratio of lead to plastic was chosen to be 0.2 so one third of the particle shower energy is deposited in the scintillator. Every sector is logically divided into two stacks, an inner one and an outer one. The inner stack includes eight logical layers while the outer one has only five. Per module 216 photomultipliers are needed to supply 36 strips per direction in each of the two stacks, which sums up to 1296 channels for the six panels. The characteristics are as follows:

- Energy resolution $\sigma/E \leq 0.13/\sqrt{E(\text{GeV})}$

- Position resolution $\delta r \approx 2\,\text{cm}$ at $1\,\text{GeV}$

- Response time for event trigger $\ll 100\,\text{ns}$ (energy sum)

- Time-of-Flight resolution $\approx 1\,\text{ns}$

- π/e rejection $\geq 99\%$ at $\text{E} \geq 1\,\text{GeV}$

One panel of the EMC is shown in figure 2.11 and additional information about the EMC can be found in [27].
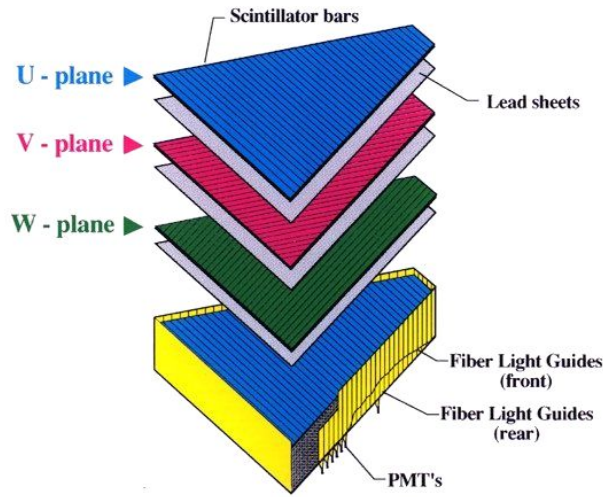

Figure 2.11: Exploded view of a module of the CLAS electromagnetic calorimeter. [27]

2.5 Trigger and Data Acquisition

Every detector is equipped with electronics to collect its signals. Signals are caused by physics events, but not exclusively. They can get invoked by a number of background sources like cosmic radiation passing through a detector element or electronic noise. The trigger has to decide which sets of signals form a physics event. These signals are collected and written to tape by the Data Acquisition System (DAQ). The signals come from the channels of each subdetector like the sense wires of the drift chambers, the photomultipliers of the ST, TOF, Cerenkov detector, and EMC and sum up to around 40,000 channels in total. The data is recorded in an *event-based* format, where the time is divided up into finite intervals and the signals present in each detector at the end of an interval are written to disk.

The discriminator monitors each channel. For each kind of signal a certain threshold is defined and only signals exceeding these thresholds are allowed to be processed further.

Signals which passed the discriminator are regarded to originate from physics interaction and are digitized by two types of hardware. The TDC simply reports the time at which a signal arrives. The ADC digitizes an analog signal or rather reports a number corresponding to the integral of the signal. Every TDC and ADC can handle a multitude of signals in parallel and write their output to a single data stream. Software processes running on server clusters communicate with each TDC and ADC and assemble their data stream into an event-based data format which is then stored on a disk array. The trigger opens up the possibility to store only certain events. The trigger definition itself is a list of signals from various detectors which have to be present for a certain event. As the DAQ monitors signals for finite intervals of time the trigger has to come to a decision instantaneously or at least as quick as possible. During the *g12* run every 100 ns a decision was made. All the subsystems, except the drift chambers, can acquire signals in a few nanoseconds. This allowed for the use of the Hall B tagger, ST, TOF, EMC, and CC to define trigger conditions.

The most complex trigger configuration was made possible by using a Field Programmable Gate Array (FPGA) as trigger supervisor. Each trigger condition can be changed during running and twelve independent trigger conditions were in place during running. The *production* trigger was the primary trigger and designed to record meson spectroscopy events. It required three charged tracks at any beam photon energy or two charged tracks with a high energy photon. These conditions can be met by implementing coincidences between the start counter, time of flight, and a logic unit providing an OR between the first 19 paddles of the tagger, called the master-OR (MORA). Various combinations of these trigger rules occupied usually 6 slots in the supervisors, the other 6 rules were dedicated triggers for other aspects of the *g12* experimental program.

The drift chamber can be used for a trigger decision, but only at the second level (L2 trigger). In this scenario events which passed L1 are routed on to L2 which is mostly a software routine and no pure hardware system. This software does perform an online, and therefore, fast, but coarse, track reconstruction to confirm if the L1 decision was caused by particles traveling through the detector.

During the *g12* run the rate of records of the DAQ was 8 kHz, compared to *g11* with 5 kHz. More information can be found in [26].

2.6 Event Reconstruction

After the data of the subdetectors have been written to disk, the events have to be reconstructed. The reconstruction of events is done by searching for certain patterns in the signals of the subdetectors. The first stage is called *hit-based-tracking*. The reconstruction of an event is independently conducted for each sector and starts with the drift chambers. Only the position of hit wires in a given sector is required. Adjacent hits in each superlayer are grouped into clusters and these clusters are linked in each region following the drift chamber geometry to produce track segments. A full hit-based track is reconstructed if the track segments are linked once more across the three regions. The charge and magnitude of the momentum of each track are given by the sign and magnitude of the curvature of the track as it passes through the R2 drift chamber.

It is possible that signals are produced by noise so that whole clusters can be found

which are not associated with physical tracks. Therefore, the hit-based tracks deliver a first approximation only. These noise hits can be identified by extrapolating the tracks to the suitable TOF panel and search for hits in panels where the track was supposed to hit. TOF panels are read out by a TDC, too. This enables one to set an upper limit to the times of the drift chamber hits correlated with the track. This is called *time-based-tracking*. All drift chamber hits correlated with the track are checked for the time when the hit happened starting in the inner part and going to the outer part where they are required to be in increasing time order as the track moves outwards. All hits and clusters which do not fit the requirements are removed and the track is refitted. This process is repeated two more times with more stringent requirements to refine the momentum measurements as well as the measurement of the event vertex, determined by the distance of closest approach of the track to the beamline.

A set of tracking parameters is assigned after the time-based tracking algorithm has filtered a set of hits which fits best to the signals. The track is then extrapolated to the rest of the detectors. The start counter, Čerenkov counter and EMC are examined for hits where the track intersected the detectors. If hits are found they are added to the description of the track. In the final reconstruction a well-known state is assigned to the track based on its mass and charge. The mass can be calculated using time and momentum information

$$
\begin{aligned}
m &= \frac{cp^2}{\beta^2}, \\
\beta &= \frac{t_{\text{TOF}} - t_{\text{vertex}}}{cl},
\end{aligned}
$$

where c is the speed of light, p is the track momentum, t are the start and end times of the track measured by the start counter or tagger and the TOF and l is the length of the track. The calculated masses are distributed in a certain range according to measurement inefficiencies. Therefore, a threshold for the calculated value of m is defined for particle identification:

$$
\text{Particle ID} =
\begin{cases}
\pi & \text{if } m < 0.3\,\text{GeV/c}^2 \\
K & \text{if } 0.35 < m < 0.65\,\text{GeV/c}^2 \\
p & \text{if } 0.8 < m < 1.2\,\text{GeV/c}^2 \\
d & \text{if } 1.75 < m < 2.2\,\text{GeV/c}^2
\end{cases}
$$

Sometimes the beam photon causing the event is not recorded by the tagger and another one is chosen instead, or a single TOF paddle reports two hits in sequence, but with different times. In those cases it can happen that the calculated masses are between the cuts and, therefore, classified as unknown.

2.7 g12 Data Set

For this analysis data are used which have been recorded from August to December in 2009, called the *g12* beam time.

An integrated luminosity of 68 pb^{-1} corresponding to 26 billion events were written to tape. Those events are chopped in run files with approximately 50 million events each.

Runs that were ended prematurely, because of poor beam quality or DAQ failure for example were discarded as well as broken run files or run files with less than 1M events. After the first refining process 622 "good" runs in total remain and occupy 121 terabytes of disk space.

Additionally to this a Monte Carlo simulation has been used for the determination of the detector efficiency as well as estimation of possible background channels.

2.8 Monte Carlo Event Generation

The accurate reconstruction of an event is affected by the efficiencies of the detectors. Physical detectors are never ideal and every detector has its own inaccuracies and resolutions which have to be taken into account. Events are generated in accordance to the desired channel and propagated through the simulation of the detector. The result is then processed further with all the cuts and analysis tools used for the data sample.

The `GSIM` package provides a full simulation of CLAS and contains all the inefficiencies and resolutions of the sub-detectors. Regions where the simulation does not reproduce the detector behavior in a reasonable way were cut out from our analysis as mentioned in section 3.4. After this procedure we are able to calculate a fraction of events lost as a function of their kinematics or acceptance. This enables us to correct the derived quantities like differential cross sections or measured yields from the reconstructed events accounting for detector efficiencies as well as the efficiency arising from our cuts.

2.8.1 Event Generation

For acceptance calculation events of the desired decay channels are needed. The decay chains generated are listed in table 2.1. For each listed mother particle each mentioned decay chain has been simulated.

Table 2.1: Simulated channels.

mother particles	decay chains
$\eta(1295)$, $f_1(1285)$, $\eta(1405)$, X	$\pi^+\pi^-\eta(2\gamma)$
	$\pi^+\pi^-\eta(3\pi^0)$
	$\pi^+\pi^-\eta(\pi^+\pi^-\pi^0)$
	$\pi^+\pi^-\eta(\pi^+\pi^-\gamma)$

The simulation includes a Bremsstrahlung distribution for the beam photon energy. For the $\eta(1295)$, $f_1(1285)$ and $\eta(1405)$ approximately 720 thousand events have been generated each. In table 2.1 the X refers to an arbitrary resonance with a mass of $3\,\mathrm{GeV/c^2}$ and a width of $10\,\mathrm{GeV/c^2}$ to sample the available phase space for $\pi^+\pi^-\eta$ uniformly and randomly. Approximately 60 million events have been generated for this purpose. All these generated events are called *raw-monte-carlo* and after they have been processed through algorithms, the detector simulation and the analysis procedure, they are called *accepted-monte-carlo*.

The generated events are passed to a software called `gamp2part`, because a PART bank containing the Monte Carlo event is needed. `gamp2part` is customizable to smear the target distribution in x, y and z. The detector simulation `GSIM` is `GEANT` based and simulates

the transition of the generated events, the simulated detector response and effects of the materials on the path where the particle might scatter or react otherwise. Unfortunately the simulation does not account for all effects and the timing and momentum resolution is better than for the real data. For this purpose the software package `GPP` is used which smears the timing and momentum resolution and removes dead TOF paddles and DC wires. The resulting gsim file is then processed with `a1c` for cooking, which results in a bos file like the real data. This a1c file is then treated like a data file and all analysis procedures are applied as well.

3 Event Selection

This analysis is a search for excited η resonances in photoproduction. The resonances of interest for this analysis, the η', $\eta(1295)$ and the $\eta(1405)$ decay all into $\pi^+\pi^-\eta$. The event selection is based on purifying a data sample to retain only $p\pi^+\pi^-\eta$ events. The η is not detectable, because of CLAS' inability to detect neutral particles. Incidental background in the data sample is caused by inefficiencies of the detector or reconstruction algorithms. Another form of background is physics background. This can be caused by reactions with a $\gamma p \rightarrow p\pi^+\pi^-\eta$ final state, but that are not originating from an intermediate excited excited η, but eg. via baryon resonances.

The event selection is a crucial part of most physics analyses and is a compromise between the removal of background events and the retaining of signal events. In an ideal world one would be able to find a set of rules to choose only the signal events without loss, while the background events are rejected. In reality one rejects some signal events along with most of the background events. Ideally each selection of events increases the ratio of signal to background events, but with every selection you lose events and, therefore, increase the statistical uncertainties as well. Depending on the background source contaminating the data sample systematic uncertainties can be introduced if the data sample is not clean enough.

In the first step of the analysis the beam photon which triggered the event will be chosen. Then the data samples gets refined further by rejecting events which did not have their origin inside the target, which do not fit the particle identification (PID) requirements or which momentum was too low to get reconstructed well. After all reasonable cuts have been applied a method is used which suppresses the remaining background.

3.1 Preliminary Data Skim

The data was initially skimmed according to the number of charged tracks per event. Exactly three tracks were required where two must have an assigned positive/negative charge. In the next step PID information was used to demand the positive particles to be a proton and a pion and the negative particle to be a pion. The final state is $p\pi^+\pi^-\eta$. The η can not be detected, as CLAS is only capable to detect charged particles well. Therefore, the η is reconstructed via the missing mass of the $p\pi^+\pi^-$.

3.2 Beam Photon Selection

Since *g12* is a high luminosity run it is necessary to identify the photon which induced the event, further called beam photon. The high beam current which intersects with the radiator can produce a multiplicity of photons which then causes multiple hits in the
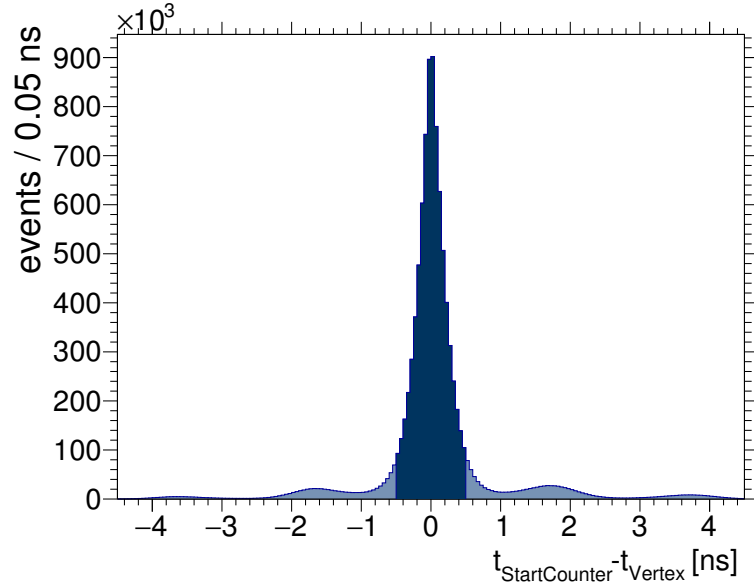
Figure 3.1: Difference between the vertex time and the start counter time.

tagger. To select the right photon the start counter is used as described in 2.4.1. The start counter reports the time and deposited energy of each hit.

The extrapolated tracks from the drift chamber can then be used to determine which paddle is related to the track and where the event vertex is located in the target volume. Including the information of the TOF the speed of the particle can be determined. Using the distance between the event vertex and the hit paddle of the ST as well as the speed information one can calculate the time the particle needed from the vertex to the ST paddle, which then can be subtracted from the time when the particle hits the start counter. This yields the time when the track was produced. Doing this for all tracks which are averaged then, one obtains estimates for the time for each event. This time is called the *start counter vertex time*.

The tagger has measured the remaining energy of the scattered beam electrons as well as the time of entrance. Knowing the distance between the radiator and the hit paddle as well as the distance between the radiator and the target, the time when the produced photon hit the target can be determined. Comparing the time of the photon, the event vertex time as well as the electron hit in the tagger with the best agreement enables one to selected the photon that triggered the event.

CEBAF delivers a bunch of electrons every $2.004\,\mathrm{ns}$ and a beam current of 60–$65\,\mathrm{nA}$ was chosen which results in a photon flux of $5 \cdot 10^{8} \gamma/\mathrm{s}$ or about 50 photons measured by the tagger for each event. In some cases it is possible that a photon produced by a beam bucket before or after the current one is actually responsible for the event. To account for this a cut is applied on the difference between the vertex time and the time measured by the start counter (figure 3.1).

The possibility of having two photons which fit in the time window is high. The timing
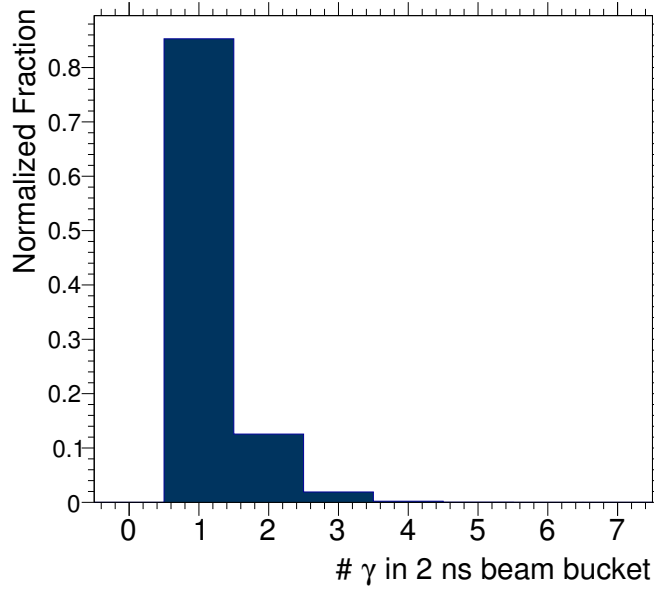
Figure 3.2: Fraction for single and multiple beam photons within the 2 ns timing window.

given by the accelerator is the most accurate available, and therefore, it is not possible to distinguish the event photon from the others by a timing perspective. The distribution of the number of photons per beam bucket is shown in figure 3.2.

It is visible that most of the events have only one photon candidate per beam bucket, but there is, still, a significant amount which has two or more photon candidates. The probabilities for certain numbers of beam photon candidates in-time are listed below:

- 85.1% of the events have one in time photon,

- 12.5% of the events have two in time photons,

- 1.7% of the events have three in time photons

- and less than 0.5% of the events have more than 3 in time photons.

For this analysis the photon with the highest energy from all candidates was chosen.

3.3 g12 Corrections

To obtain the right values for the components of each 4-vector several corrections have to be applied on the data which will be discussed in the following. The first is a final-state particle momentum correction due to energy losses of a particle that travels through matter. Also a correction for the sagging of the tagger which was handled by the tagger calibration and finally a correction for changes in the magnetic field strength of the tagger is applied.

3.3.1 Energy Loss Correction

The momentum measurement of a particle starts after the particle passed through the target and the start counter. Therefore the measured momentum is decreased by the energy lost in matter. This energy loss is due to atomic excitation and ionization caused by the charged particles while traveling through the matter. The energy loss is proportional to the distance the particle has passed in the target volume, while it is assumed that the angles are not affected by this. The energy loss of charged particles in matter is described by the Bethe-Bloch equation:

$$-\frac{dE}{dx} = \frac{4\pi}{m_e c^2} \frac{n z^2}{\beta^2} \left(\frac{e^2}{4\pi\epsilon_0} \right)^2 \left[ln \frac{2 m_e c^2 \beta^2}{I \cdot (1 - \beta^2)} - \beta^2 \right] \sim \frac{ln\gamma}{\beta^2}$$

Light particles like electrons or positrons which travel with velocities of $\beta \approx 1$ loose less energy than heavy particles like protons. The energy loss routine is therefore not applied to light particles. For those charged particles that are effected by an energy loss the corrections were made for the intersected materials: liquid hydrogen, Kapton walls of the target, beam pipe, the start counter and the air between the first set of drift chambers and the start counter. The corrections are included as an add-on in the `CLASEVENT` software package and were written by Eugene Pasyuk [28].

3.3.2 Beam Corrections

The correction for the incident beam photon energy is handled by the `a1c` software package. The correction is due to a gravitational sagging of the tagger's focal plane, which leads to wrong energy measurements of the scattered electrons.

Another issue showed up during the complete run time. Initially the measured missing mass was systematically too low , during the investigation the missing mass changed depending on the run varying by as much as 10 MeV. The issue was analyzed and corrected using two decay different channels.

The reason of the changing missing mass was found to be caused by a changed magnetic field strength of the tagger magnet. A shutdown of the tagger magnet took place and after the restart the field strength changed although the tagger current was the same. A known phenomena in magnetism is the hysteresis of the magnetic fields which allows for a change in the field strength at the same current.

The selected test-channels include two charged pions of opposite charge and a proton or neutron plus a positively charged pion which were selected as missing particles. The first channel, $\gamma p \rightarrow \pi^+ \pi^- p$, was used to identify the correction needed, because all particles are detectable by CLAS and the second, $\gamma p \rightarrow \pi^+ \pi^+ \pi^- (n)$, to verify this correction.

The changed magnetic field strength affects the energy measurement of the scattered electrons. The 4-vector of the beam photon is calculated by taking the difference of the 4-vectors of the electron beam and the scattered electron.

$$P_\gamma = P_{E_0} - P_e$$

The four-vector of the scattered electron P_e has to be corrected by a scalar factor x. Using the equation

$$
\begin{aligned}
(P_\gamma + P_{target} - (P_{\pi^+\pi^-}))^2 &= m_p^2 \\
P_{\pi^+\pi^-}^2 - 2P_{target}P_{\pi^+\pi^-} &= 2P_\gamma(P_{\pi^+\pi^-} - P_{target}) \\
\text{with } P_{target}^2 = m_p^2 \quad &\text{and} \quad P_\gamma^2 = 0,
\end{aligned}
$$

one can determine x to be

$$
x = \frac{P_{E_o}(P_{target} - P_{\pi^+\pi^-}) + \frac{P_{\pi^+\pi^-}^2}{2} - P_{target}P_{\pi^+\pi^-}}{(P_{E_0} - P_\gamma)(P_{target} - P_{\pi^+\pi^-})}
$$

The beam photon energy is then corrected by using this factor on the energy of the scattered electron. The correction factor was calculated for each run and with 1/10 of the data of each run to reduce statistical fluctuations.After the correction, the masses of the proton and neutron are less than 1 MeV off the PDG values.

3.4 Event Vertex and Fiducial Volume Cuts

The event selection for this analysis is restricted to events whose primary vertex is located inside the liquid hydrogen of the target. Because of configurations or equipment failures it may happen that the beam does not hit the liquid hydrogen contained in the target and tracks are produced which originate in the target walls or the support structures. The target for *g12* is 40 cm in length and 4 cm in diameter and was centered 90 cm upstream. To require only tracks which originated inside the liquid hydrogen it is necessary to take the tracking resolution into account. The vertex resolution in radial direction is 5 mm and in 6 mm z-direction.
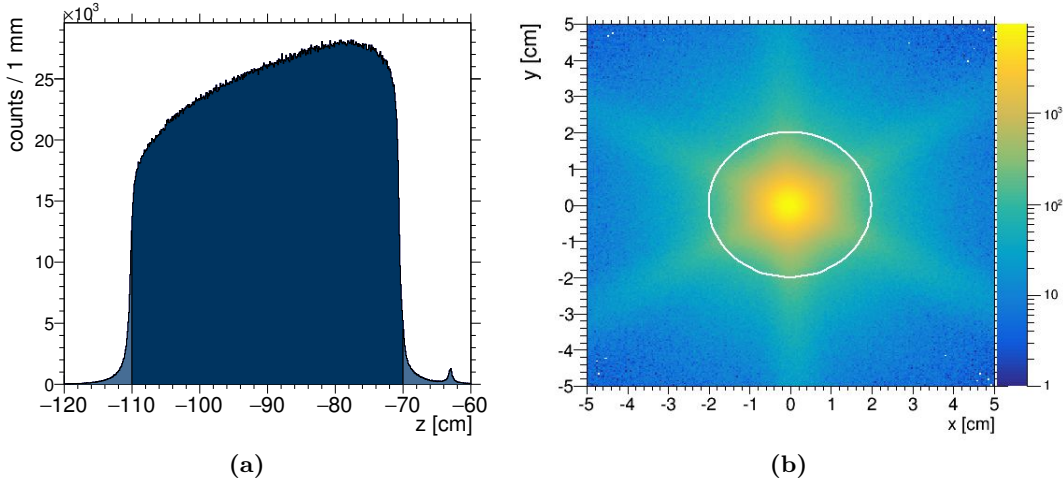

Figure 3.3: (a) z-vertex of $p\pi^+\pi^-$ events. The dark blue region contains the accepted events (b) y vertex vs. x vertex. The white circle indicates the vertex position cut.

The cuts accounting for this are listed here

- the radial distance from the central axis of the target $r = \sqrt{x^2 + y^2}$ has to be less than $2.5\,\text{cm}$

- the reconstructed common vertex of the z-position has to be within the range [-110,-70] cm

and presented in figure 3.3.

A second set of cuts on geometric parameters is called *Geometric fiducial cuts* and rejects events which occur in regions where the acceptance is not well understood and reliably reproduced in simulations. These regions are defined by an upper and lower limit of the Φ angle between the center of a sector and a track.

The fiducial boundaries of the Φ angle are defined by functions of momentum, charge and polar angle. For each sector a different set of boundaries was derived. In general the occupancy should not drop below 50% for a Φ angle between -10° and 10°, which is called the sector's flat region. The flat region is defined as $-10° < \phi < 10°$. It can be chosen between *tight*, *loose* and *nominal* cuts. For this analysis the nominal cuts were chosen and an example before and after the cut can be seen in figure 3.4.
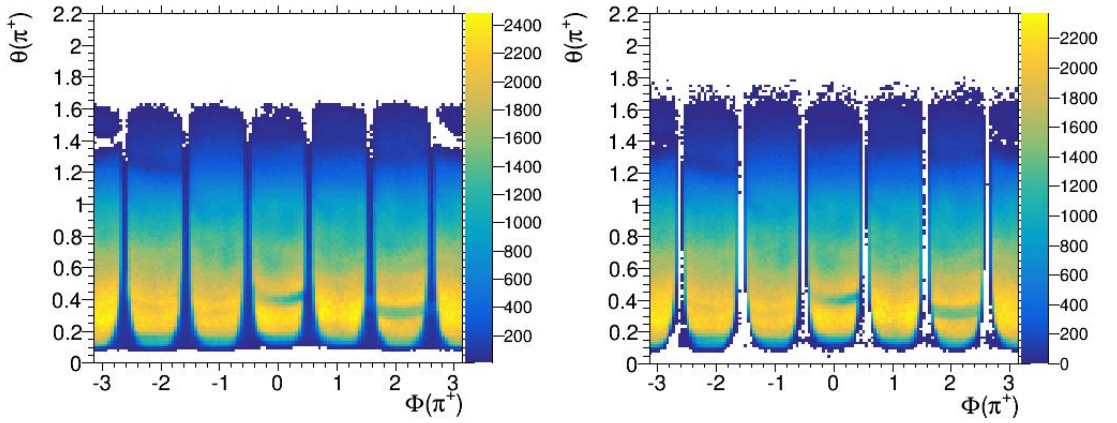

Figure 3.4: Angular distributions of $\theta(\pi^+)$ Vs. $\Phi(\pi^+)$ is shown before the fiducial volume cut (left) and after the fiducial volume cut (right).

3.5 TOF Fiducial Cuts

In some cases wrong photons are selected as responsible for the event (see Section 3.2). This can lead to wrong estimations for the start time of the event. Due to wrongly estimated start times superluminal speeds of tracks may be possible. These tracks should be removed from the data set, because they are nonphysical. The relativistic β which is the actual speed of a particle divided by the speed of light. Two cuts are applied on:

- $\beta < 1.04$
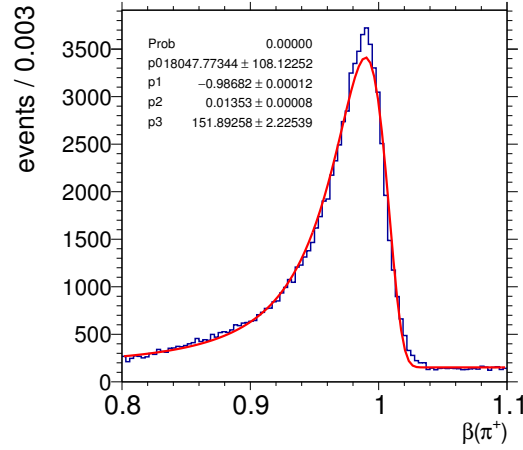
- $\delta\beta < |\beta_{meas} - \beta_{calc}|$

Figure 3.5: Fitted β distribution for π^+.

The β is chosen larger than one to take timing resolution into account. β_{meas} is solely derived from the measurements of the time-of-flight system for each reconstructed particle and β_{calc} is the calculated β using the momentum of the reconstructed particles.

To calculate the relativistic speed of a particle for a certain momentum one uses the PDG value of the mass hypothesis assigned to the particle using equation (3.5.1).

$$\beta_{calc} = \frac{p}{\sqrt{m_{PDG}^2 + p^2}} \tag{3.5.1}$$

The difference $\delta\beta$ was derived by fitting a Landau function with a constant to the β distributions of the pions. In figure 3.5 one can see the β distribution obtained for π^+ and the fitted function in red.

The extracted sigma of the function is approximately 0.0135. The cut was chosen to take all events within a 3σ region left and right of the calculated β.

In figure 3.6 the momentum of each detected particle versus the relativistic β is shown. The colored lines depict the calculated β for kaons in violet, pions/protons in black and muons in red.

Table 3.1: List of malfunctioning TOF paddles.

Sector	Paddle Number
1	6, 25, 26, 35, 40, 41, 50, 56
2	2, 8, 18, 25, 27, 34, 35, 41, 44, 50, 54, 56
3	1, 11, 18, 23 35, 40, 41, 56
4	8, 19, 41, 56
5	48
6	1, 5, 24, 33, 56

It is clearly visible that the data sample is free of charged kaons, but that there is a lepton contribution. The second plot illustrates the distribution after the applied cuts.
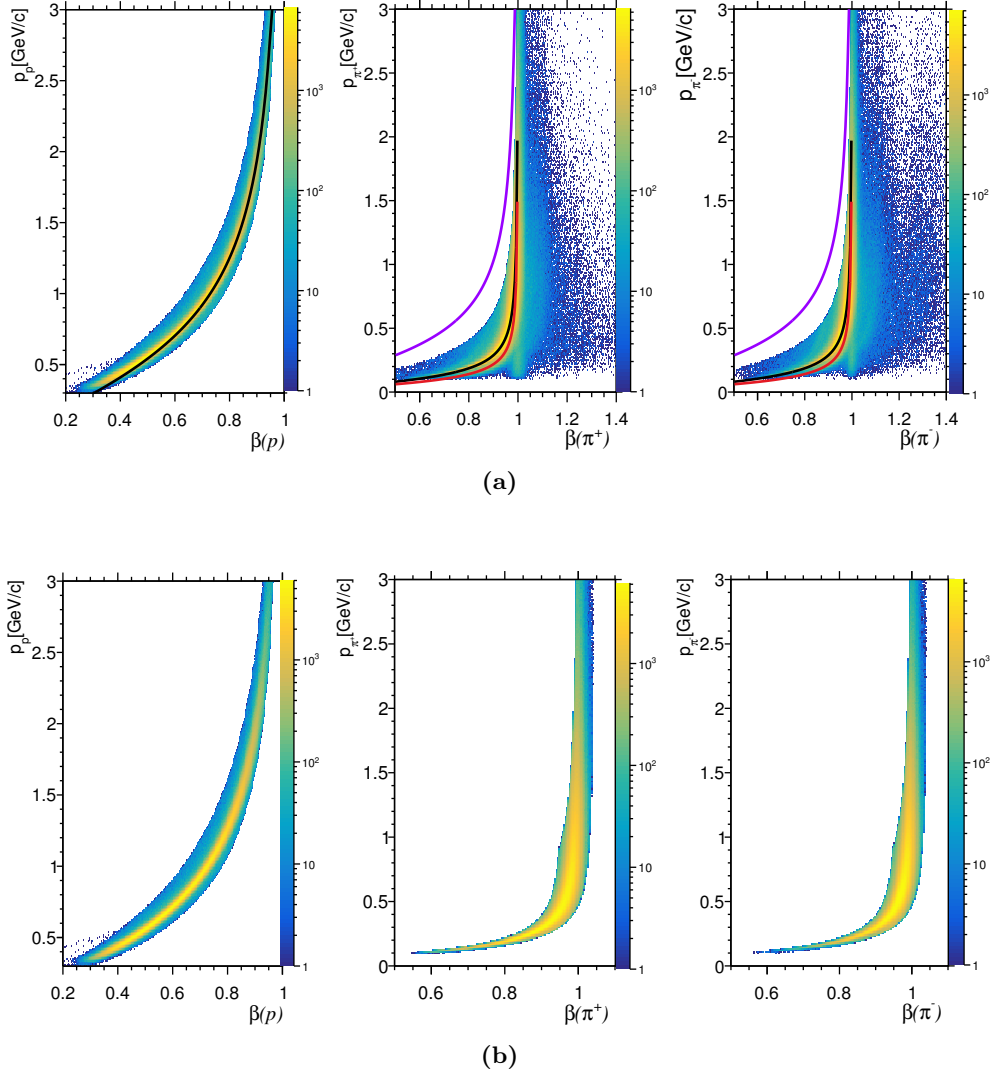
Figure 3.6: (a) Momentum of the detected particle vs. the measured β. Colored lines indicate calculated β for particles: Purple: kaons, Red: muons and Black: proton/pions (b) Momentum vs. β after cut.

The lepton band is cut out, but a pion lepton separation at high momenta is not possible. In addition to this cut some TOF paddles were found to be faulty and therefore events measured by them were removed from the further analysis procedure. The list of bad paddles is listed in table 3.1. For more information see [29].

3.6 Minimum Momenta

The momentum of all charged particles has been corrected for energy losses. The lower the momentum of the particle the more energy they lose. Therefore track reconstruction

becomes more and more difficult with decreasing momentum and the acceptance for these particles can be affected. Former studies computed a fractional difference value for Monte Carlo generated events and data.

$$A = \frac{|A_{data} - A_{MC}|}{A_{data} + A_{MC}}$$

Here A_{data} is the acceptance for a proton in the correct sector of CLAS for real physics events and A_{MC} is the acceptance for Monte Carlo events. The acceptance was calculated by using the test channel $\gamma p \rightarrow p\pi^+\pi^-$ where events with charged pions were selected and kinematically fit to the test channel. A should then be around zero if the Monte Carlo simulation accurately describes the detector acceptance. Areas which show an A deviating from zero are due to bad TOF paddles, the forward hole and low momentum tracks.

It was found that it is sufficient to cut away events where the proton has a momentum below $300\,\text{MeV/c}$ and the pions have a momentum below $100\,\text{MeV/c}$.

3.7 Kinematic Fit

In order to reduce more of the undesired contributions and to improve the resolution of our distribution a kinematic fit was performed. The kinematic fit assigns a probability nearer to one to each event in the case it originates from the reaction $\gamma p \rightarrow p\pi^+\pi^-\eta$. All measured quantities are measured within certain error limits caused by measuring uncertainties. The kinematic fit varies the measured quantities within their errors to match energy-momentum conservation and invariant mass constraints using a χ^2 minimization algorithm. The fit delivers a likelihood for each event fulfilling the desired constraints of the final state via the values of a χ^2 probability or a confidence level value.

Kinematic Fitting
The goal of kinematic fitting is to make use of the energy and momentum conservation laws to vary the values of our measured quantities within the uncertainties given by the detector to improve the precision of our measurement. The kinematic fit adjusts the physics hypotheses with a least squares method using Lagrange multipliers. As a formula this can be written as

$$\vec{\eta} = \vec{y} + \vec{\epsilon},$$

where $\vec{\eta}$ is the n-dimensional vector of our measured observables, $\vec{y}$ is the vector of our actual values and $\vec{\epsilon}$ are the deviations needed to shift the values to match the constraints. The constraints, invariant masses and the conservation of momentum and energy, can be used to deduce a certain number of unmeasured observables, as long as the number of unmeasured observables is equal or smaller than the number of constraints. The constraints can be written as

$$f(\vec{x}, \vec{\eta}) = f(\vec{x}, \vec{y} - \vec{\epsilon}) = 0,$$

where $\vec{x}$ is the m dimensional vector of unmeasured observables. $\vec{f}$ has to be linearizable at $(\vec{x}_0, \vec{\eta}_0)$ with

$$\vec{f}(\vec{x}, \vec{\eta}) = \vec{f}_0(\vec{x}_0, \vec{\eta}_0) + \frac{\partial \vec{f}}{\partial(\vec{x}, \vec{\eta})}(\vec{x} - \vec{x}_0, \vec{\eta} - \vec{\eta}_0).$$

If $f(\vec{x}, \vec{\eta})$ is linearizable then the solution with the least squares is reached when

$$\mathcal{L} = \chi^2 = \vec{\epsilon}^T C_y \vec{\epsilon} + 2\vec{\lambda}^T \cdot \left[A(\vec{x} - \vec{x}_0) + B(\vec{\eta} - \vec{\eta}_0) + \vec{f}(\vec{x}_0, \vec{\eta}_0) \right],$$

is minimal. C_y is the symmetric covariance matrix, the vector $\vec{\lambda}^T$ contains the Lagrange multipliers, A and B are matrices which contain the derivatives of the constraints at $(\vec{x}_0, \vec{\eta}_0)$ where A belongs to $\vec{x}$ and B to $\vec{\eta}$.

In this case a kinematic fit with one constraint was performed under the condition of the missing mass of $p\pi^+\pi^-$ being an η. If there are no systematic errors present the difference between the fitted value η_i and the measured value y_i should be zero when averaged over many events. This is under the assumption that if there are no systematic errors present the error should be Gaussian distributed and the error ϵ_i has the same likelihood to be positive as negative. To check for systematic uncertainties one can normalize the distribution according to

$$pull(y_i) = \frac{\eta_i - y_i}{\sqrt{\sigma^2(\eta_i) + \sigma^2(y_i)}},$$

which is called the pull distribution from now on. The values of a pull distribution should deviate around zero and they should have a width of one if the errors $\sqrt{\sigma^2}$ of the data set are set correctly. If the width is smaller or larger than one then the errors in the covariance matrix C_y have been determined too large or small. If the mean of the distribution is not positioned at zero then there are systematic uncertainties present. Those systematic uncertainties, for example background in the range of the wanted missing particle, can disfigure the pull distributions.

The second value to evaluate the probability of an event to contain the wanted final state particles is the probability or the confidence level. The values of the confidence level range from 0 to 1, where 1 indicates that the event's measured values match the corresponding values for an ideal event exactly. There are two constraints of how a reasonable confidence level value distribution should look like. The first is that the distribution of confidence level values for pure signal events, events which match all the constraints, should be flat. The signal events should be distributed according to the distribution of errors in measurement with respect to the quoted errors given in the covariance matrix. If the errors are set correctly then the signal events should be evenly distributed in the confidence level value distribution. Every event which does not match the constraints should have a probability near zero.

The data is then kinematically fit to the missing particle for the reaction of interest, in this case $p\pi^+\pi^-\eta$. One problem of the kinematic fit is its handling of background events in the missing mass spectrum of $p\pi^+\pi^-$ (figure 3.9). Most of the events directly under the enhancement at $0.547\,\mathrm{GeV/c^2}$ would probably match the kinematic constraints of the kinematic fitter, but some of them are no real η events. All events in this analysis are kinematically fitted, but the unfitted 4-vectors are kept, too. In the first step the probabilistic event weight method (section 3.9) is used to remove non signal events. In the further analysis, the probability for each event obtained from the kinematic fit can be used to refine the distributions further.

3.8 First Look to Data

After applying all needed corrections and reasonable cuts, discussed before, the resulting spectra of the missing mass distribution of $p\pi^+\pi^-$ and the invariant $\pi^+\pi^-\eta$ mass are illustrated in figure 3.7.

The left picture shows the missing mass of the $p\pi^+\pi^-$, under the consideration that the kinematics of the initial state system γp is known. An enhancement at a mass of $0.547\,\text{GeV/c}^2$ can be seen, which is identified as an η. It is clearly visible that a significant background contribution remains below the η, which passed the selection for the final state. The right picture presents the invariant mass of $\pi^+\pi^-\eta$, where a cut on the missing mass of $p\pi^+\pi^-$ has been applied in the range from 0.5 to 0.6 GeV/c^2. There are $\approx 18 \cdot 10^6$ selected $\pi^+\pi^-\eta$ events left after the cut. At a mass of $0.9\,\text{GeV/c}^2$ a narrow signal is visible. This resonance is the η', which will be used later as a reference state. The differential cross section of the η' will be extracted and compared to a previous measurement result as a proof of concept, c.f. chapter 7.

The second major enhancement can be seen at a mass of approximately $1.28\,\text{GeV/c}^2$. This signal could be originated by the $\eta(1295)$, with a nominal mass of $1294 \pm 4\,\text{MeV/c}^2$, or the $f_1(1285)$ with a nominal mass of $1281.9 \pm 0.5\,\text{MeV/c}^2$ [3].

A minor, broad bump can be seen at a mass of $1.4\,\text{GeV/c}^2$, which may be identified as $\eta(1405)$.

In chapter 6.2 the differential cross sections of both resonances will be presented along with results for the mass and width of the η'.

Figure 3.7a suggests a signal-to-background ratio of approximately 1/3. This background will infiltrate the $\pi^+\pi^-\eta$ mass spectrum and all spectra including quantities derived from the missing particle. Therefore another method is needed to reduce the background further. For this purpose an event based background subtraction is applied, which is described in section 3.9.
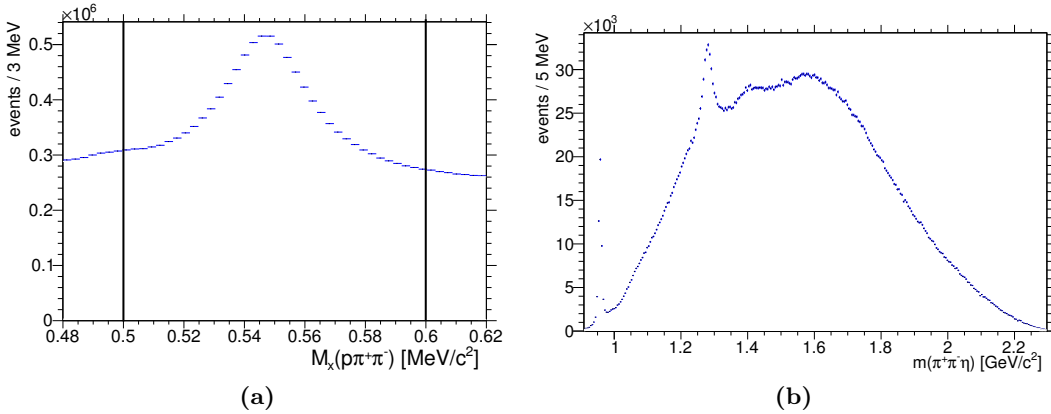

(a)   (b)

Figure 3.7: (a) Missing mass of the reconstructed $p\pi^+\pi^-$, (b) Invariant mass of $\pi^+\pi^-\eta$.

3.9 Event Based Background Rejection

Due to large background contributions in the data sample an event based background sub-traction method is used in order to reduce the background further. The afore mentioned background can not be reduced by applying cuts on observables (detailed information can be found in [30]). The main goal of the method being applied here is to obtain a probabilistic weight (Q-factor) for each event so to decide if it is a signal event or not. To subtract the background in the data sample, every event is weighted with its own Q-factor.

The method has two advantages compared to other methods, eg. a one-dimensional sideband-subtraction:

- No knowledge about the origin of the background is required

- Preserving the possibility of an event-based analysis

An event based analysis is preferable, because there is no need to group events according to one or more observables and consider them as a set. Another improvement is a better characterization of systematic uncertainties. One is no longer influenced by the chosen size of each kinematic bin which is most important for low statistic data. The biggest advantage of this method is that the probabilistic weight is coupled to an event and not to a certain observable.

The following subsections will deal with the general procedure and theoretical framework as well as an estimation of errors. In the last subsection the application of the Q-factor method to subtract background below the η and all derived quantities are explained.

3.9.1 General Procedure

All events have a common set of kinematic variables, further referred to as non-reference coordinates. The main assumption for this method is that the behavior of the background distributions does not change rapidly within a small cell of phase space and that there is no quantum mechanical interference between signal and background. The last requirement is that the non-reference-coordinates which are used to chose the nearest neighbors and the coordinate the fit is applied onto are uncorrelated. In the next step one has to define a metric to describe the position of each event in phase space based on the non-reference-coordinates. To deduce information about the behavior of signal and background distributions for each particular event one has to look at the events closest to this event in phase space, the nearest neighbors (N_{NN}). At this point the event wise procedure starts and is explained here on the example of one event called the seed-event.

To find the events closest to this seed-event a distance between two events A and B can be calculated according to

$$D_{AB} = \sqrt{\sum_i \left(\frac{\xi_i^A - \xi_i^B}{r_i} \right)^2}, \qquad (3.9.1)$$

where ξ is the kinematic variable and i the index of the kinematic variable. r_i is a normalization factor and normally selected to be the range which the phase space variable spans.
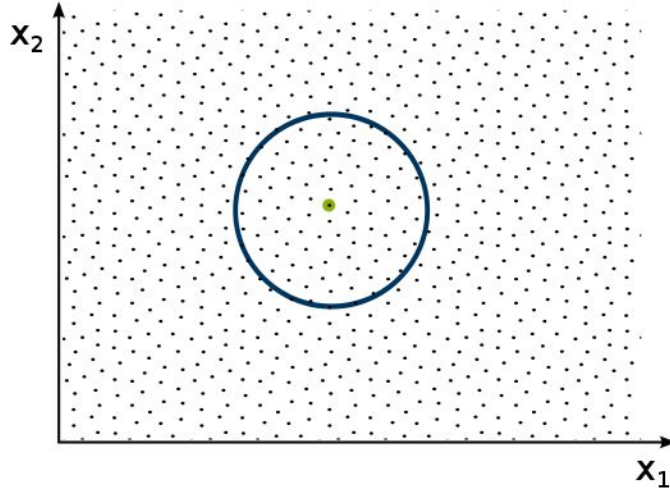
Figure 3.8: Illustration of the selection of the nearest neighbors. x_1 and x_2 represent the non-reference coordinates of a 2 dimensional phase space. The green dot is the seed-event and the black dots are all other events. In this example the events are evenly distributed in phase space and the nearest neighbors are all inside a circle of a certain radius. All events inside the blue circle are chosen as the N_{NN} nearest neighbors of the seed-event and used to define the background and signal characteristics at the seed-event's point. In reality this has not to be a circle, because the distributions of the corresponding phase space coordinates do not have to be evenly distributed.

In specific cases this factor can be chosen otherwise (see section 3.9.3), for example to achieve a better detection of narrow structures.

The number of the nearest neighbors should be chosen such that a good representation of the data is ensured. This means that enough nearest neighbors have to be chosen in order to obtain a proper fit result and few enough that the phase space cell is small enough. The statistical uncertainty for the Q-factor itself increases with a decreasing number of nearest neighbors, but the systematic uncertainty decreases. As we want the uncertainty to be as low as possible we tend to increase the number of nearest neighbors, but this increases our correlation errors as well. If the number of nearest neighbors becomes large compared to the number of events in our data sample we start averaging over a wide range of phase space. The phase space cell has to be small enough so that the signal to background ratio stays constant, which is not given for a wide range.

Additional to the non-reference coordinates the reference coordinate has to be selected which has to be uncorrelated with the non-reference coordinates. The distribution of the reference coordinate of these N_{NN} events is fitted with a signal and background function. It has to be required that the functions to describe the chosen reference coordinate are known, eg. a Breit-Wigner mass shape to describe a mass distribution.

$$f(x) = N[f_s S(X) + (1 - f_s)B(x)] \tag{3.9.2}$$
$$f(x) = N[s(X) + b(X)] \tag{3.9.3}$$

N is a normalization factor when using an unbinned maximum likelihood fit, f_S is

the signal fraction, $S(X)$ is the function for the signal and $B(X)$ is the function for the background. The signal fraction has a value between 0 and 1 and is the relative amplitude of signal and background functions. The unbinned maximum likelihood method is used to obtain the fit parameters. Using these fit parameters, $s(X)$ and $b(X)$ can be calculated at X the mass of the seed-event. With these numbers Q can be computed according to equation (3.9.4)

$$Q = \frac{s(X)}{s(X) + b(X)} \qquad (3.9.4)$$

3.9.2 Error Estimation

The error of the Q-factor can be deduced by the errors of the fit parameters. Those errors can be propagated to the measured quantities. The error for each Q-factor can be calculated in consideration of the covariance matrix, $(C_\eta)_{ij}$ associated with each fit, as well as the partial differentiation of Q with respect to the fit parameters.

$$\sigma_Q^2 = \sum_{ij} \frac{\partial Q}{\partial \eta_i} (C_\eta)_{ij} \frac{\partial Q}{\partial \eta_j}. \qquad (3.9.5)$$

To extract any observable the data set has to be subdivided into subranges of an observable. This binning leads to an error for each bin called *statistical* error. This statistical error for each bin is approximately the square root of the number of entries in each bin for Possion statistics if N is not too, small.

$$\sigma_{stat} = \sqrt{N_{Signal}} \qquad (3.9.6)$$

$$N_{Signal} = \sum_i Q_i \qquad (3.9.7)$$

For weighted Poisson statistics the error of each bin is

$$\sigma_{stat} = \sqrt{\sum_i Q_i^2} \qquad (3.9.8)$$

If all weights are one then we get the error σ_{stat} stated in equation (3.9.6). To explain how and why the error of the Q-factor has to be taken into consideration as well, we will take out one bin containing N events.

Each event is highly correlated with most of the other events due to the Q-factor procedure. Every Q-factor value is correlated to the chosen nearest neighbors. It depends on how many neighbors are chosen and how big the available phase space is. If a smaller phase space is considered and thus a lower number of events, then most of the events share most of their nearest neighbors with other events. This leads to a high correlation between each event and its nearest neighbors. Hence a 100% correlation between the events is chosen in order not to underestimate the error.

$$\sigma_{signal} = \sum_i^N \sigma_{Q_i} \qquad (3.9.9)$$

This leads to an overestimation of the error. To take the real correlation between the events into account one can calculate the number of shared nearest neighbors from each event to all other events and divide this by the number of chosen nearest neighbors.

$$\sigma_{Signal}^2 = \sum_{ij} \sigma_{Q_i} \rho_{ij} \sigma_{Q_j}, \tag{3.9.10}$$

where σ is the error of the Q-values for event i and j and

$$\rho_{lk} = \frac{N_{common}}{N_{NN}}, \tag{3.9.11}$$

with N_{common} the number of the shared nearest neighbors and N_{NN} the number of nearest neighbors. As the number of shared nearest neighbors has to be looked up for each event one can assume a large expenditure of time to do this. Therefore, the first method with the overestimation of errors has been chosen according to equation (3.9.9) and the bin wise error results in

$$\sigma_N^2 = \sigma_{stat}^2 + \sigma_{Signal}^2. \tag{3.9.12}$$

3.9.3 Background Rejection for $M_x(p\pi^+\pi^-)$

The CLAS detector is not able to detect photons, and therefore the η can not be detected. Nevertheless the missing mass of the $p\pi^+\pi^-$ system shows an enhancement at the mass of the η, which can be seen in figure 3.9.

As one can see the peak is afflicted with a huge background contribution. On the left side of the peak at the η mass a small structure is visible caused by a contribution of neutral kaons as a part of the background.

The non-reference coordinates used to get the positions in phase space for each event are listed in table 3.2. These coordinates are chosen as a base to describe the phase space for the reaction $\gamma p \rightarrow p\pi^+\pi^=\eta$ as detailed as possible.
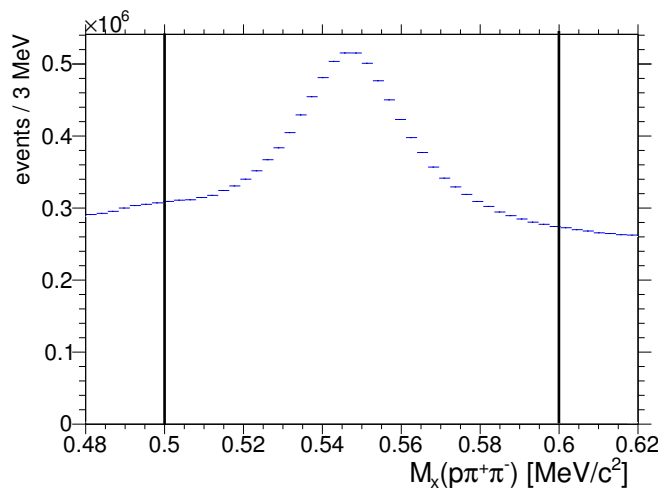
Figure 3.9: Missing mass of $p\pi^+\pi^-$.

Quantity	Non-Reference-Coordinates
Beam Energy	E_γ
η' production angle	$\cos(\theta_{\eta'}^{c.m.})$
Angular Distributions	$cos(\theta)_{\pi^-\pi^+}^{\pi^+}, cos(\theta)_{MM\,\pi^+}^{\pi^+},\ cos(\theta)_{MM\,\pi^+\pi^-}^{\pi^+\pi^-},\ \Phi_{\pi^+MM}^{\pi^+}, \Phi_{MM\,\pi^+\pi^-}^{\pi^+\pi^-}$
Invariant Squared Mass	$\mathrm{m}^2(\pi\,\pi\,MM)$

Table 3.2: Kinematic variables used in the background Rejection with $M_x(p\pi^+\pi^-)$ as reference-coordinate. MM stands for the missing mass of $p\pi^+\pi^-$.

To obtain the Q-factor for a certain event one has to identify the nearest neighbors. This can be realized by simply calculating the distances between two events among each other. This procedure can be parallelized, using subsets of the data for the seed-events, but using the whole sample for choosing nearest neighbors. This improves the run time a lot, but is still not enough to gain results in a reasonable amount of time.

To avoid this time-consuming procedure another assumption was made. The nearest neighbors and the seed-events occupy the smallest cell in phase space possible. Therefore, all distances in all non-reference coordinates have to be as small as possible. Consequential it is possible to realize a preselection of events in dependence of the corresponding beam energy. A simple binning would cause sharp edges in phase space and can lead to non-optimal results. The non-optimal results can happen if the seed-event is near the bin edge, but the nearest neighbors can only be chosen from inside the bin, but some events in the next bin would have been more suitable. Another problem can happen due to the bremsstrahlung distribution of the beam energies which leads to varying event numbers per bin. In the low energy regime it can happen that the fraction between N_{NN} and the event number is not good enough to account for correlation effects and the phase space cells are getting unreasonable big.

To avoid the before mentioned sharp edge effects an overlapping binning is used. An explanatory drawing is presented in figure 3.10.

In addition to each *seed-events-bin* two slices left and right of this bin are chosen containing
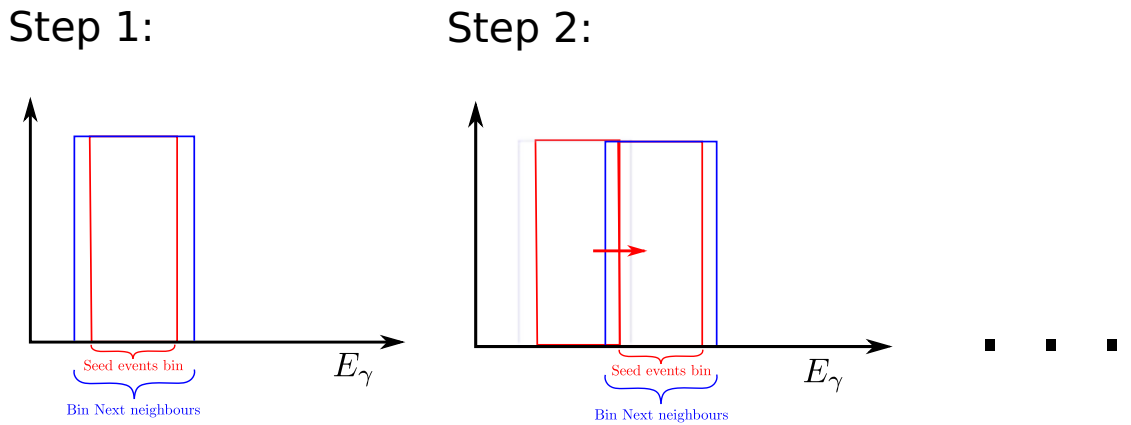
Figure 3.10: Schematic drawing of the overlapping bins. The red dotted bin depicts the seed-events-bin and the blue lines indicate the slices next to it.
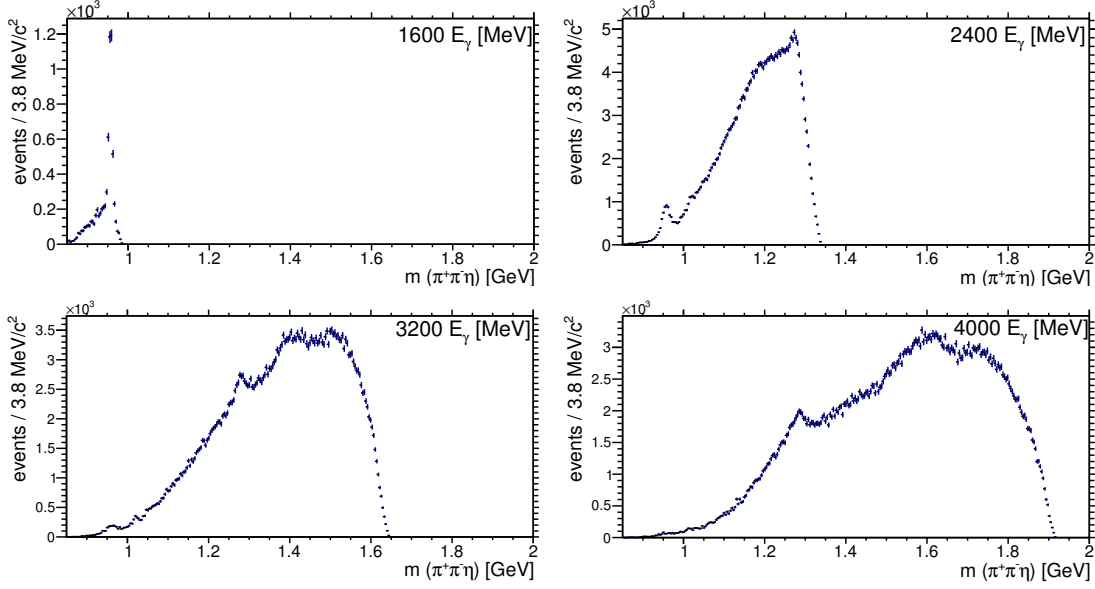
Figure 3.11: Invariant mass of $\pi^+\pi^-\eta$ in different bins of E_γ, each $100\,\text{MeV}$ wide.

an additional event set. The number of events per slice is calculated to contain 5% of the number of entries in the *seed-events-bin*. For every event in the *seed-events-bin* its nearest neighbors are selected. The nearest neighbors can get selected inside the seed-events-bin and the slices next to it. The next bin, step 2, has its left border exactly at the same energy as the right border of the former *seed-events-bin*. Accordingly its left slice contains events of the former seed-events-bin. And in this way the whole data set is "binned". Several values for the fraction of the number of the events of the slices were tested and 5% was good enough to avoid edge effects and a larger value did not improve the results further.

In figure 3.11 the invariant mass of $\pi^+\pi^-\eta$ is shown for different ranges of beam energies. One can clearly see that the size of the covered phase space becomes larger with increasing beam energy. Since the squared invariant mass of $\pi^+\pi^-\eta$ is a part of the metric the normalization of this property has to be dynamically according to the beam energy. Therefore, the mass range covered by the invariant $\pi^+\pi^-\eta$ mass is calculated according to

$$\alpha = \sqrt{2m_p E_\gamma + m_p^2} - m_p - 2m_{\pi,PDG} + 2m_{\eta,PDG},$$

where α is the normalization factor and m is the invariant mass. E_γ is the beam energy at the end of the given bin or the highest possible energy for this bin. $\sqrt{2m_p E_\gamma + m_p^2}$ is the center of mass energy of the $E_\gamma p$ system.

It is visible that the structure representing the η' is rather narrow compared to the complete covered mass range of the $\pi^+\pi^-\eta$ mass at higher beam energies. In order to resolve such narrow structures an additional factor is used, which has been empirical determined and is multiplied to α. Thus, different values of the multiplicative factor have been tested for each energy range afterwards the factor has been chosen which ensured the
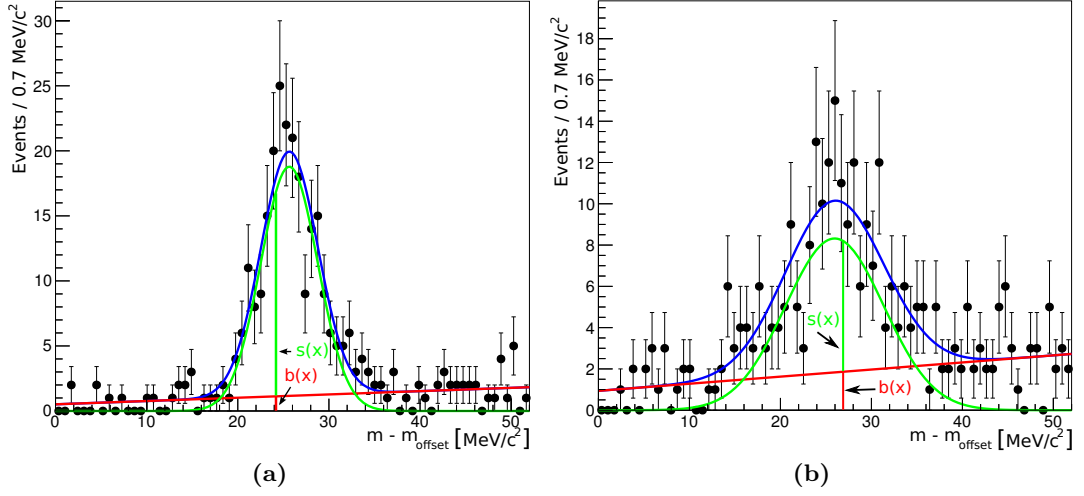
Figure 3.12: Examples of a fits to 200 nearest neighbors. The black points represent the
mass shape of the nearest neighbors, the blue line indicates the combined
PDF of signal function and background function, the green line stands for
the signal function and the red line for the background function. The vertical
green and red lines represent the values of both functions at the mass of the
seed-event and represent $s(X)$ and $b(X)$.

best background subtraction. These factors were plotted against the corresponding beam
energy of the certain energy range. The factors were found to perform an exponential
distribution. This distribution was fitted with an exponential function, which allows a
continuous and dynamic calculation of the needed value. The parametrization was found
to be:

$$e^{2.65-1.65E_\gamma} \ .$$

In this case E_γ is the value between the lowest possible energy of the bin and the highest
possible one.

Another huge leverage effect on the quality of the background subtraction is related to
the chosen number of chosen nearest neighbors. Several different number for N_{NN} were
tested, like 50, 100, 150, 200, 250, 300, 400 ,500.

It turned out that 200 nearest neighbors are the optimal choice, because this number
guarantees the best trade-off between the statistical and systematical error. Examples
of fits to 200 nearest neighbors can be seen in figure 3.12 including the fitted functions.
The left example has a huge signal fraction compared to the background. For samples of
the nearest neighbors where the signal-to-background ratio is less good, cf. figure 3.12
b), the statistical uncertainties of the Q-factor rises..

The fit is performed by making use of an unbinned maximum likelihood fit. The function
chosen for the fit are the sum of:

- First order Chebychev polynomial for the background

- Gaussian for the signal
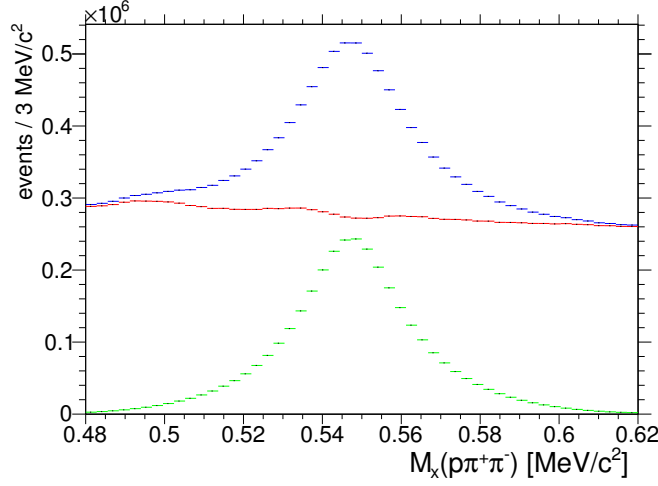
Figure 3.13: Missing mass of $p\pi^+\pi^-$. Blue: Unweighted, Green: Q weighted and Red: 1-Q weighted.

A simple Gaussian is preferred over a Voigtian function because of the large width of the peak representing the η. The η has a natural width of $1.3\,\text{keV}$, and therefore the width of the signal is dominated by the detector resolution.

The parameters of the Gaussian

$$s(x) = e^{-\frac{(x-\mu)^2}{2\sigma^2}}$$

can vary; the mean (μ) between $\pm 3\,\text{MeV}$ around the PDG mass of the η and the width (σ) between $4\,\text{MeV/c}^2$ and $26\,\text{MeV/c}^2$. The amplitude of the signal has no boundaries during the fit.

The probabilistic event weight can then be calculated according to equation (3.9.4). A background subtracted spectrum of an observable can be obtained by weighting each event's contribution to the distribution of the observable with the obtained Q-factor.

The good background rejection power can be seen in in the spectrum of the missing mass of $p\pi^+\pi^-$ (figure 3.13).

As one can see the Q-weighted distribution contains nearly no background any more. The red points show the spectrum weighted with 1-Q and represent the subtracted background. The smooth background distribution and the clear peak for the signal are a reliable result for the event-based background subtraction.

As mentioned before the Q-factor method enables us to reduce the background in any distribution of observables, and consequently also in the $\pi^+\pi^-\eta$ mass spectrum.

Figure 3.14 shows the former $\pi^+\pi^-\eta$ mass spectrum in blue. The errors are the squared sum of the statistical error and the errors of the Q-factors, c.f. equation (3.9.12). The background below the η' signal has been reduced to a negligible amount, which is very convenient for the comparison to previous measurements of the η' differential cross sections. It is visible that the massive background contribution, visible in red, is reduced by factor of two in the $f_1(1285)/\eta(1295)$ region. The signal-to-background ratio has been improved from approximately 1:3 to 1:1.2. The rise at a mass of $1400\,\text{MeV/c}^2$ is clearly
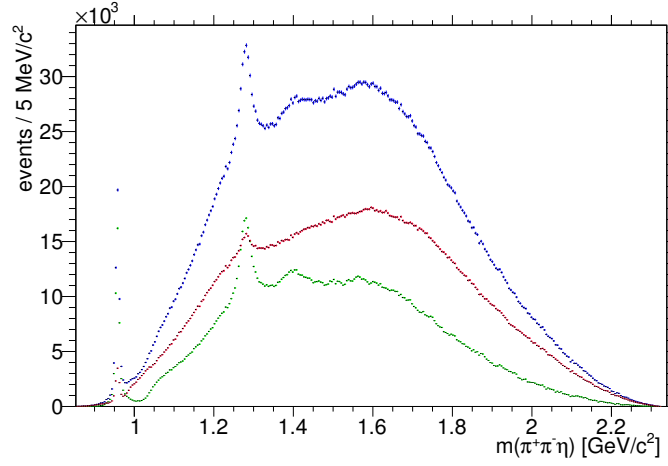
Figure 3.14: Invariant mass of $\pi^+\pi^-\eta$ weighted with Q-factors. Blue: Unweighted, Green: Q weighted and Red: 1-Q weighted.

identified as signal structure, as it is visible only in the Q-weighted spectrum while the 1-q weighted distribution shows no structure in this region. The enhancements are more emphasized and refined. The 1-Q weighted distribution shows a smooth behavior, which is an indication that most of the non-resonant background has been identified.

This is also visible if one applies a cut on the η mass in the range from $0.53\,\mathrm{GeV/c^2}$ to $0.57\,\mathrm{GeV/c^2}$ to select events which are in the signal region. Secondly two cuts are applied right and left from the η mass to select events from sidebands: $0.48\,\mathrm{GeV/c^2}$ – $0.5\,\mathrm{GeV/c^2}$ and $0.6\,\mathrm{GeV/c^2}$ – $0.62\,\mathrm{GeV/c^2}$. The events from the signalband get weighted with Q as well as 1-Q while the events from the sidebands stay unweighted. The resulting distributions for a chosen energy range are shown in figure 3.15, where it is visible that the cyan and brown distributions show nearly the same behavior.
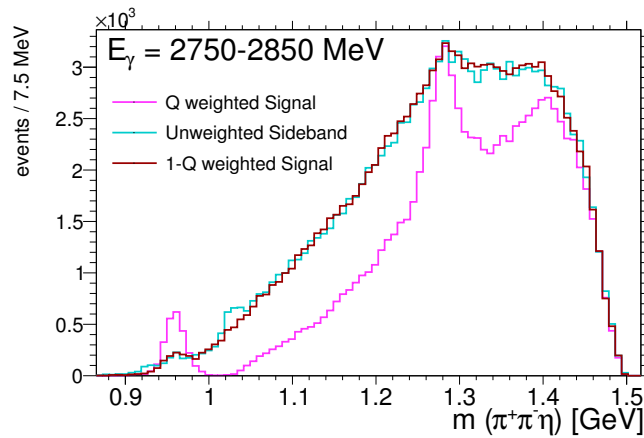
Figure 3.15: Signalband weighted with Q-factors. Magenta: Q weighted and Brown: 1-Q weighted. Cyan: unweighted sideband.

4 Background Contribution

In the previous section it has been shown that the selected data sample is afflicted by a massive background contribution. As mentioned before the main goal of the event selection is to select as much as possible events of the desired decay mode and reject as many events as possible of the background. Nevertheless, it is not possible to reject all background events, and therefore the data sample has been studied for potential background sources and their amount in the selected data set.

The background visible in figure 3.13 is a mixture of events where the wrong PID is assigned to the tracks as well as particles assigned to the wanted reaction, but coming from another one. Another source of background are particles of a competing reaction that are mistaken for participating in the wanted reaction. Background accepted as signal can take place if the kinematic observables match the requirements for a signal event. The reconstructed channel is prone to this, because the η is not reconstructed, but derived from the missing mass. It may happen that neutral particles in other reactions have the same kinematics as the wanted η meson.

In figure 4.1 the missing mass of the proton is plotted against the missing mass of $p\pi^+\pi^-$.
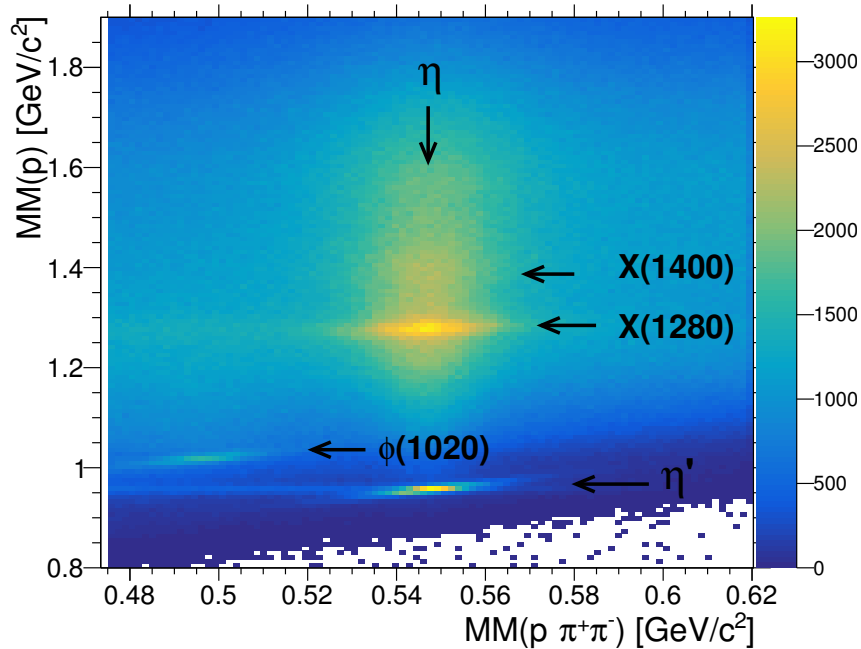
Figure 4.1: Missing mass of the p versus missing mass of $p\pi^+\pi^-$.

<div align="center">**Table 4.1:**</div>

Final State	$prob >$	events passing [%]	Branching Fraction Γ_i/Γ [%]	Total Cross Section σ [%]
$p\pi^+\pi^-\gamma$	0.1	$0.0075\ 10^{-3}$	29.3	$2.19 \cdot 10^{-6}$
	0.01	$0.015\ 10^{-3}$		$4.39 \cdot 10^{-6}$
	0.001	$0.0225\ 10^{-3}$		$6.59 \cdot 10^{-6}$
	0	$0.0775\ 10^{-3}$		$22.5 \cdot 10^{-6}$
$p\pi^+\pi^-3\gamma$	0.1	0.021	2.75	$5.775 \cdot 10^{-7}$
	0.01	0.033		$9.075 \cdot 10^{-7}$
	0.001	0.045		$12 \cdot 10^{-7}$
	0	0.14		$39 \cdot 10^{-7}$
$p\pi^+\pi^-5\gamma$	0.1	0.193	21.6 (η')· 4.6 (η)	0.000019
	0.01	0.303		0.00003
	0.001	0.392		0.000039
	0	1.35		0.00013
$p\pi^+\pi^-6\gamma$	0.1	0.44	21.6 (η')· 22.74 (η)	0.0002
	0.01	0.675		0.0003
	0.001	0.86		0.0004
	0	2.57		0.0013
$p\pi^+\pi^-\eta$	0.1	0.7	43.4	0.003
	0.01	1.07		0.0046
	0.001	1.3		0.0056
	0	2.98		0.013

A prominent peak can be seen at the crossing of the η and the η', but there is also a horizontal band crossing through this peak.

This horizontal band is caused by background events and causes background directly beneath the η' as well. A similar band is crossing through the peak at the η mass and a mass of $1280\,\mathrm{MeV/c^2}$ for the missing mass of the proton. Another enhancement is visible at $1020\,\mathrm{MeV/c^2}$ in the missing mass of the proton. This structure is positioned at a missing mass of $p\pi^+\pi^-$ of $\approx 500\,\mathrm{MeV/c^2}$ which leads to the assumption that this structure is attributed to $\phi(1020) \to K_S\overline{K}_L$. To estimate the background contribution of several other decay channels to the data set, Monte Carlo studies have been performed including the decay modes:

$$\gamma p \to p\eta' \to p\rho^0\gamma \to p\pi^+\pi^-\gamma$$
$$\gamma p \to p\eta' \to p\omega\gamma \to p\pi^+\pi^-\pi^0\gamma \to p\pi^+\pi^-3\gamma$$
$$\gamma p \to p\eta' \to p\pi^0\pi^0\eta \to p\pi^0\pi^0\pi^+\pi^-\gamma \to p\pi^+\pi^-5\gamma$$
$$\gamma p \to p\eta' \to p\pi^0\pi^0\eta \to p\pi^0\pi^0\pi^+\pi^-\pi^0 \to p\pi^+\pi^-6\gamma$$

The η' has been chosen as reference channel. For every channel 400k events were generated and then smeared and propagated through the simulation of the detector. After this the events were selected with the same selection procedures and corrections as applied to
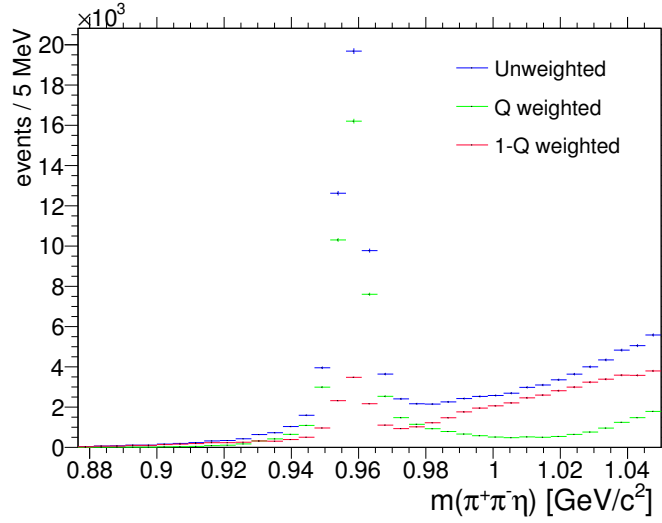
Figure 4.2: Invariant $\pi^+\pi^-\eta$ mass. The blue line indicates the unweighted distribution, the red line indicates the 1-Q weighted spectrum and the green line shows the Q weighted spectrum.

real data and a 1C kinematic fit (section 3.7) was conducted with the requirement of an η appearing in a sub-range of the missing mass of $p\pi^+\pi^-$. In table 4.1 the fraction of the passing events are presented after different cuts on the kinematic fit probability.

It is clearly visible from the number reported in the table 4.1 that it is possible to select events where the η' has decayed into $\pi^0\pi^0\eta$ with an efficiency about a magnitude lower than that for the signal decay$\eta' \to \pi^+\pi^-\eta$ mode, but one should not underestimate the contributions of this channel. In this case the η decays to $\pi^+\pi^-\pi^0$, adding two charged pions to the final state. If the neutral pions of the η' decay have nearly the same kinematics as the charged pions of the η decay, they can be interchanged. The decays including a ρ or ω are rather unlikely to contribute to the peaking background.

In figure 4.2 the invariant $\pi^+\pi^-\eta$ mass is shown. The green and red lines are the spectrum weighted with Q and 1-Q and the red distribution features a peak directly in the η' mass region.

This might be a hint on events from competing channels which have been rejected by using the probabilistic event weight background rejection on the η. The yield of the η' in the green distribution as well as the signal yield of the red distribution have been estimated by fitting a Gaussian function plus a third order polynomial in order to exclude non-resonant background. The signal yield of the Q weighted distribution was found to be ≈ 50000 η' events and the signal yield of the η' in the background distribution was found to be ≈ 4000 events after a probability cut of $prob > 0.1$. The ratio of simulated signal events to wrongly chosen Monte Carlo events after the same selection criteria is ≈ 13.6. The ratio of the signal yield of the 1-Q weighted $\pi^+\pi^-\eta$ mass distribution to the signal yield of the Q-weighted distribution is ≈ 12.5.

In order to verify if the Q-factor background subtraction is able to filter those kinematic permutations one can compare, from a mass window selected, signal events weighted with Q and 1-Q with events that are possible background and got selected from a sideband.
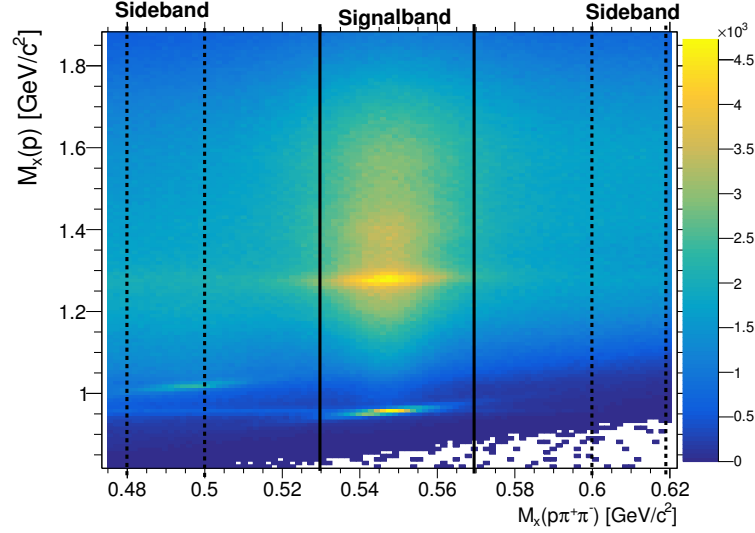
Figure 4.3: Invariant mass of $\pi^+\pi^-\eta$ versus η. The lines are indicating the cuts applied for selecting events in a signal band and sidebands half the width of the signal band.

For this test two cuts were applied on the missing mass of $p\pi^+\pi^-$ which are depicted in figure 4.3.

The black lines contain events from the signal band while the events between each of the two the black, dashed lines contain events of the sidebands and each sideband has half of the width of the signal band width. The events between the black lines are weighted with Q and 1-Q and the events between the black, dashed lines remain unweighted. In figure 4.4 those events are filled in one-dimensional histograms with the missing mass of the p on the x-axis. The events are sorted in bins of the beam energy of 100 MeV each. To demonstrate how well the Q-factor method is able to subtract background one has to compare the 1-Q weighted events from the signalband and the unweighted events from the sideband. It is clearly visible that both distributions show nearly identical behavior. The enhancement at a mass of $1.020\,\text{GeV/c}^2$ is only visible in the distribution of the sideband. As one can see in figure 4.1 these are events with $\phi \rightarrow K_S\overline{K}_L$ and it is positioned to the left of the η, because it decays to neutral kaons, and therefore cannot be seen in the signal band. The conclusion is that the horizontal bands crossing the resonances can be rejected well by using the Q-factor method on the η.

But nevertheless, one can see much possible non-resonant background at higher masses. As a conclusion there are contributions from wrongly assigned identities of particles, but most of it can be subtracted by using the Q-factor method on the η.
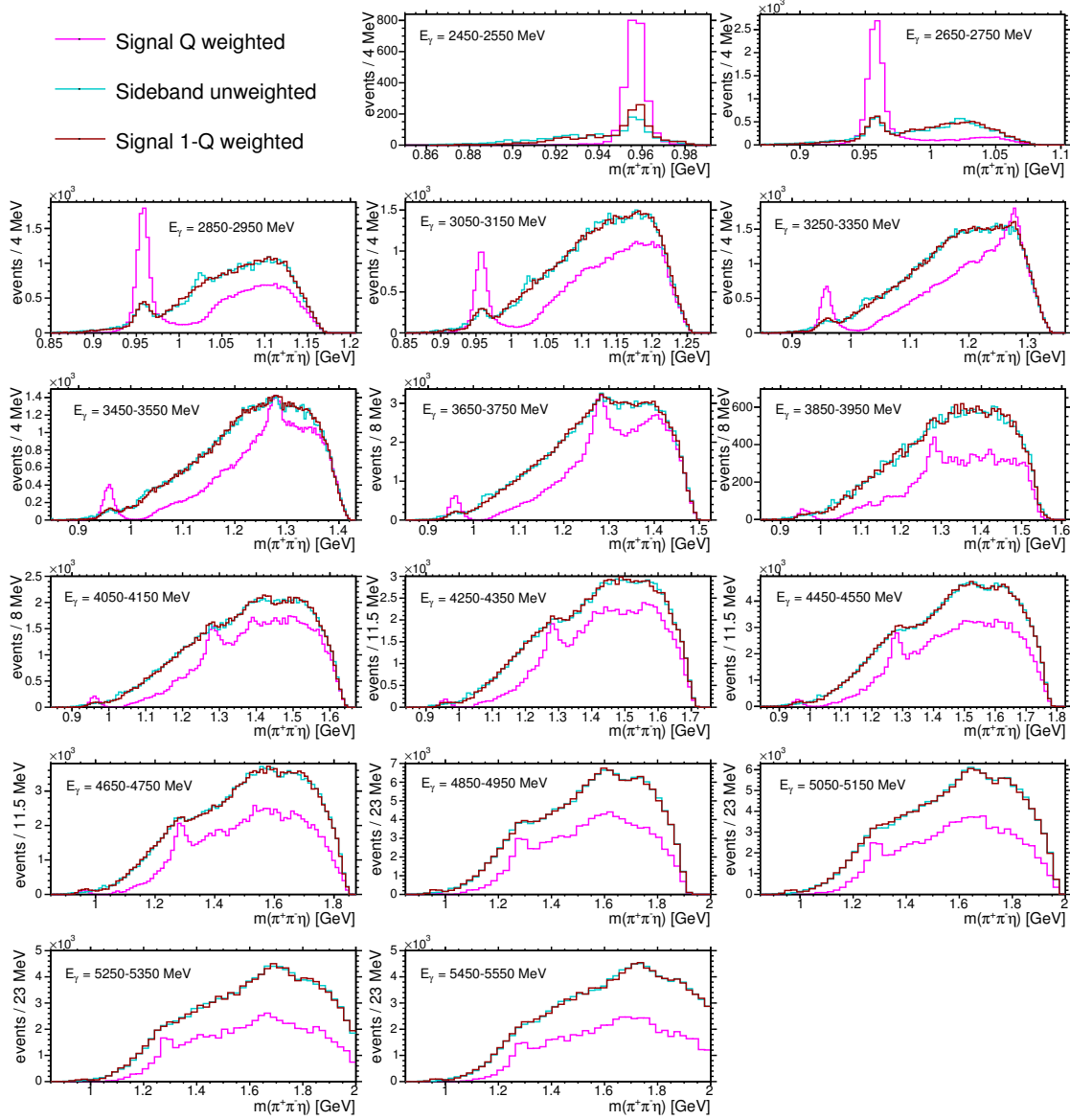
Figure 4.4: Invariant $\pi^+\pi^-\eta$ mass. Each plot covers $100\,\text{MeV}$ intervals of the beam photon energy. The green magenta depicts events of the signal band weighted with Q and the brown line those with 1-Q weighted. The cyan line presents the unweighted events of the sideband. In the upper part the mean beam energy for the corresponding bin is displayed.

5 Contribution of Baryon Resonances

In photon-proton reactions a high possibility exists to produce baryon resonances beside the discussed meson resonances. Baryons are mainly produced via the s-channel production process. In this case the intermediate resonance is a baryon, for example a N^* which decays to a proton and a meson.

To get a clue if and in what strength baryon resonances might contribute one can take a look at invariant mass spectra including the proton in combination with the three mesons of the final state.

In figure 5.1 one can see two similar spectra. The left one shows the invariant mass of $p\eta\pi^+$ on the y-axis and $p\pi^+$ on the x-axis. Perpendicular to the x-axis at a mass of $\approx 1230\,\mathrm{MeV/c^2}$ one can see a band with a structure at a mass of $\approx 1900\,\mathrm{MeV/c^2}$ on the y-axis. The bulge has a width of about $120\,\mathrm{MeV/c^2}$ on the x-axis projection. For the projection on the y-axis one could not make a clear statement about the width, because the enhancement lies at the border of phase space. But the position of the peak indicates a $\Delta(1910)$ resonance which decays with a branching fraction of about 9% to $\Delta^{++}(1232)\eta$ which appears in the peak of the enhancement in the x-axis projection. The right plot in figure 5.1 shows the same, but the π^+ is replaced by the π^-. In this case no structure affiliated with a certain resonance is visible.

In consideration of the Clebsch-Gordan coefficients one can calculate that the production of a $\Delta^0(1232)$ is suppressed with respect to the $\Delta^{++}(1232)$, which might explain the absence of structures in figure 5.1b.

To gain further insight of how these baryon resonances might effect the yields of the enhancements in the invariant $\pi^+\pi^-\eta$ spectrum the figures 5.2 are presented.

All three histograms display the invariant mass of $\pi^+\pi^-\eta$ on the y-axis and on the

           (a)   (b)
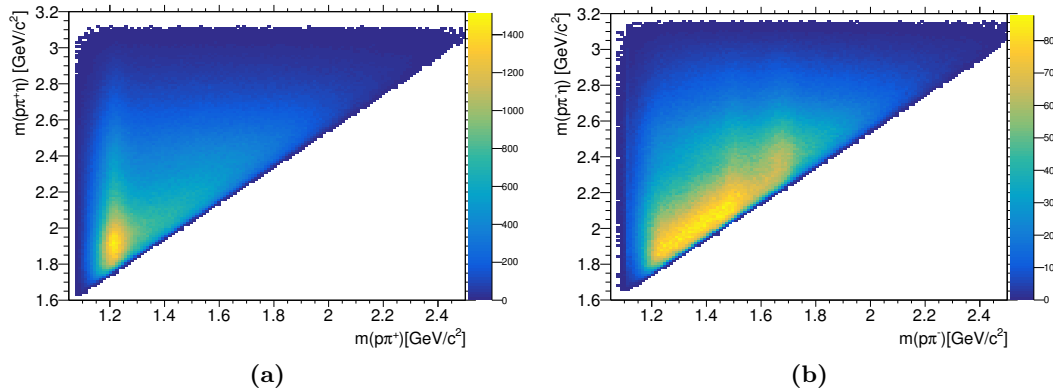
Figure 5.1: (a) The x-axis shows $m(p\pi^+)$ and the y-axis $m(p\pi^+\eta)$.
                    (b) In this case the π^+ is exchanged for a π^-.
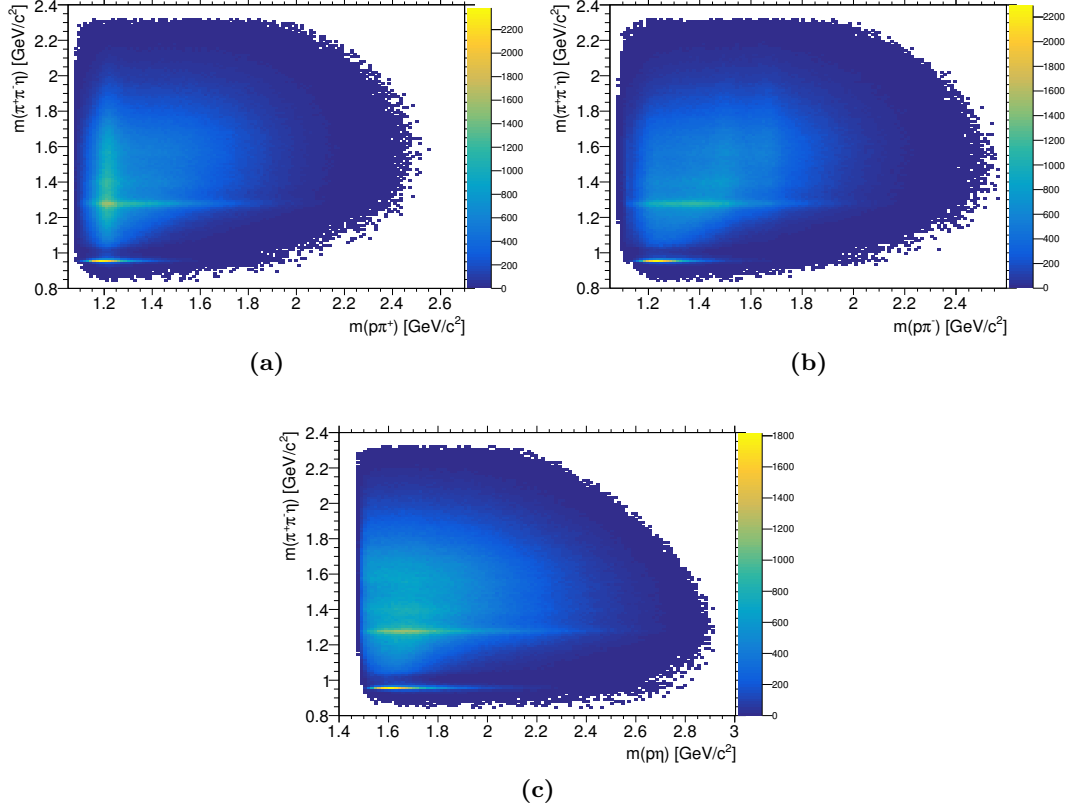
Figure 5.2: Both histograms have the invariant $\pi^+\pi^-\eta$ mass on the y-axis and on the x-axis (a) $m(p\pi^+)$, (b) $m(p\pi^-)$ and (c) $m(p\eta)$.

x-axis the invariant mass of the proton plus one of the other three final state mesons. If baryon resonances contribute to the yields of the enhancements the spectra should show vertical bands or enhancements crossing the masses of the seen resonances. In the histogram including the π^+ one can see a vertical band passing below both enhancements at a $\pi^+\pi^-\eta$ mass of $1280\,\mathrm{MeV/c^2}$ and $1415\,\mathrm{MeV/c^2}$. This broad vertical band can be assigned to the before mentioned baryon $\Delta^{++}(1232)$ and seems to contribute to the background beneath the $X(1280)$ and $X(1400)$. No such vertical band is visible in the similar spectrum for the π^-, because of the reasons mentioned before.

For the histogram with the invariant mass of $p\eta$ on the x-axis there is no vertical band visible either which might hint on a baryon contribution.

6 Study of the $\eta(1295)/f_1(1285)$ and $\eta(1405)$

The study of the $\eta(1295)/f_1(1285)$ and $\eta(1405)$ includes several steps.

For the two resonances at higher masses a cross section will be extracted. The cross section is an effective area proportional to the likelihood of an interaction between particles. In particle physics, especially photoproduction experiments, the likelihood of the production of a particle per unit of solid angle and per beam photon energy is measured. The extraction of the cross section involves the estimation of the number of measured events per resonance and its normalization to all produced particles (equation (7.2)). The number of events is determined by fitting a model to the $\pi^+\pi^-\eta$ mass shape and is described in section 6.1.4.

This fit grants the possibility to release parameters like the mass and intrinsic width of the fitted function, to acquire knowledge about the possible identity of the fitted mass shape representing a resonance. This comes handy to gain further clarification if the seen first enhancement might be a $\eta(1295)$ or $f_1(1285)$.

6.1 Normalization

The values of a differential cross section are influenced by detector properties as well as branching fractions and binning effects. To extract a correct cross section one has to account for all these influences. The differential cross section can then be calculated according to

$$\frac{d\sigma}{d\Omega} = \frac{Y}{2\pi\, N_\gamma\, \rho\, l\, A_{CLAS}\, \Delta_{cos\theta_{CM}}\, \mathcal{B}} \ ,$$

where Y is the yield of the desired particle (cf. section 6.1.4), N_γ is the number of photons hitting the target (cf. section 6.1.1), ρ and l are the density and length of the CLAS $g12$ target (cf. section 6.1.2), A_{CLAS} is the acceptance and efficiency of the CLAS detector (cf. section 6.1.3) and $\Delta_{cos\theta_{cm}}$ is the bin width of the distribution in cosine of the production angle in the center-of-mass frame.

The yield of the particle is corrected by the appropriate branching fractions $\mathcal{B}$ of the produced resonance. For $X(1280)$ and $X(1400)$ it is not possible to include the branching fraction of $X(1280)$ and $X(1400)$ decaying to $\pi^+\pi^-\eta$ since there is no confirmed knowledge about the identity of the resonances. But it is possible to take the branching fractions of η decaying to further states into account. The second level branching fractions, the decay possibilities of the final state η, are not taken into the normalization by an exact number because they are accounted for by simulating all strong contributing decay modes according to their branching fractions.

6.1.1 Photon Flux

An accurate knowledge of the total number of photons that hit the target is mandatory for the accurate determination of the cross section. The procedure to calculate the incident photon flux measured by the CLAS tagger has been established in the *gflux* package. Further information can be found in [31] and [32].

The method calculates the number of photons by reconstructing the number of electrons striking a given T-counter from the rate of electrons in a given time window and compares them to the number of photons measured at the target by a total absorption counter. These numbers are further corrected for the livetime as well as photon loss in the tagger radiator foil and the target. The livetime is the time during the DAQ was ready to record events from the CLAS detectors. This measurements are conducted during normalization runs. For this analysis the flux was binned in $10\,\mathrm{MeV}$ energy ranges and was later rebinned and integrated for the energy interval shown in the differential cross sections. Problems arose from dead photomultipliers at the paddles responsible for beam energies of $3.025 \pm 0.025\,\mathrm{GeV}$, $3.075 \pm 0.025\,\mathrm{GeV}$, $3.125 \pm 0.025\,\mathrm{GeV}$ and $3.525 \pm 0.025\,\mathrm{GeV}$. The flux distribution is shown in figure 6.1.
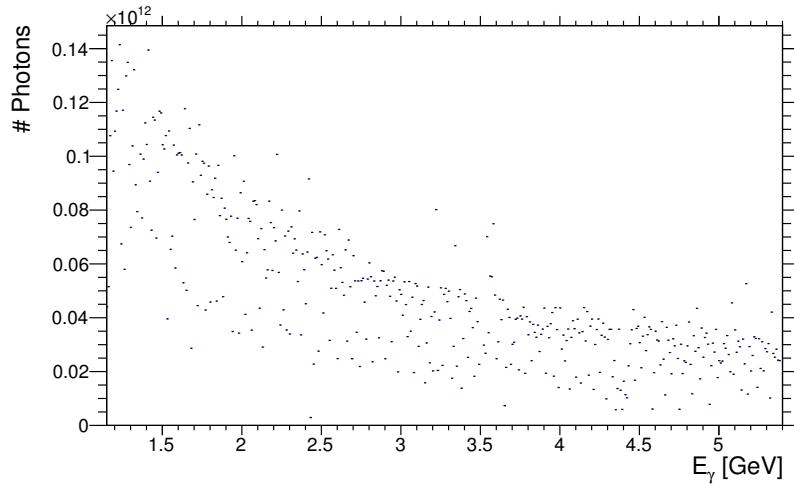
Figure 6.1: *g12* flux in $10\,\mathrm{MeV}$ bins.

6.1.2 Target Density

As described in section 2.3 the target for the *g12* run was a $40\,\mathrm{cm}\pm0.2\,\mathrm{cm}$ in length and $4\,\mathrm{cm}$ in diameter tapered cylinder filled with liquid hydrogen. The density of liquid hydrogen is dependent on temperature and pressure inside the target volume. Fluctuations for example in temperature would lead to fluctuations in the density which would influence the reaction rate. Therefore, values of pressure and temperature were recorded (shown in figure 6.2) and the average density calculated for each run separately.

The procedure for calculating the density of the target has been established in [33]. The formula is

$$\rho = -2.89 \cdot 10^{-5} \left[\frac{g}{cm^3 K^2} \right] T^2 + 1.0 \cdot 10^{-7} \left[\frac{g}{cm^3 mbar} \right] P + 8.249 \cdot 10^{-2} \left[\frac{g}{cm^3} \right],$$

where T and P represent the temperature and pressure and the coefficients are taken from [34]. An average density and its variance were calculated for each run and then an average density for all *g12* runs was determined. The total target density and it's variance was determined to

$$\begin{aligned} \overline{\rho}_{tot} \quad &= \frac{1}{N_{run}} \sum_i^{N_{run}} = \overline{\rho}_{run} = 0.07114 \pm 1.74 \cdot 10^{-5} \left[\frac{g}{cm^3} \right] \\ \sigma_{tot}^2 \quad &= \frac{1}{N_{run}-1} \sum_i^{N_{run}} (\overline{\rho}_{run} - \overline{\rho}_{tot})^2 = 0.00024. \left[\frac{g}{cm^3} \right] \end{aligned}$$

The uncertainty of the target density is much lower than the uncertainty of the physical dimensions of the target, and therefore do not have to be considered for the total systematic errors.
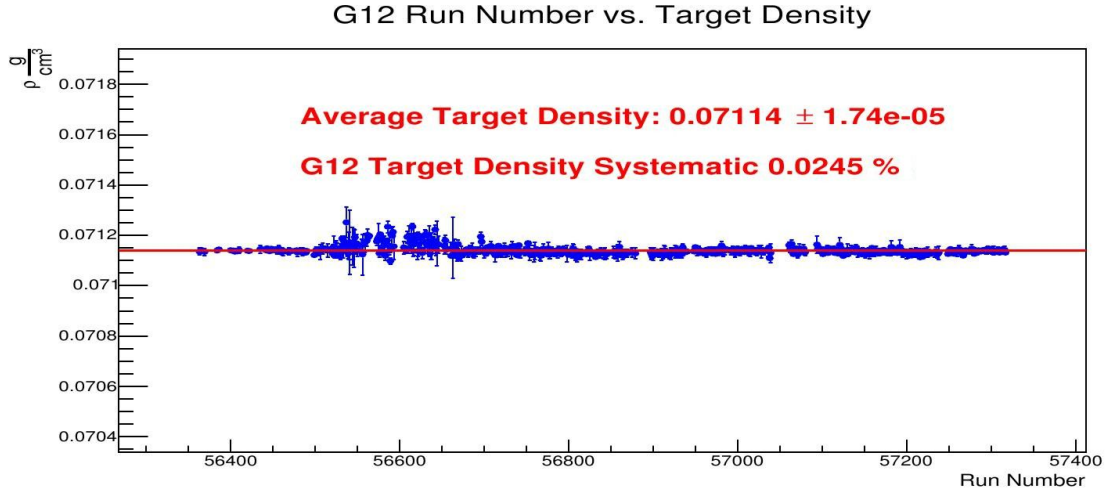
Figure 6.2: Target density for *g12*. [35]

6.1.3 Acceptance Calculation

In a first step Monte Carlo events have been generated, which consist of the four-vectors of the resonances participating in the reaction. These four-vectors are then further processed through a full simulation of the CLAS detector including detector inefficiencies and gaps in the acceptance. In the last step the Monte Carlo data is treated the same way as the raw data have been and is analyzed with the same software.

In this acceptance the detector inefficiencies are included as well as the signal loss from the cuts applied to the data sample. It is assumed that the acceptance is mostly affected by the energy and the production angle

$$A_{CLAS}(W, cos\theta_{CM}) = \frac{N_{acc}}{N_{MC}},$$

where N_{acc} is the number of reconstructed and accepted Monte Carlo events and N_{MC} is the number of generated events per certain energy and production angle.

6.1.4 Yield Extraction

For the determination of a differential cross section it is crucial to extract the number of events of the desired particle as precise as possible. Therefore, the following sections explain how the yield is extracted for the enhancement at a mass of $1.28\,\text{GeV/c}^2$ in combination with the enhancement at a mass of $1.4\,\text{GeV/c}^2$ visible in the $\pi^+\pi^-\eta$ mass spectrum.

Yield of $X(1280)$ and $X(1400)$

The extraction of the yield of the $X(1280)$ and $X(1400)$ is challenging. In figure 6.3 it is visible that the weighted $\pi^+\pi^-\eta$ mass spectrum has still much background left at higher masses.

Two major enhancements are visible in the $\pi^+\pi^-\eta$ mass shape at masses higher than $1\,\text{GeV/c}^2$, the first at a mass of $\approx 1280\,\text{MeV/c}^2$, referred to as $X(1280)$, and the second peak at a mass of $\approx 1400\,\text{MeV/c}^2$, referred to as $X(1400)$. For the first enhancement two explanations are possible. First, this heightening might be caused by the $f_1(1285)$ decaying to $\pi^+\pi^-\eta$ and the second includes the existence of the $\eta(1295)$ which also decays to $\pi^+\pi^-\eta$. The second structure might be identified by an excited η state, the $\eta(1405)$.

To calculate a differential cross section for the two enhancements at higher masses it is necessary to know the exact yield of both. The yield is extracted by fitting the signals as well as the non-resonant $\pi^+\pi^-\eta$ contribution.
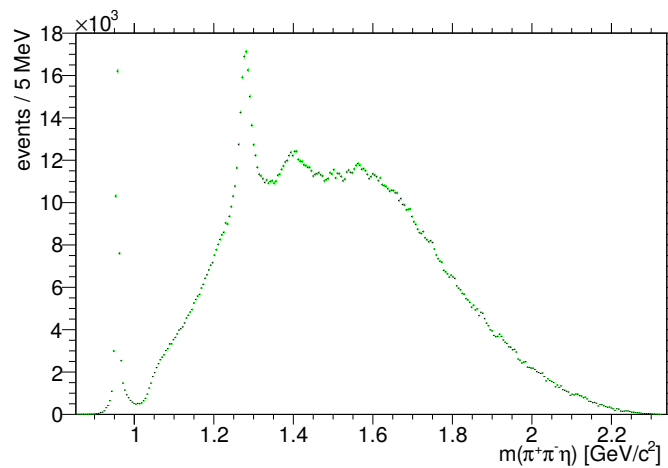
Figure 6.3: Invariant mass of $\pi^+\pi^-\eta$ weighted with Q.

The signal is fitted with a Voigt function which is a convolution of a Breit-Wigner ($L(x;\Gamma)$) function and a Gaussian ($G(x;\sigma)$) function.

$$V(m;\sigma\Gamma) = \int_{-\infty}^{\infty} G(m';\sigma)L(m-m';\Gamma)dm' \tag{6.1.1}$$

$$G(m;\sigma) = \frac{e^{-m^2/(2\sigma^2)}}{\sigma\sqrt{2\pi}} \tag{6.1.2}$$

$$L(m;\Gamma) = \frac{\Gamma}{\pi(m^2+\Gamma^2)} \tag{6.1.3}$$

Where m is the mass of the particle, Γ is the natural width of the particle and the σ of the Gaussian distribution is the detector resolution.

The data resolution is obtained from Monte Carlo simulations. For each of the assumptions of possible particles Monte Carlo events are generated with the width and mass given in the PDG. For all the reconstructed Monte Carlo events the difference between the mass of the corresponding raw Monte Carlo event and the mass of its reconstructed event is calculated. These events are further binned in bins of the center of mass energy using the same intervals as are used for the extraction of the events yields in section 6.1.5. The resolution is determined in dependence of the energy as it might change with increasing beam energy as well as the mass of the produced resonance.

Figure 6.4 shows the resolution for the $f_1(1285)$, $\eta(1295)$ and $\eta(1405)$ at three different energies. The energies are chosen to be at the threshold were the production of the particle starts, an energy in the middle and one at the highest possible energy.

The black dots represent the data, the blue line shows the fit. The binned data are fitted with a Crystal-Ball function whose width is then taken as sigma for the Gaussian part of the Voigt function. The distribution could not be described by a Gaussian or Voigtian function. Therefore, the Crystal-Ball function was chosen, which has the advantage of an asymmetric shape. The asymmetric shape is caused by the power low-end tail, which is assumed to be negligible as its contribution is small in contrast to the Gaussian core. The minimal resolution was found to be $4.12\,\text{MeV/c}^2 \pm 0.12\,\text{MeV/c}^2$ and the maximal $4.67\,\text{MeV/c}^2 \pm 0.44\,\text{MeV/c}^2$, which is equivalent within the errors. The averaged resolution is $4.3\,\text{MeV/c}^2$ for each particle and energy. Despite this constant behavior the resolution was determined for each energy bin of the cross section and used in the yield extraction as a fit parameter on a bin by bin basis.

The method used to describe the data and extract the yield of the enhancements is described in the following subsections along with different model selection criteria.

6.1.5 Strategy of the Yield Extraction

For a proper estimation of the yield of the two enhancements visible in figure 3.14 one has to choose the hypothesis with the best fit quality for the description of the data. The mass shapes of the two individual resonances will be described by a Voigtian profile. This function includes the mass and natural width of the assumed resonance as well as the detector resolution. The mass of the fit hypothesis can be chosen from the PDG as fixed parameter or be released in the fit procedure.
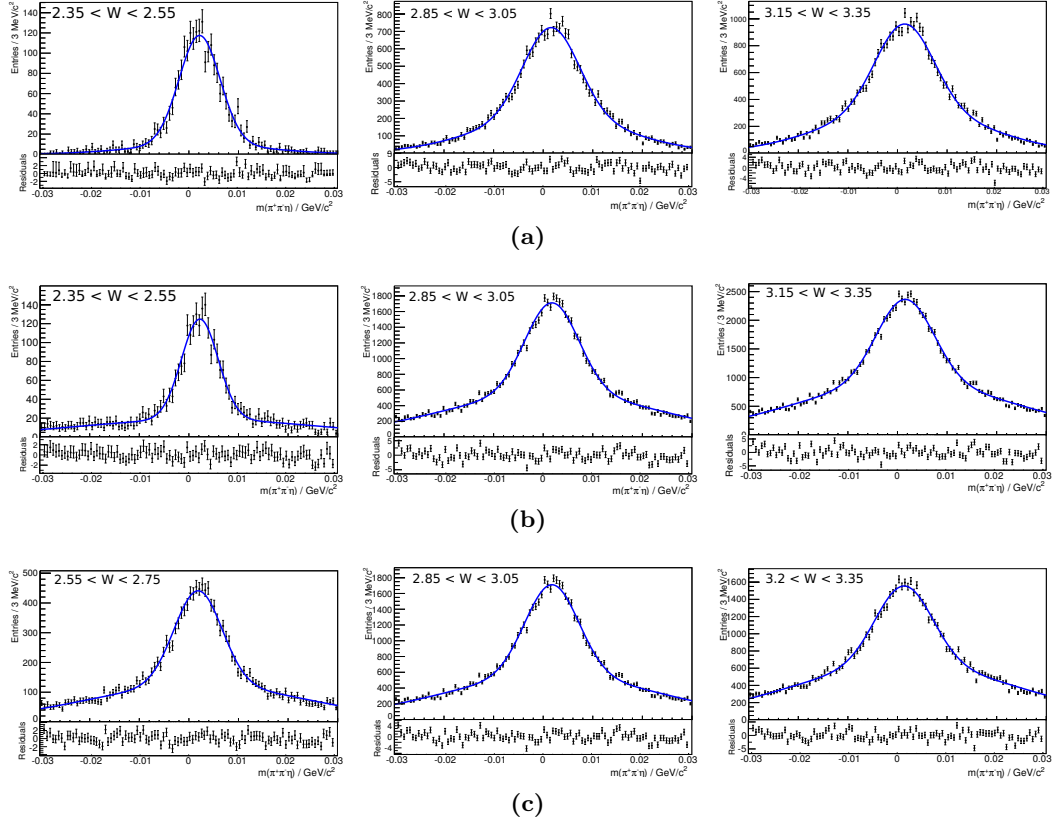
Figure 6.4: Resolution from Monte Carlo simulation for $f_1(1285)$, $\eta(1295)$ and $\eta(1405)$. (a) $f_1(1285)$, (b) $\eta(1295)$ and (c) $\eta(1405)$. The middle of the corresponding center-of-mass energy range is shown in the upper left corner of each plot. The box below the mass distribution shows the residuals between the fit and the data points in terms of σ.

The first raise can be explained by either the $f_1(1285)$ or the $\eta(1295)$, while the second enhancement can be originated by with the $\eta(1405)$. The following table summarizes the mass and width listed in the PDG for the relevant resonances.

particle	m_{PDG} [MeV]	Γ_{PDG} [MeV]
$f_1(1285)$	1281.9±0.5	24.2±1.1
$\eta(1295)$	1294±4	55±5
$\eta(1405)$	1406.2±2.3	54±4

Table 6.1: Resonance parameters of $f_1(1285)$, $\eta(1295)$ and $\eta(1405)$ taken from PDG [3].

The non-resonant part in the mass spectrum can not only be described by a pure phase space distribution and thus a second order polynomial or a third order polynomial is added to the fit function.

Another complication is the strong dependence of the yield on the beam energy and the production angle of the meson. To take this behavior into account a proper parametriza-

tion depending on these properties would be needed. Due to the fact that this can be achieved only by employing a full partial wave analysis the whole data set has been binned. The data have been divided in sub-samples by applying a 2-dimensional binning in energy and the meson production angle. For each of the ranges a fit has been conducted, which yields the possibility to extract a yield in dependence of the cosine of the meson production angle as well as the center-of-mass energy. Hence it is feasible to show a differential cross section.

Two different values have been chosen for the bin width of the energy binning. The first has a bin width of 200 MeV. Due to the fact that the $X(1280)$ has enough statistic per sub-range the energy bins can be divided further by half. The binning in the production angle is chosen to a bin width of 0.2 of the $cos(\theta)$ value over the whole range.

For every sub-range of the data both resonances have been fitted except the ones near their production threshold. The fit range in the $\pi^+\pi^-\eta$ mass expanded from $1.1 \, \text{MeV}/c^2$ to $1.5 \, \text{MeV}/c^2$.

In a first step it will be tested which resonances may contribute to the reaction (section 6.1.9), these hypotheses include either the $f_1(1285)$ or the $\eta(1295)$ together with the possible production of the $\eta(1405)$. In this step all masses and widths of the particles are fixed to the PDG values.

Once the best fit hypothesis has been chosen it will be systematically tested if several fit parameters of the chosen hypothesis can be released within limited borders or if they have to be left fixed to guarantee a good fit result (section 6.1.10). For all fit hypotheses the resulting invariant $\pi^+\pi^-\eta$ mass spectrum, integrated over all energies and angles, is shown.

6.1.6 Maximum Likelihood Method

In order to determine the values of the free fit parameters of the fit mode the maximum likelihood method was used. Every event has its own well defined position in phase space. Generally, if the probability is p to find a certain event at a certain point in phase space x_i then the probability P for an ensemble of events is the product of the single probabilities multiplied with $n!$. n is the number of events, with the assumption that the events are independent of each other and of the order of events. The probability for a certain point x_i in space is proportional to the intensity distribution $|f(x_i; \vec{\phi})|^2$, where f is the probability density function. In order to describe the data with $f(x; \vec{\phi})$ a likelihood function is defined in the following way

$$\mathcal{L} = n! \prod_{i=1}^{n} \frac{|f(x_i; \vec{\phi})|^2 \epsilon(x_i)}{\int |f(x_i; \vec{\phi})|^2 \epsilon(x) dx}. \tag{6.1.4}$$

The detector acceptance as well as the reconstruction efficiency is considered by the term $\epsilon(x_i)$ and the parameters needed to describe the weighting function is $\vec{\phi}$. The integral in the denominator includes the integration over the whole phase space and is needed for normalization. The integral can not be determined analytically, but it can be described by the sum of weights of n Monte Carlo events. As the Monte Carlo events are subject to

the same acceptance and reconstruction inefficiencies as the data events, the acceptance correction $\epsilon(x_i)$ is considered implicitly and the integral becomes,

$$\frac{n_{data}}{n_{MC}} \sum_{j=1}^{n_{MC}} |f_{MC}(x_j; \vec{\phi})|^2, \tag{6.1.5}$$

where each Monte Carlo event gets the weight 1. The product of many probabilities is a small number and causes instabilities in numerical calculations. Therefore, the *negative log likelihood* is defined

$$NLL = -ln\mathcal{L} = -\sum_{i=1}^{n_{data}} ln|f_{(data}(x_i; \vec{\phi})|^2 + n_{data}ln \sum_{j=1}^{n_{MC}} |f_{MC}(x_j; \vec{\phi})|^2 \tag{6.1.6}$$

and its minimum sought. Formula 6.1.6 is the likelihood neglecting the constant terms, because they do not affect the minimum. In order to extract the released fit parameters optimal the final formula minimized is

$$f = \frac{n_{data}}{2} \left(\frac{\sum_{j=1}^{n_{MC}} |f_{MC}(x_j; \vec{\phi})|^2}{n_{MC}} - 1 \right)^2 - \sum_{i=1}^{n_{data}} ln|f_{(data}(x_i; \vec{\phi})|^2 + n_{data}ln \sum_{j=1}^{n_{MC}} |f_{MC}(x_j; \vec{\phi})|^2 \tag{6.1.7}$$

In the case of convergence the first addend vanishes, because then the number of Monte Carlo events is exactly as large as the integral over the phase space of the phase space distributed Monte Carlo events.

The adjustment of the degrees of freedom is achieved by using MINUIT2 [36], which uses deterministic algorithms.

For this analysis a 1-dimensional fit has been conducted, to describe the invariant $\pi^+\pi^-\eta$ mass.

$$f(x_i; \vec{\phi}) = f(m_{\pi^+\pi^-\eta}; \vec{\phi}) \tag{6.1.8}$$

Other phase space parameters, except the meson production angle and the beam energy (taken into account by binning), have not been considered and thus the fit is not sensitive to these.

6.1.7 Model Selection Criteria

The yield extraction is prone to systematic effects caused by the model fitted to the mass shape. In order to extract the yield as precise as possible the $\pi^+\pi^-\eta$ mass shape has been fitted with different models to describe the data under different hypotheses. In this case the model is the actual function and the hypothesis the assumption of what particles contribute. At this point one needs a measure to assess which fit has the highest significance.

The most used and widely known parameter to measure the model quality is to have a look on the χ^2 in relation to the number of degrees of freedom (*reduced* χ^2). The χ^2 is calculated the following way

$$\chi^2 = \sum_{i=0}^{n_{bins}} \frac{(y_{i,data} - y_{i,fit})^2}{\sigma_{i,data}^2 + \sigma_{i,fit}^2} , \tag{6.1.9}$$

for binned observables. Basically the χ^2 value is just the squared sum over the difference of each bin content between the data and the obtained fit value normalized by the sum of the squared errors for each bin.

As mentioned in section 3.9.2 it is possible to propagate the errors of the Q-factors to the distributions under consideration of the correlation between the events (equation (3.9.10)). It has also been mentioned that a huge extent of time and computing power is needed to calculate the correlation per bin. Hence, a 100% correlation is assumed. In addition to the statistical error of each bin the sum of the errors of the Q-factors is taken into account (equation (3.9.12)). This might lead to an overestimation of the errors per bin. If one calculates the χ^2/NDF one gets values which are systematically too low.

Another well known test is the likelihood ratio test. The likelihood ratio test can be used only for the comparison of nested hypotheses. This means that only less complex models can be tested against the full model if the less complex models are a subset of the full model. Thus a test for the fit quality is needed which does not dependent on the errors of the events or does not need nested hypotheses. Two of these tests will be described in the following text.

Akaike Information Criterion

The Akaike information criterion (AIC) offers a solution to choose between different models. It estimates the quality of each model relative to other models. In doing so it does not provide a measure on how good a fit is. If all models fit poorly you are only able to choose the one better than the others, which means you are not able to conduct a test of a null hypotheses. But it provides a good measure using the trade-off between the quality of the model and the complexity of the model.

The basic AIC value is calculated like this

$$AIC = 2k - 2ln\mathcal{L} = 2k + 2NLL, \qquad (6.1.10)$$

where k is number of estimated parameters, $\mathcal{L}$ the Likelihood and NLL the negative logarithmic likelihood respectively. Hence the model with the smallest AIC value is stated to be the best fitting model. AIC discourages over-fitting, because it includes a penalty for an increasing number of fit parameters.

Additional to this the criterion should take the sample size into account. AIC is assumed to be used for infinite sample sizes. In this case our event number is not infinite. Therefore, the $AICc$ value is used for testing these models. $AICc$ is useful for finite data samples and is defined as

$$AICc = AIC + \frac{2k(k+1)}{n-k-1}. \qquad (6.1.11)$$

In this equation k and n denote the number of fit parameters and the number of events to be fitted. If n gets large $AICc$ becomes AIC, but $AICc$ has the advantage of a greater penalty for a greater number of fit parameters.

Bayesian Information Criterion

The Bayesian information criterion (BIC) or Schwarz criterion was developed as a measure to choose between a finite set of models. Analogous to AIC the model with the

most negative BIC value is the most preferable. As AIC, BIC includes a penalty on the number of fit parameters, as the raise of fit parameters increases the likelihood, but may result in over-fitting.

BIC is defined as

$$BIC = -2ln\mathcal{L} + k \cdot ln(n) = 2NLL + k \cdot ln(n) \qquad (6.1.12)$$

In contrast to $AICc$ this method has two disadvantages. The first is that it can be used only if the sample size is much larger than the number of fit parameters. The second is that it can not handle complex collections of models.

6.1.8 Order of Polynomial for Background Description

For the decision what polynomial is suited better to describe the background two scenarios have been executed. Both scenarios use the values listed in the PDG for the $f_1(1285)$ and $\eta(1405)$ as fixed parameters for the two Voigtian functions. Additionally the first fit uses a second order polynomial while the latter one uses a third degree polynomial. Polynomials of higher orders are problematic as the probability increases that not only the background is described by the polynomial, but the enhancements, too. As mentioned before the χ^2 is not suitable to choose the best fit method in this case due to too large errors.

Consequently the $AICc$ values have been calculated for each bin and for both fits. In the next step the difference between the $AICc$ values for the fit using the second order polynomial and the $AICc$ values for the fit using a third order polynomial has been calculated. The two dimensional histogram (figure 6.5) shows this difference on the z-axis, while x-axis depicts the energy bins and the cosine bin is displayed on the y-axis. Once more one has to emphasize that these tools do offer a relative comparison between the quality of several fits, but do not deliver an estimation if the model is suited to describe the data well. Even so the likelihood decreases more with increasing fit parameters the
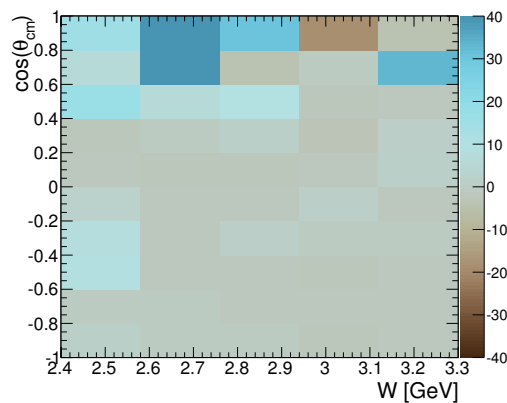
Figure 6.5: Difference of $AICc$ values for second order polynomial minus third order polynomial, while all fit parameters fixed except the yield.

information criteria punish an increasing number of fit parameters and BIC does this more than $AICc$.

Since the $AICc$ value of the second order polynomial is taken minus the $AICc$ value of the third order polynomial per fit, the second order polynomial is favored if the difference values tend to be negative and the third order polynomial is favored if the difference values are positive.

It is visible that the third order polynomial delivers a better fit quality than the lower order polynomial in most of the bins. It is mostly preferred in bins with high statistics, which means the combination of a lower center of mass energy as well as a high positive $cos(\theta)$ value. In some bins the second order polynomial is favored, but the difference between the two $AICc$ values is not as high as for the bins where the third order polynomial is favored.

Due to the fact that most bins which show a significant deviation in $AICc$ values fit better with the third order polynomial all following results that are shown are fitted with a with this polynomial for background estimation.

6.1.9 Contributing Resonances

A systematic check has been performed to test which resonances possibly contribute to the invariant $\pi^+\pi^-\eta$ mass spectrum in the region from $1.1\,\text{GeV/c}^2$ to $1.5\,\text{GeV/c}^2$. For this purpose all fit parameters of the Voigtians are fixed except the yields. As mentioned before three possible scenarios have been tested:

- Hypothesis 1: $\eta(1295)$ and $\eta(1405)$, all fit parameters fixed except yields

- Hypothesis 2: $f_1(1285)$ and $\eta(1405)$, all fit parameters fixed except yields

- Hypothesis 3: $f_1(1285)$, all fit parameters fixed except yields, but no $\eta(1405)$

The first hypothesis includes the production of the $\eta(1295)$ and exposes in the $\pi^+\pi^-\eta$ spectrum as the enhancement at $1.28\,\text{GeV/c}^2$. This hypothesis also includes the $\eta(1405)$ which would then explain the second enhancement.

The second hypothesis assumes that the $f_1(1285)$ is responsible for the first enhancement and includes the production of the $\eta(1405)$ as well.

Figure 6.6 shows a comparison of the invariant $\pi^+\pi^-\eta$ mass spectrum between the selected data and the fit, corresponding to hypothesis 1. The black points depict the data, while the green, magenta and blue line show the whole fit, the contribution of $f_1(1285)$ and $\eta(1405)$ respectively. The histogram is the sum of all single fits in each bin. Beneath the mass spectrum the residuals are shown. The horizontal red and green line depict the values for zero and plus/minus three σ.

The $\eta(1295)$ has a mass of about $1294\,\text{MeV/c}^2$ and a width that has a value of $55\,\text{MeV/c}^2$, which makes it much broader than the $f_1(1285)$.

The fit as well as the residuals show a huge systematic deviation in the mass region from $1.25\,\text{GeV/c}^2$ to $1.35\,\text{GeV/c}^2$. This deviation is an indication for a systematic shift of the obtained mass compared to the reported PDG value. Additional to this the natural width of the $\eta(1295)$ is too broad to be agreeable with the width of the first enhancement. This is also visible in the residuals as the values leave the 3σ band in the region of the first enhancement, while staying within for the rest of the range.
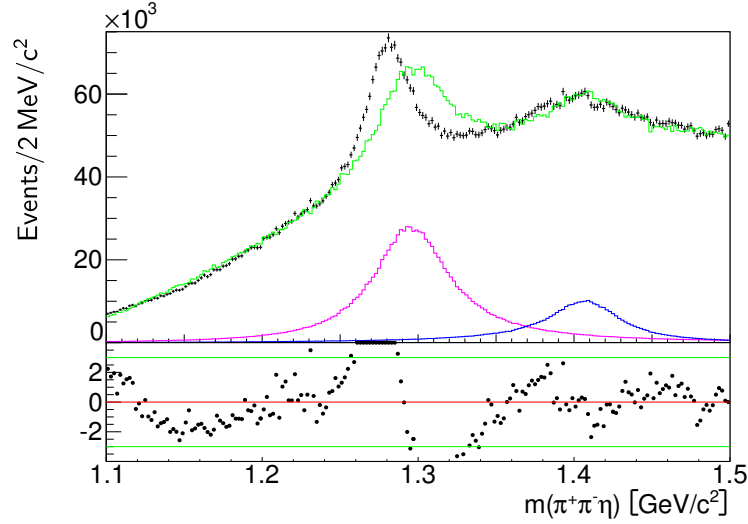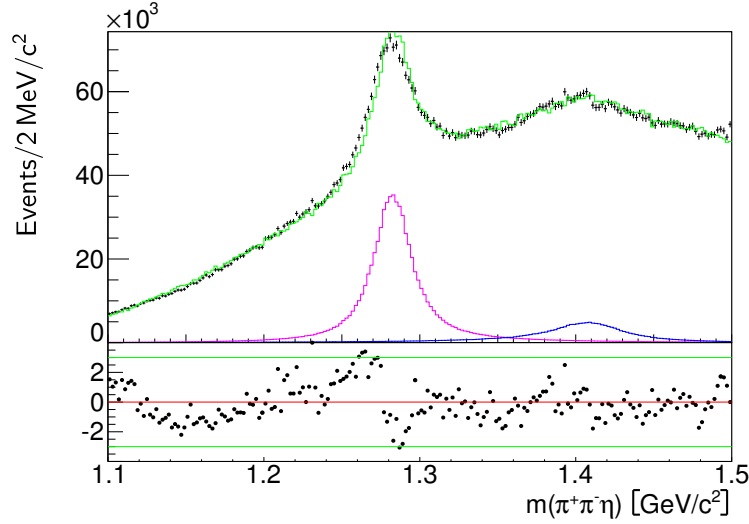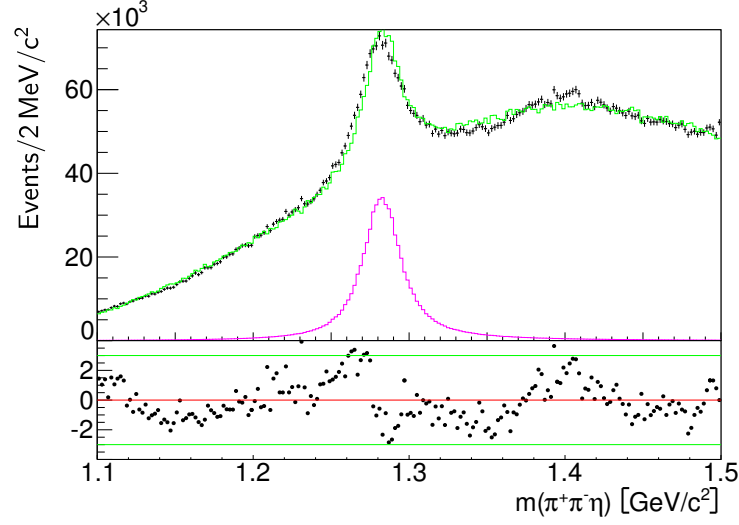
Figure 6.6: Hypothesis 1. Integrated over all energy ranges and production angles. The black points show the data. The weighted events obtained from the fit are illustrated with a green line, the magenta line depict the contribution of the $\eta(1295)$ while the blue line indicates the $\eta(1405)$ contribution.

As a preliminary result one might say that the assumption that the data are containing an $\eta(1295)$ based on the properties listed in the PDG is not confirmed.

The comparison between the mass shape of the selected data and of the fit corresponding to hypothesis 3 is illustrated in Figure 6.7.

The region of the second enhancement is described reasonable well by the fit.

Additional to this the residuals show a small systematic behavior in the region from 1.1–1.2 GeV/c^2, where the residuals lie systematically below zero. This might be due to the fact that a third degree polynomial does not satisfy a perfect data description, but describes it well enough so that the residuals lie well within 2σ. The only systematic deviation is visible in the range around the X(1280), which is fitted under the hypothesis being the $f_1(1285)$. While all points of the residuals are above zero from 1260 MeV/c^2 to 1280 MeV/c^2 they fall below zero from 1280 MeV/c^2 to 1300 MeV/c^2. This is an indication that the obtained mass for the X(1280) is systematically shifted by approximately 2 MeV/c^2 with respect to the PDG value for the mass of the $f_1(1285)$.

This is also visible in the invariant mass spectrum where the green line is shifted to the right of the mean of the data distribution. The mean of the fit coincides with the mean of the first enhancement, with a slight deviation to a higher mass. All parameters of the Voigtian describing the $f_1(1285)$ are fixed except the yield. The data shows the mean at a mass approximately 2 MeV/c^2 beneath the PDG value. It has to be added that the PDG mass is only an average over many measurements.

The width of the Voigtian is a combined width from the detector resolution, which is accounted for in the σ of the Gaussian part, and the natural width of the particle, which is accounted for in the Γ in the Breit-Wigner part. Even with fixed parameters the width

Figure 6.7: Hypothesis 2. Integrated over all energy ranges and production angles. The black points show the data. The weighted events obtained from the fit are illustrated with a green line, the magenta line depicts the contribution of the $f_1(1285)$ and the blue line indicates the contribution of the $\eta(1405)$.

of the peak in the data seems to be matched well by the width of the $f_1(1285)$ taken from PDG.

Therefore, we can state that the $f_1(1285)$ contributes to the mass shape with a higher possibility than the $\eta(1295)$ does.

In a last step the data distribution has been fitted under the assumption that the $\eta(1405)$ is not produced (hypothesis 3), and therefore has not to be taken into account to describe the mass shape in a proper way. Accordingly, the data have been fitted only with a Voigtian shaped by the $f_1(1285)$ parameters and a polynomial function, cf. figure 6.8.

The following dip between the two enhancements is overestimated this time which is also present in the residuals. This might indicate that the enhancement is not only caused by fluctuations, but a resonance is needed to describe this and the dip between the two enhancements is described better by considering the second resonance at $1400\,\mathrm{MeV/c^2}$.

The mean of the second peak is approximately $1400\,\mathrm{MeV/c^2}$ which corresponds to the assumption of it being an $\eta(1405)$. Since the excited η states are relatively broad compared to the $f_1(1285)$ and η', this might explain why it is not as prominent as the aforementioned states. To get a further confirmation if the $\eta(1405)$ has to be taken into account one can compare the *AICc* and *BIC* values of both fits.

Figure 6.9 shows the difference of the *AICc/BIC* values for the fit with the assumption of an $\eta(1405)$ taken into account to describe the data distribution and the fit with no $\eta(1405)$ included. The difference is calculated using the obtained *AICc* and *BIC* values for both fits. The difference of the *BIC* values is displayed too, because *BIC* features a higher penalty for an increase in the number of fit parameters.

It is evident that most of the bins have a gray color which indicates that for these kinematic regions it does not matter whether the $\eta(1405)$ is included or not. Several bins

Figure 6.8: Hypothesis 3. Integrated over all energy ranges and production angles. The black points show the data. The weighted events obtained from the fit are illustrated with a green line, the magenta line depicts the contribution of the $f_1(1285)$.

are colored brown, which is an evidence that the $\eta(1405)$ has to be considered with respect to the calculated $AICc$ and BIC values. A vertical line of brown colored bins shows at a center-of-mass energy of 2.5 GeV. This energy bin covers the production threshold of the $\eta(1405)$ and an enhanced production is expected at energies near and above the production threshold.

(a) *AICc*

(b) *BIC*
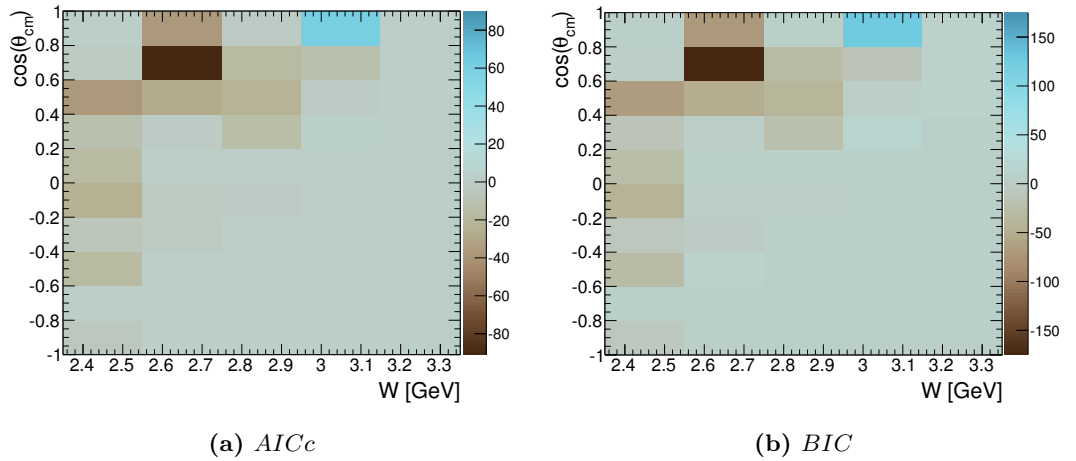
Figure 6.9: Difference of *AICc* and *BIC* values for fit with fixed parameters and assumption of $f_1(1285)$ and $\eta(1405)$ and fit with fixed parameters and assumption of $f_1(1285)$, but without $\eta(1405)$.

A horizontal strip of brown colored bins appears for the cosine of the meson production angle of 0.7. This strip indicates a clear preference to include the $\eta(1405)$ into the description of the data. This circumstance has to be emphasized as those bins are bins with a high event statistic. In contrast to this the fit where only the $f_1(1285)$ is taken into account is favored for the most forward angular bins. This behavior can be explained by taking the geometry of CLAS into account, as the statistic is significantly decreased due to the forward hole of CLAS. Therefore, a fit with less fit parameters is preferred in comparison to the fit including the $\eta(1405)$.

Nevertheless, the outcome shows that the $\eta(1405)$ has clearly to be considered.

As temporarily conclusion one might say that the $\eta(1405)$ is needed in the energy region near its production threshold as well as in the forward direction where a high event statistic is present. This has to be rechecked with a fit where the mass and resolution of the $f_1(1285)$ are released.

6.1.10 Systematic Checks for Yield Extraction

For a proper extraction of the yield of the two visible resonances it is crucial to describe the mass shape as perfect as possible. It has been become apparent that the mass of the first enhancement is slightly systematic lower than the reported PDG value for the $f_1(1285)$. In order to make allowances for this systematic shift it might be feasible to release certain parameters of the fit.

The first parameter in consideration is the mean of the Voigtian, to allow the fit to adjust to the mean of the first increase. Additional to this the fit parameter representing the detector resolution is released.

At first a check has to be made if the $\eta(1405)$ has still to be taken into account if
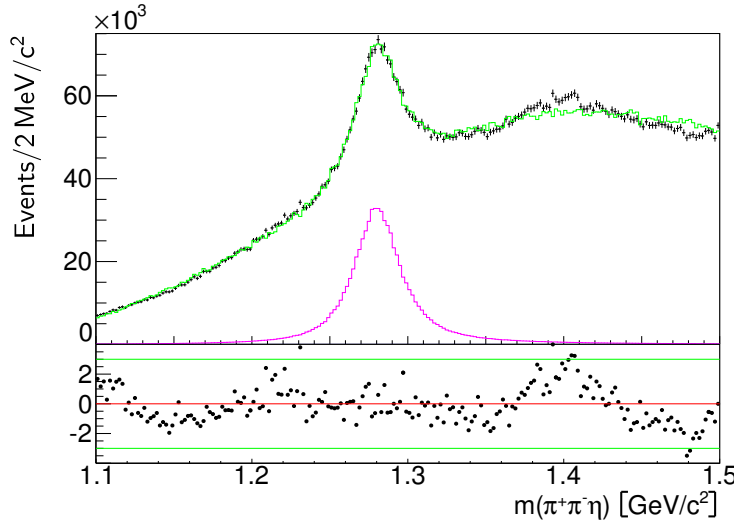
Figure 6.10: Integrated over all energy ranges and production angles, fit parameters fixed except yields, mass and resolution of $f_1(1285)$. The black points show the data. The weighted events obtained from the fit are illustrated with a green line, the magenta line depicts the contribution of the $f_1(1285)$.
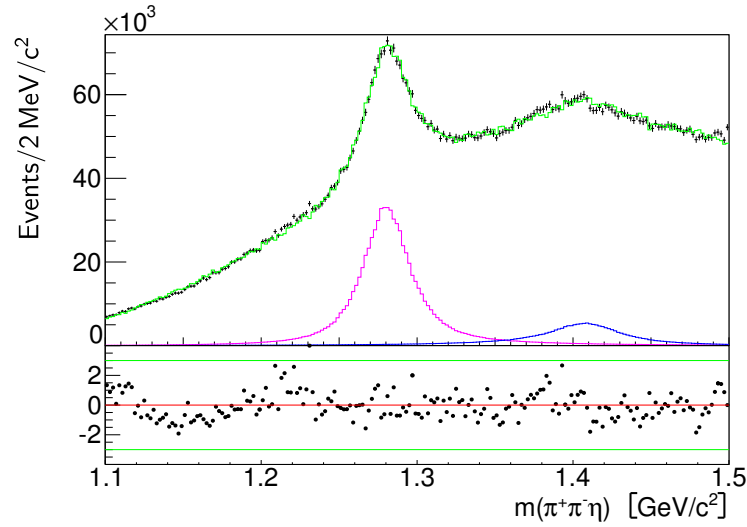
Figure 6.11: Integrated over all energy ranges and production angles, fit parameters fixed except yields, mass and resolution of $f_1(1285)$. The black points show the data. The weighted events obtained from the fit are illustrated with a green line, the magenta line depicts the contribution of the $f_1(1285)$ while the blue line indicates the $\eta(1405)$ contribution.

parameters of the Voigtian describing the $X(1280)$ resonance are allowed to vary within the limits. This can lead to a broadened distribution which might enable the fit to describe the distribution properly without any $\eta(1405)$ contribution.

Figure 6.10 shows a fit result with the released parameters for the $X(1280)$. The first enhancement of the mass distribution is described well. The width and mean of the peak are matched almost perfectly with the ones of the $f_1(1285)$, but the description of the data above $1.3\,\mathrm{GeV/c^2}$ is very poor.

In order to improve the description of the mass shape further the production of the $\eta(1405)$ is added to the scenario, while the parameters of the Voigtian describing this resonance are still fixed to PDG values. The small contribution of this resonance to the whole spectrum and the subdivision in energy and angular bins does not allow a release of these parameters.

Figure 6.11 shows a comparison of the invariant $\pi^+\pi^-\eta$ mass spectrum for the selected data and the fit which considers the $f_1(1285)$ as well as the $\eta(1405)$.

It is apparent that the peak position is matched much better than for the corresponding fit with fixed parameters, as well as the width which matches perfectly, too . This is also evident in the residuals. The fluctuations of the residuals within the mass range from $1.24\,\mathrm{GeV/c^2}$ to $1.34\,\mathrm{GeV/c^2}$ are much smaller than in figure 6.7. In addition to this the points are evenly distributed around the red line, which means that no major systematic behavior is recognizable. In order to support the assumption that the distribution is described better by this fit one can compare the $AICc$ values of the fit from the fit with fixed parameters to the ones of this fit.

For further confirmation that both resonances are needed for a good description of the data one can have a look at the difference of $AICc$ values.
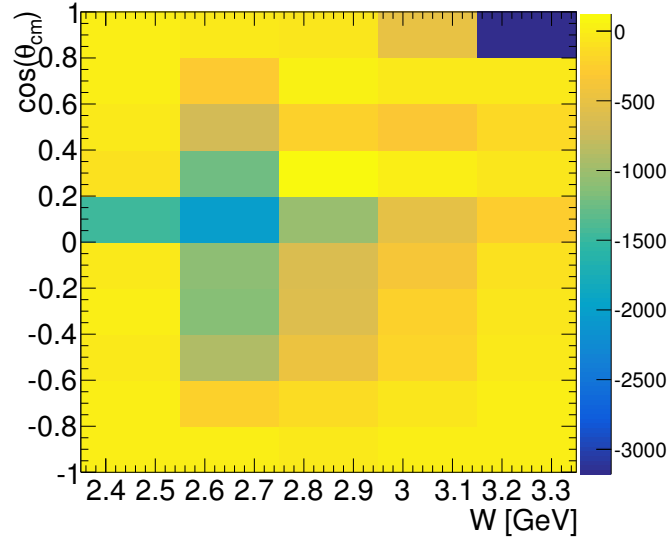
Figure 6.12: Difference of $AICc$ values from fit with mass and resolution of the $f_1(1285)$ are allowed to vary. One fit fits the $\eta(1405)$ too and the other only the $f_1(1285)$.

In figure 6.12 one can see the difference between the $AICc$ values obtained from the fits with and without the $\eta(1405)$. It is obvious that for most of the fits the $\eta(1405)$ has to be taken into account. This is very significant for the fits near the production threshold of the $\eta(1405)$. In comparison to figure 6.9 the significance is more pronounced. Almost all bins show a tendency to prefer the fit including the $\eta(1405)$.

At last it is necessary to verify if the fit with released parameters describes the mass shape better than the fit where the parameters of the Voigtian are fixed.

In figure 6.13 one can see the difference of $AICc$ values for the fit with released parameters and the fit with fixed parameters. It is remarkable that almost all bins exhibit negative values. This demonstrates that the fit with released parameters is preferred to the fit with the fixed parameters even if two more parameters are needed. This is visible for the energy range from $2.55\,\mathrm{GeV/c^2}$ to $2.95\,\mathrm{GeV/c^2}$ and an $cos(\theta)$ from -0.6 to 0.4, which is remarkable because this energy region corresponds to the production threshold of the $\eta(1405)$.

As a preliminary result one might state that the $\eta(1405)$ is needed to describe the data distribution in an acceptable way and that it is possible to extract a differential cross section for the $\eta(1405)$ in photoproduction which is showed in section 6.2.4. Therefore, all following results are extracted by fitting a polynomial of third order in addition with two Voigtians describing the mass region at $1.28\,\mathrm{GeV/c^2}$ with released parameters for the mass and width and the $X(1400)$ with fixed parameters.
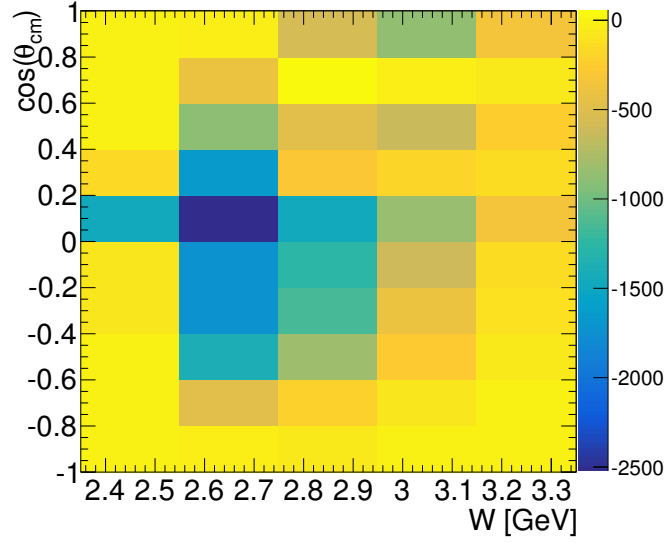
Figure 6.13: Difference of *AICc* values from fit with mass and resolution released to the
AICc values of the fit with all parameters fixed except the yields.

6.2 Results

In the preceding chapters a complex method was described to select a very background
free data sample to measure physical observables.

Due to the fact that the η is reconstructed via the missing mass method the data sample
contains lots of events which are not $p\pi^+\pi^-\eta$ signal events. This becomes clearly apparent
in the spectrum of the missing mass of $p\pi^+\pi^-$. Therefore, the multivariate side-band
subtraction method was applied with the η mass as reference coordinate in order to
reduce the background in the whole $\pi^+\pi^-\eta$ mass spectrum.

We will show the results for the mass and width of the $X(1280)$. Furthermore, the
obtained differential cross sections for the $X(1280)$ and $X(1400)$ will be presented.

6.2.1 Differential Cross Section for the Reaction $\gamma p \rightarrow pX(1280)$

This section will summarize the results for the contained differential cross section of the
reaction $\gamma p \rightarrow pX(1280)$. This has been realized by subdividing the data sample in ranges
of the center-of-mass energy as well as in 10 bins of the cosine of the meson production
angle in the center-of-mass frame of $pX(1280)$. The forward and backward holes of the
CLAS detector are limiting factors. The binning in the center-of-mass energy starts at
2.35 GeV and goes up to 3.35 GeV. Due to the relatively high production statistic of the
$X(1280)$ signal it was possible to chose the bin width for the following results to 100 MeV.
The yield was extracted in ranges of the beam energy and cosine of the production angle
and enables to show a differential cross section. In total 84985 ± 534 $X(1280)$ events have
been determined.
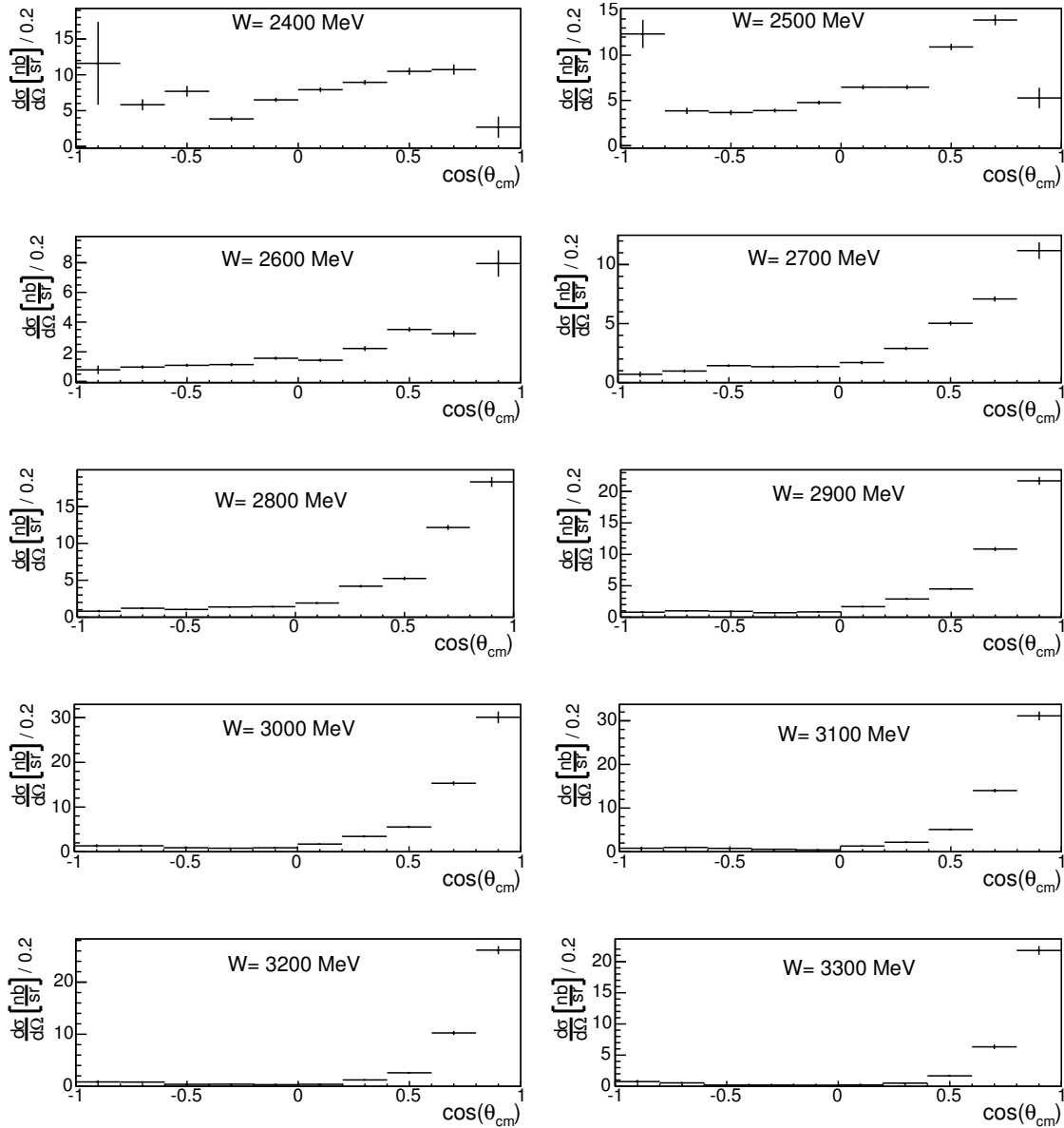
Figure 6.14: Differential cross section of the $\gamma p \to p X(1280) \to \pi^+\pi^-\eta$. The energy is divided in 100 MeV samples and the mean energy of each bin is shown in each plot.

As mentioned before the identity of the enhancement at the mass of $1280\,\mathrm{MeV/c^2}$ is not fully clarified. Therefore, the presented cross sections include also the unknown decay fraction of $X(1280) \to \pi^+\pi^-\eta$. The contribution of the branching fractions of the η decays is taken into account by simulating all four main contributing decays of the η according to their reported branching fractions.

Figure 6.14 shows the differential cross section for the reaction $\gamma p \to p X(1280)[\pi^+\pi^-\eta]$.
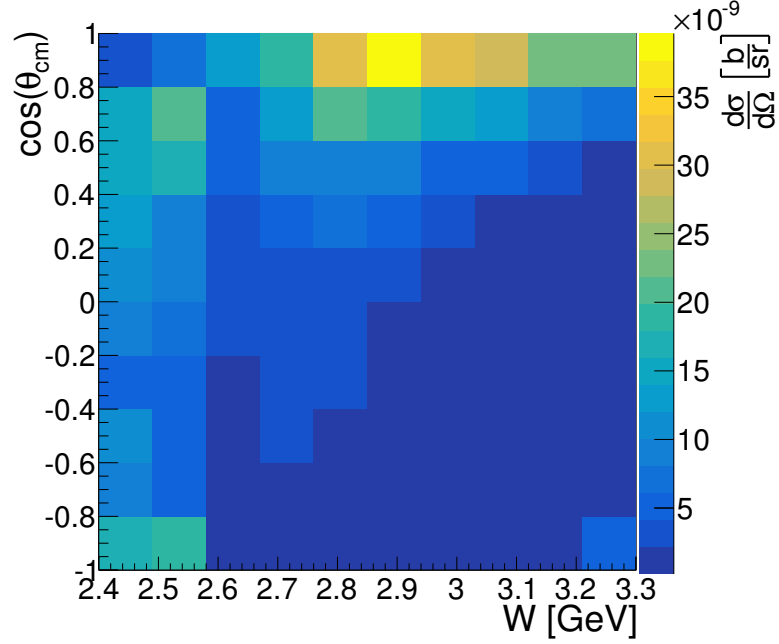
Figure 6.15: Differential cross section of the $X(1280) \rightarrow \pi^+\pi^-\eta$. The x and y-axis show the corresponding energy range and the cosine of the production angle respectively while the z-axis displays $d\sigma/d\Omega$.

It is to emphasize that the forward-most and backward-most angles have to be treated with caution, because of lacks in the acceptance of the CLAS detector.

The lowest energy range is close to the production threshold of the $f_1(1285)$ at 2.35 GeV. It is clearly visible that the cross section features a relatively flat distribution near the production threshold of the $f_1(1285)$.

At a center-of-mass energy of 2.5 GeV the cross section tends to develop a peak in forward direction. With rising center-of-mass energy the peak in forward direction becomes more and more prominent. This behavior is likely associated with t-channel production mechanism which can be described by recent Regge model calculations published by the CLAS collaboration [37]. The model predicts a rise in forward direction and suggests that part of the strength of the $f_1(1285)$ comes from s-channel baryon production. Additionally the model predicts a fall down in the forward-most bins of the cross section which might shows in the first two energy sub-ranges.

The amplitude of the cross section rises to a maximum value of 30 nb/sr. The drop in cross section at an energy of 2.6 GeV is due to non-working PMTs in the tagger and has no physics cause.

In figure 6.15 the same differential cross section for the reaction $\gamma p \rightarrow pX(1400)(\pi^+\pi^-\eta)$ is shown as a two-dimensional plot to achieve a better overview of the alteration of the cross section with energy and angle.

Obviously the highest cross section is around the production threshold and at angles corresponding to the forward direction.

Further discussion is given in chapter 8. A table of all values can be found in section 8.2.

6.2.2 $X(1280)$ Mass and Width

One aim of this analysis is to shed light on the origin of the enhancement at a mass of 1280 MeV/c^2. As it has been mentioned in section 1.5 it is rather difficult to make a statement if the $\eta(1295)$ exists or if it is just an artifact of the partial wave analyses made by other groups. Performing a partial wave analysis for the reaction $\gamma p \rightarrow p\pi^+\pi^-\eta$ is very challenging due to a large number of different contributing intermediate resonances
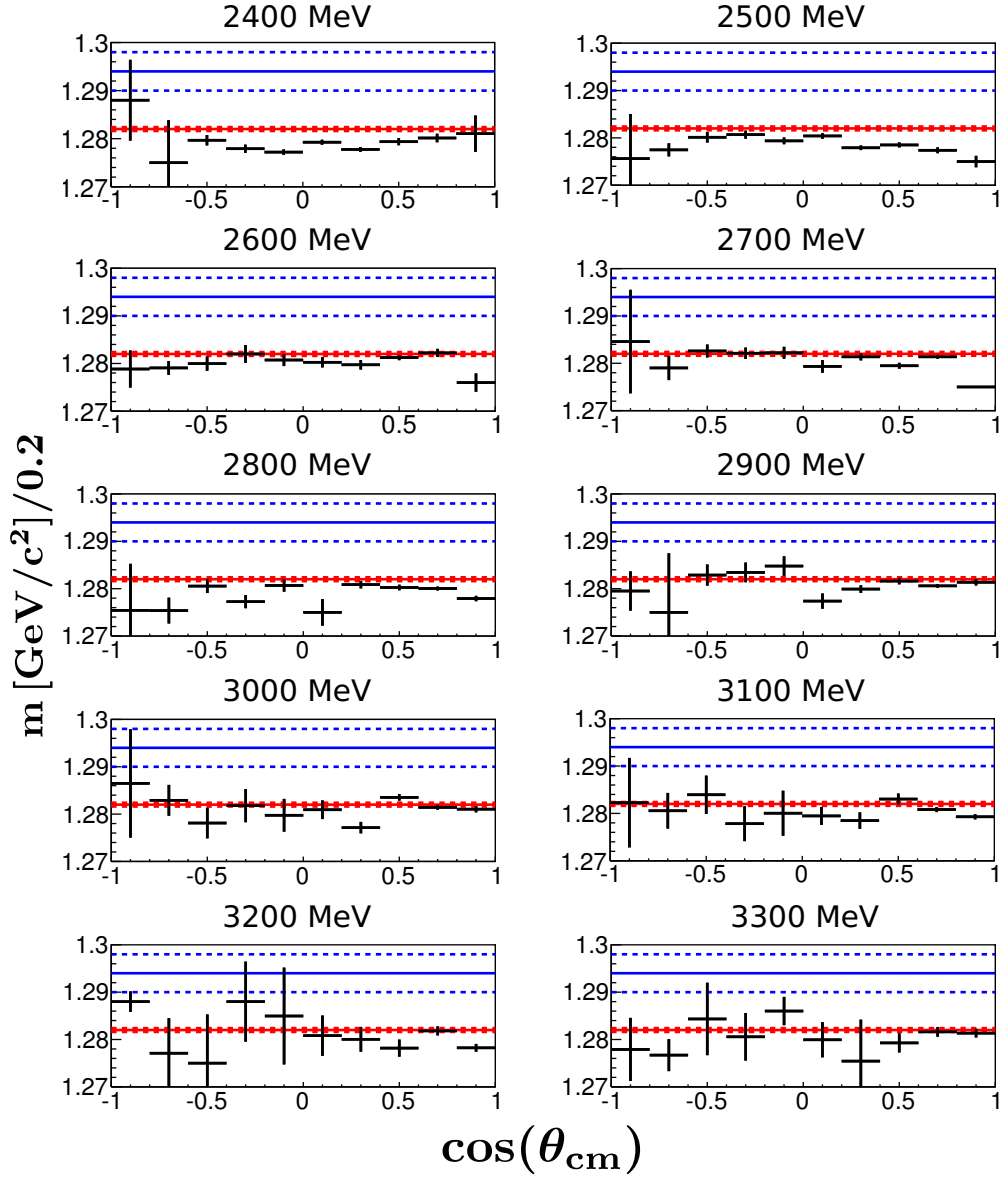
Figure 6.16: $X(1280)$ mass per cosine of the meson production angle in 100 MeV center-of-mass energy bins, red line indicates PDG mass of $f_1(1285)$ with $m = 1281.9 \pm 0.5$ MeV/c^2, dashed line represents the error. Blue line shows PDG mass of $\eta(1295)$ and blue dashed line its error with $m = 1294 \pm 4$ MeV/c^2.
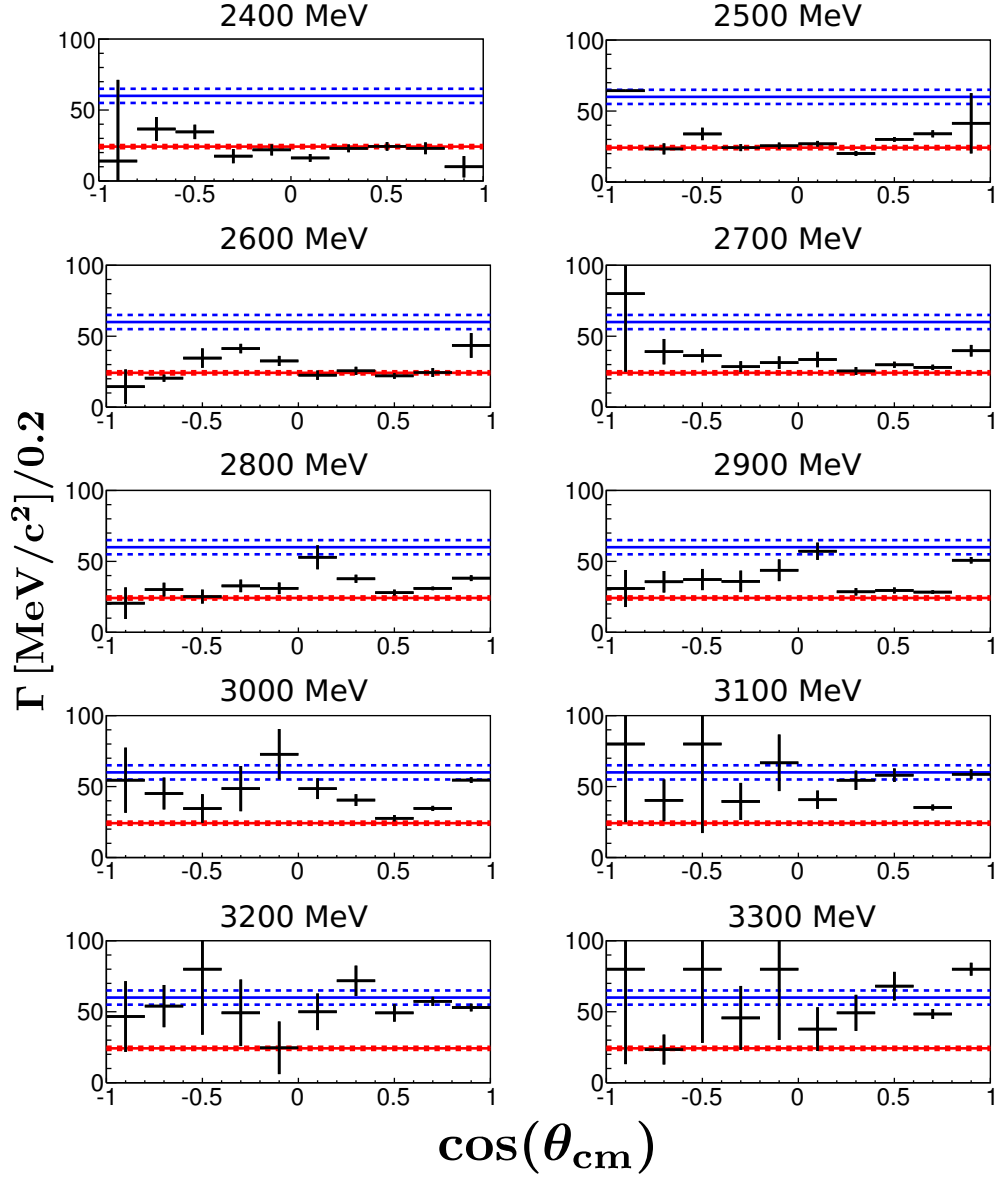
Figure 6.17: $X(1280)$ width per cosine of the meson production angle in 100 MeV center-of-mass energy bins, red line indicates PDG width of $f_1(1285)$, dashed line represents the error: $\Gamma = 24.2 \pm 1.1\,\mathrm{MeV/c^2}$. Blue line shows from the PDG reported width of $\eta(1295)$ and blue dotted line its error: $\Gamma = 55 \pm 5\,\mathrm{MeV/c^2}$.

and thus not the scope of this thesis. Apart from the mesons like η', $\eta(1295)$, $\eta(1405)$ and $f_1(1285)$ a lot of other resonances with sequential decays to the final state can be produced. One option to get a clue is to have a look at the results of the fits where the mass was allowed to vary during the adaption. In figure 6.16 the fit results of the mass of the $X(1280)$ are shown for the 100 MeV energy binning.

It is visible that near the production threshold of the $f_1(1285)$ and for some of the low
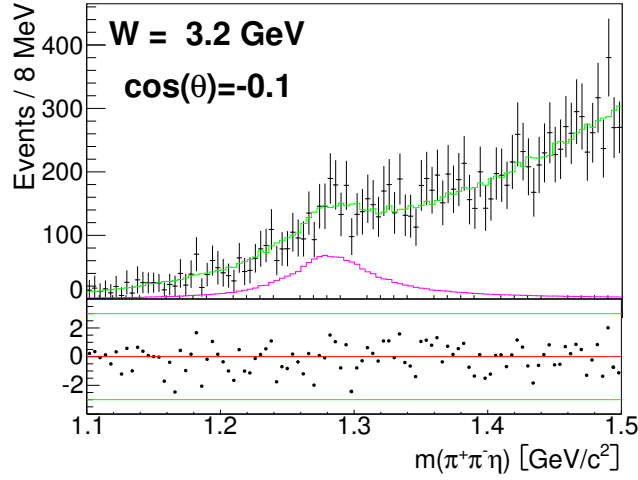
Figure 6.18: Fit for center-of-mass energy of $3.15\,\mathrm{GeV}$ and $\cos(\theta) = -0.1$. The black dots are the data points, the green line indicates the fit and the magenta line the $X(1280)$ contribution. The lower histogram shows the residuals, while the green line indicates zero and the red ones $\pm 3\sigma$. Mass and resolution of the $X(1280)$ Voigtian are fixed.

energy bins, the mass is fitted systematically to lower values compared to the following higher energy bins.

For the higher energies the $X(1280)$ yield is much lower due to the bremsstrahlung spectrum. Additional to this the cross section is lower in bins with a production angle not forward with respect to the beam direction, which can be seen also in figure 6.14. Due to the lower event numbers at higher energies the values of the statistical errors rise with rising center-of-mass energy. But within their errors the masses are better compatible with the value noted in the PDG for the $f_1(1285)$.

The fit results of all fits combined deliver a mass of $(1280.1\pm0.413)\,\mathrm{MeV/c^2}$, which supports the hypothesis of the $f_1(1285)$ being the $X(1280)$. Thereby one has to mention that up to now no systematic errors are included.

Additional to the fit with a free mass and a free resolution another fit was conducted were the mass and resolution were fixed and the intrinsic width was allowed to vary during the fit. The resolution was fixed, because the fit tends to divide the width of the signal to the intrinsic width and the Gaussian width of the resolution in equal portions. To get a clue on the real natural width of the meson it is important to fix those parameters to the values estimated in figure 6.4 and figure 6.16. The results for the width are shown in figure 6.17.

For the first six energy bins the values of the width are in a good agreement with the width of the $f_1(1285)$ and well below the width of the $\eta(1295)$. For an increasing beam energy the width becomes broader and the errors increase as well. In figure 6.18 an example fit for the last energy range and an angle perpendicular to the beam direction is shown. The magenta line shows the contribution of the $X(1280)$. It is visible that the fit has broadened the Voigtian of the $X(1280)$ to a huge width. Therefore, one might
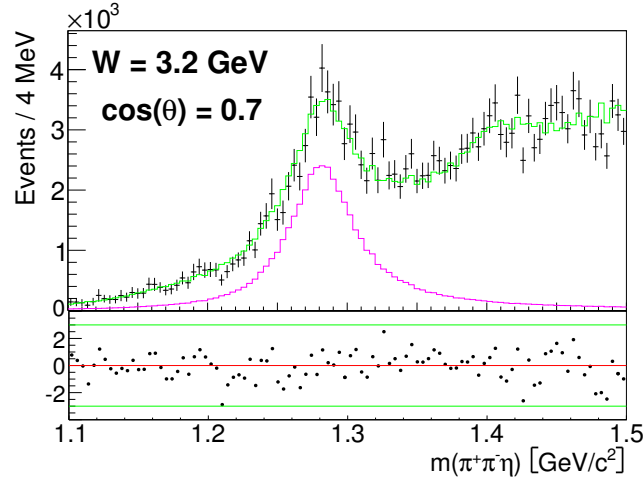
Figure 6.19: Fit for center-of-mass energy of 3.15 GeV and $\cos(\theta) = 0.7$. The black dots are the data points, the green line indicates the fit and the magenta line the $X(1280)$ contribution. The lower histogram shows the residuals, while the green line indicates zero and the red ones $\pm 3\sigma$. Mass and resolution of the $X(1280)$ Voigtian are fixed and the natural width is allowed to vary.

has to treat bins at a high energy and a $\cos(\theta)$ below zero with care. For the last two energy bins the width is mostly at the value of the $\eta(1295)$ width, but this includes a high statistical error compared to the lower energies. In contrast to this some of the forward-most angular bins show small error bars and a huge width.

An example fit for those bins is shown in figure 6.19. It is visible that the yield is much higher than the one for the bin with a $\cos(\theta)$ below zero. The peak at 1280 MeV/c^2 is described reasonably well by the fit, which is also visible in the residuals in the lower plot, too, as they do not show huge deviations. Additional to this the chosen angular bin is well before the corresponding bin covering the forward hole of CLAS which might hint on lower systematical errors. Even with the higher yield the fit needs to broaden the natural width. As a conclusion one can say that there are hints on a systematic shift of the width to higher values while the measured mass tends to be near the $f_1(1285)$ mass even at higher energies.

6.2.3 Decay Angle Distribution of $X(1280)$

Another possibility to gain knowledge about the identity of the $X(1280)$ is to have a look at the Dalitz plot of the final state particles $\pi^+\pi^-\eta$. The resonance can fragmenting via a three body decay into $\pi^+\pi^-\eta$ or it can convert via an intermediate resonance via a two body decay. The intermediate resonance will then decay immediately via a two body decay as well.

The Dalitz plot is a well established method to investigate the kinematics of a three body decay. The axes show the squares of the invariant masses of two pairs of the decay products. Four Dalitz plots are shown in figure 6.20.

Each Dalitz plot is filled with events within a sub-range of the $\pi^+\pi^-\eta$ mass with a width
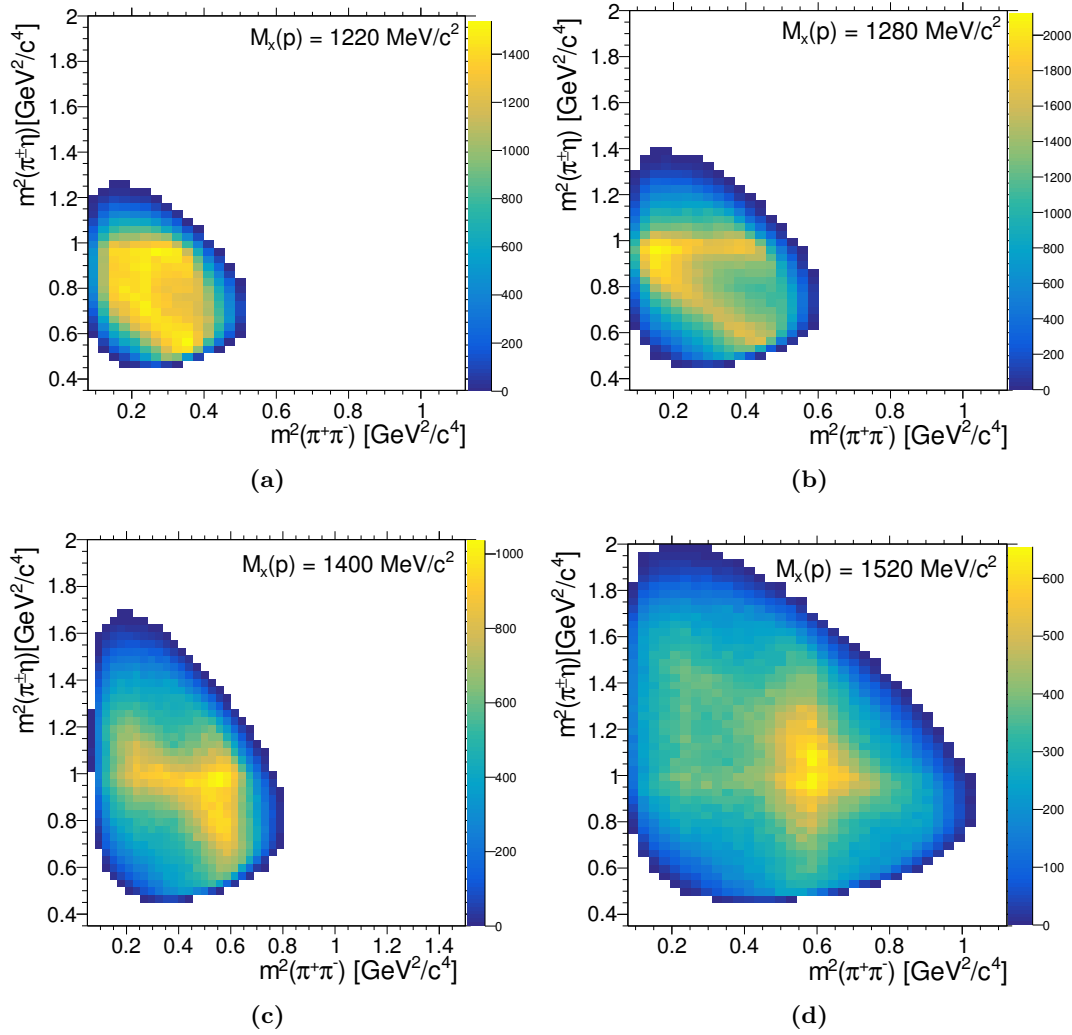
Figure 6.20: Dalitz distributions for different regions in the $\pi^+\pi^-\eta$ invariant mass each 60 MeV wide. The central of the energy region is mentioned in the upper right corner of each distribution.

of 60 MeV/c^2 and the mean of each sub-range is shown in the upper right corner. The x-axis shows the invariant mass squared of $\pi^\pm\eta$ and the y-axis the invariant mass squared of $\pi^+\pi^-$. In the case of an immediate three body decay of a spin zero resonance into three spin zero particles the Dalitz plot will not show any bands. One or more bands will show up in the distribution if an intermediate resonance is present.

All four Dalitz plots show such bands in yellow. Each plot shows a horizontal band at $m^2(\pi^\pm\eta)$ of approximately 0.96 GeV^2/c^4 and an additional diagonal band. The position of the horizontal band indicates the mass of the intermediate resonance with 980 MeV/c^2 and the particles' masses plotted on the y-axis are the daughter particles of this intermediate resonance. A resonance at 980 MeV/c^2 decaying to $\pi\eta$ is the $a_0(980)$. The plot in the
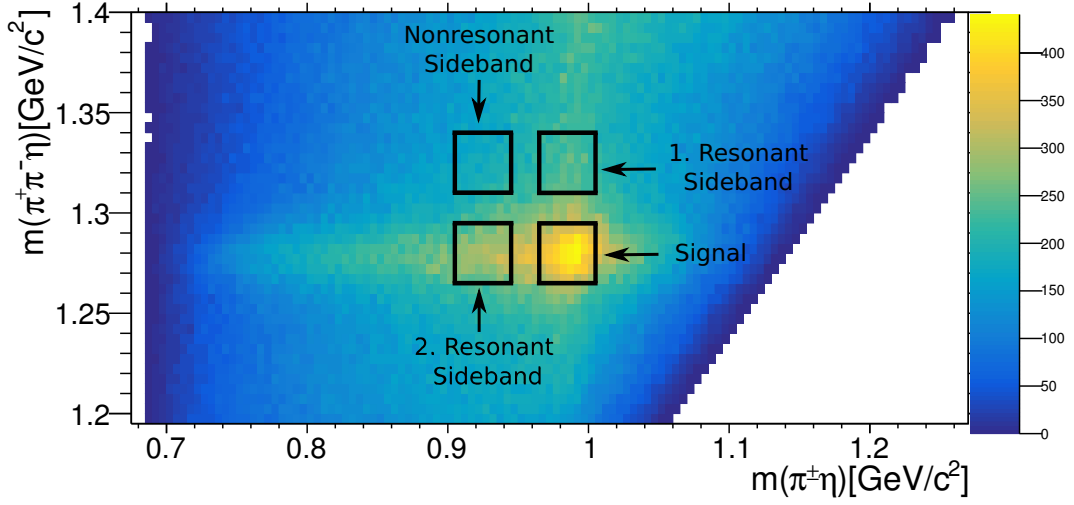
Figure 6.21: Invariant mass of $\pi^+\pi^-\eta$ vs. $\pi\eta$. Black boxes depict cuts for the signal region as well as two sidebands including resonant structures and a non-resonant sideband.

upper right corner shows the Dalitz plot of the mass range of the $X(1280)$ and the $a_0(980)$ bands are clearly visible.

Both the $f_1(1285)$ as well as the $\eta(1295)$ are known to decay via $a_0(980)\pi$, which therefore justifies no exclusion for either of the particles. In the Dalitz plot for the mass range including the $\eta(1405)$ the a_0 bands are visible, too.

For the last two mass ranges another resonance shows up as an vertical band. The mean of this vertical band lies at $m^2(\pi^+\pi^-) \approx 0.6\,\mathrm{GeV}^2/c^4$, which is associated with an invariant $\pi^+\pi^-$ mass of $770\,\mathrm{MeV}/c^2$. The corresponding particle to this mass and the decay products is the $\rho(770)$. This resonance can possibly be explained via t-channel production process. One conceivable explanation is that the incoming photon changes into the $\rho(770)$ while the proton changes to an excited baryon resonance, for example a N^*. A possible candidate is the $N(1535)$ which decays dominantly into $p\eta$. Several other scenarios are $\gamma p \rightarrow p\eta\rho$, $\gamma p \rightarrow \eta\Delta^*$ or $\gamma p \rightarrow \Delta^*$.

As a conclusion of this brief Dalitz plot discussion one can state that the resonance visible at an $\pi^+\pi^-\eta$ mass of $1280\,\mathrm{MeV}/c^2$ decays predominantly via a two body decay into $a_0(980)\pi$.

It is possible to gain information about the spin or parity of the decaying particle by examining the decay angle distribution. The first step to extract the decay angular distribution is to select a subset of suitable events. Hence, a cut has been applied on the $\pi^+\pi^-\eta$ mass to select events from $1.28\pm0.015\,\mathrm{GeV}/c^2$. The second cut has to be applied on the invariant $\pi^\pm\eta$ mass in the range from $960\,\mathrm{MeV}/c^2$ to $1\,\mathrm{GeV}/c^2$. The missing mass of the proton vs. the $\pi^\pm\eta$ mass is shown in figure 6.21 to demonstrate where the cuts have been applied.

The y-axis shows the $\pi^+\pi^-\eta$ mass and the x-axis the $\pi\eta$ mass. The lower right black box shows which region of events has been selected. As shown before, the $X(1280)$ enhancement is afflicted with a serious amount of background, therefore, it is advisable

to perform a two-dimensional sideband subtraction. Figure 6.21 shows that there are two bands visible, one vertical corresponding to the a_0 and one horizontal band for the $X(1280)$. Two two-dimensional sidebands are marked with black boxes, too. They are entitled with first and second resonant sideband and cover the same dimensions in range in the $\pi^+\pi^-\eta$ and $\pi^\pm\eta$ masses each as the signal box. Both regions are subtracted from the signal region.

Due to the region the sidebands cover, too many background has been subtracted. For this problem has been accounted for by adding an amount of non-resonant background. The region where the non-resonant background events have been taken from is shown with the upper left box. In most cases where this procedure is used sidebands are taken from the right and down side of the signal band, too. This is not possible in this case due to the limited phase space.

The decay angle discussed here is the angle between the quantization axis of $X(1280)$ and the flight direction of the a_0 in the helicity frame of the $X(1280)$. The helicity frame of a particle is dependent as its the rest frame with the quantized axis being the movement direction. This leads to the case that the decay products fly back to back. The distribution of its decay angle is related to the spin parity of the mother resonance. The resulting decay angular distributions can then be calculated for pseudoscalar as well as vector mesons.

$$0^{-+}: \quad \frac{d\sigma}{dcos(\theta^X_{a_0})} \propto |d^0_{0,0}|^2 = c \tag{6.2.1}$$

$$1^{++}: \quad \frac{d\sigma}{dcos(\theta^X_{a_0})} \propto a|d^1_{0,0}|^2 + b(|d^1_{1,0}|^2 + |d^1_{-1,0}|^2) = a \cdot cos(\theta^X_{a_0})^2 + b \cdot sin(\theta^X_{a_0})^2 \tag{6.2.2}$$

Where the Wigner d functions are defined as $d^J_{\lambda_J(\lambda_{a_0} - \lambda_\pi)} = d^J_{MJ,0}$ with J the spin of the mother particle, λ is the helicity of the mother particle and the daughter particles respectively.

Figure 6.22 shows the decay angular distributions for $X(1280)$ decaying to $a_0^+\pi^-$, $a_0^-\pi^+$ and both together. All angular distributions are sideband subtracted and efficiency corrected.

The functions mentioned above are fitted to the distributions with the free parameters c, a and b. The blue line depicts the fit for the assumption of a pseudoscalar resonance present and the red line one for a vector meson. The $X(1280)$ decaying to $a_0^+(980)\pi^-$ shows a parabolic distribution, which rules out a pseudoscalar resonance as the mother particle. On the other hand a fully flat distribution does not exclusively favor a pseudoscalar resonance. If a vector meson is fully "unaligned", $a = b$, the decay angular distribution in its helicity frame is flat.

Table 6.2: χ^2/ndf for fits to the different decay modes of the $X(1280)$.

decay mode	0^{-+}		1^{++}	
	χ^2/NDF	*prob*	χ^2/NDF	*prob*
$a_0^+\pi^-$	65.63/13	$5.06 \cdot 10^{-9}$	17.56/12	$1.3 \cdot 10^{-1}$
$a_0^-\pi^+$	43.28/13	$4.04 \cdot 10^{-5}$	33.84/12	$7.15 \cdot 10^{-4}$
$a_0\pi^\pm$	58.59/13	$9.38 \cdot 10^{-8}$	27.62/12	$6.29 \cdot 10^{-3}$

(a) $X(1280) \rightarrow a_0^+ \pi^-$

(b) $X(1280) \rightarrow a_0^- \pi^+$

(c) $X(1280) \rightarrow a_0^\mp \pi^\pm$
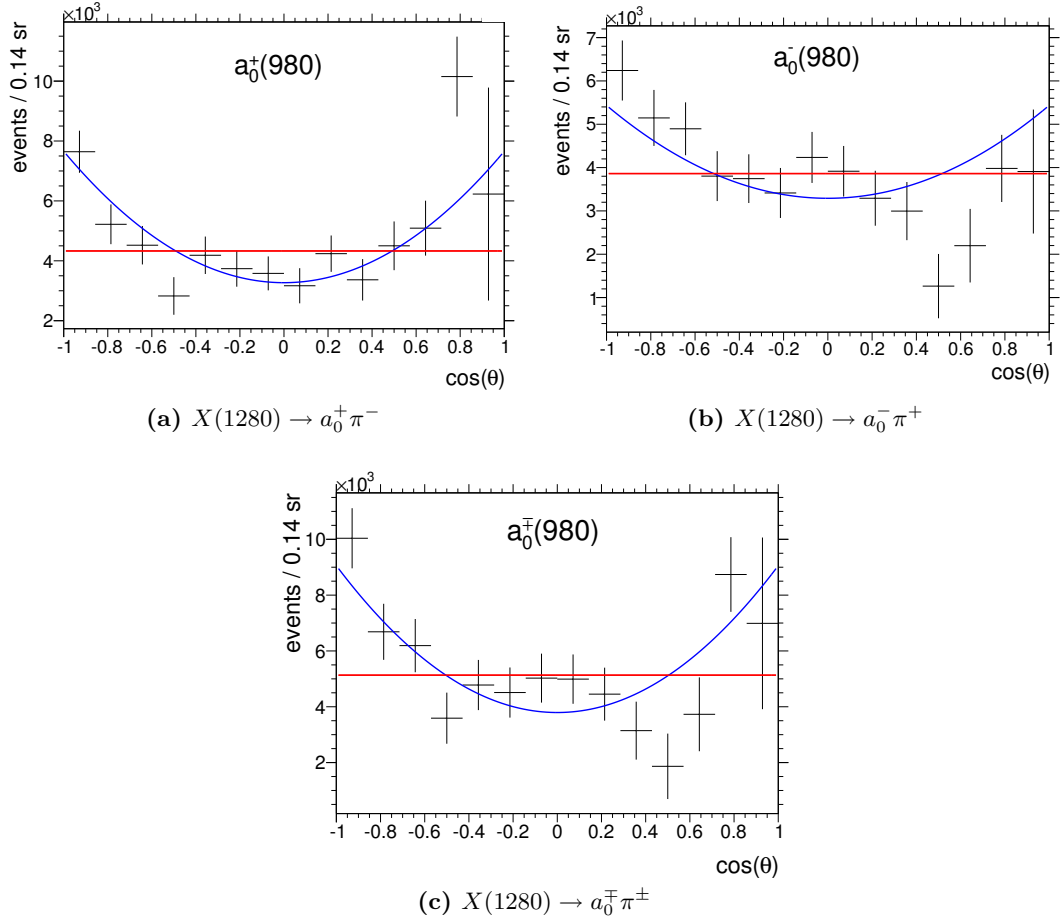
Figure 6.22: Distribution of the decay angle of $X(1280)$ to $a_0(980)\pi$. (a) $a_0^+(980)\pi^-$, (b)$a_0^-(980)\pi^+$ and (c) $a_0(980)^\mp\pi^\pm$. Red: 0^{-+}, Blue: 1^{++}.

The table 6.2 shows the χ^2/ndf for each decay mode and the two fits respectively. If one compares the reduced χ^2 of the two fits it is visible that the 1^{++} hypothesis is favored for the decay to $a_0^+\pi^-$ and the combination of both decays. The 1^{++} hypothesis is, moreover, favored for the decay to $a_0^-\pi^+$, but the probability is less good which may be because of background contributions.

At last it is to mention that the $X(1280)$ is afflicted with a high background contribution and the sideband subtraction leads to systematic errors unattended in this analysis. In general one can say that the 1^{++} hypothesis describes the distribution better.

6.2.4 Cross Section for the Reaction $\gamma p \rightarrow pX(1400)$

Due to the fact that the contribution from the $X(1400)$ is smaller in comparison to the $X(1280)$ yield energy ranges of $200\,\mathrm{MeV}$ are chosen here for the determination of the differential cross section. In total 18438 ± 665 $X(1400)$ events have been determined.

The first histogram covers the energy interval close to the production threshold at the $\eta(1405)$ mass. One can see a steep rise towards the backward-most bin which is significant
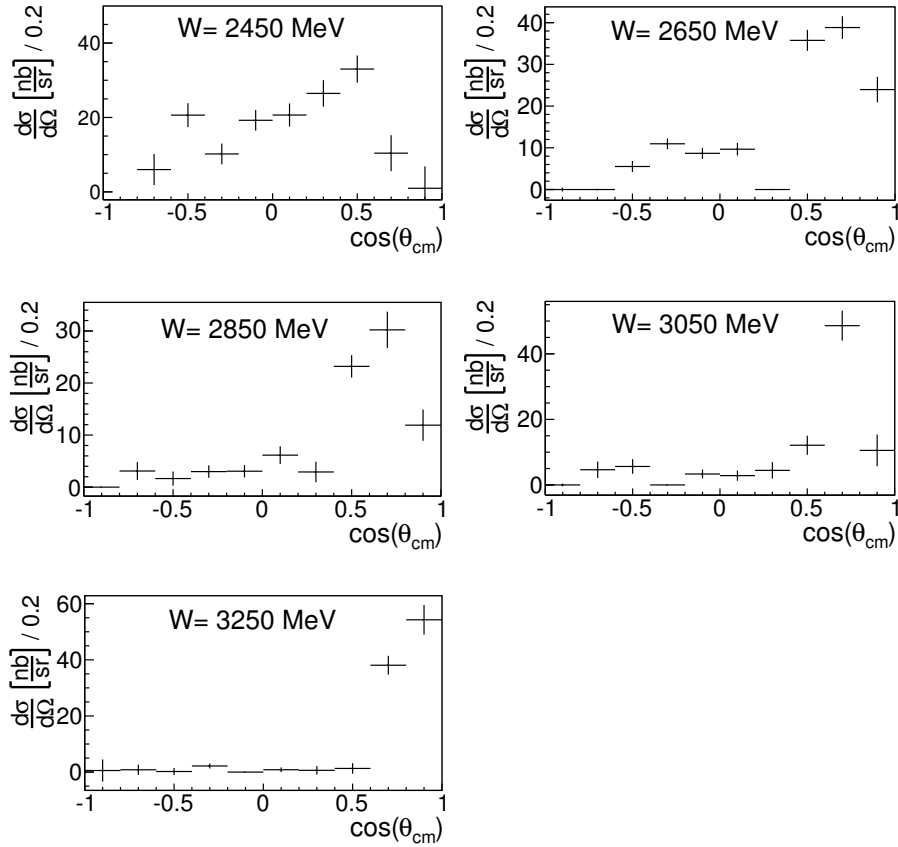
Figure 6.23: Differential cross section of the $X(1400) \rightarrow \pi^+\pi^-\eta$. The associated energy bin is written in the top of each plot. The x-axis shows the cosine of the production angle and the y-axis $d\sigma/d\Omega$.

within its errors, but it is to mark that the most forward and backward angles contain acceptance gaps of the CLAS detector. Nevertheless, the distribution at this center-of-mass energy is relatively flat. A flat distributed cross section is a hint for a s-channel production mechanism.

With increasing center of mass energy a rise in forward direction becomes more and more prominent. It becomes apparent that a significant drop down in the forward most angular bin appears within all energy ranges except the highest one. This drop down has to be treated with caution due to limitations in the detector acceptance. A drop in the cross section for the forward most bins has been predicted by Regge model using theories fro the photoproduction of η, $f_1(1285)$ and $\eta(1295)$, which might applicable here, too, although no calculations have been made for the photoproduction of the $\eta(1405)$ [37, 38]. At the highest energy the differential cross section features a flat distribution in backward direction and a peak in forward direction.

The behavior of the differential cross section of the $X(1400)$ is very similar to the one extracted for the $X(1280)$. Both start with a flat distribution at the production threshold of the regarded resonance and continues with a steep rise in forward direction with
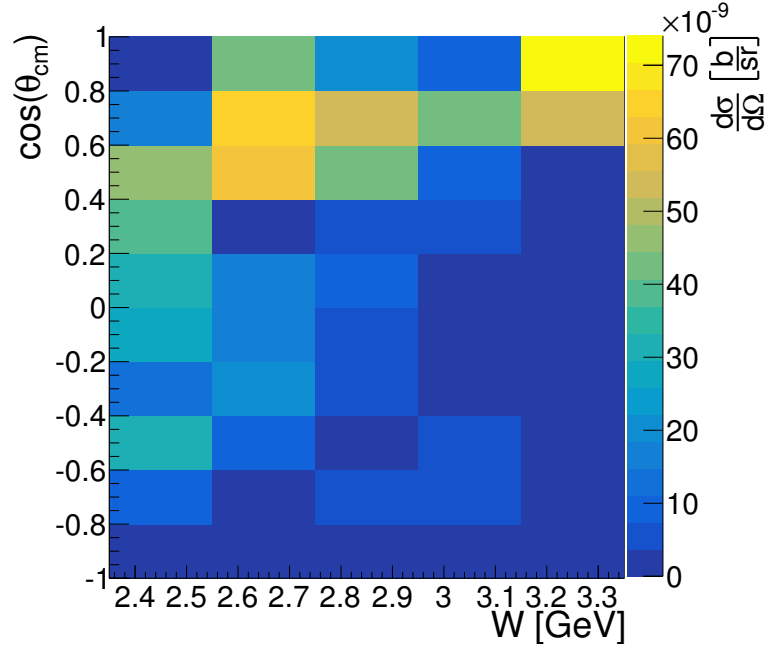
Figure 6.24: Differential cross section of the $X(1400) \rightarrow \pi^+\pi^-\eta$. The x and y-axis show the corresponding energy range and the cosine of the production angle respectively while the z-axis displays $d\sigma/d\Omega$.

increasing energy. Generally the amplitude of the $X(1400)$ cross section is a factor of two to three lower than for the $X(1280)$.

In figure 6.24 the same differential cross section for the reaction $\gamma p \rightarrow p X(1400)(\pi^+\pi^-\eta)$ is shown as a two-dimensional plot to achieve a better overview of the alteration of the cross section with energy and angle.

Again it becomes evident that the highest cross section is around the production threshold and at angles around 0.7. This rise in statistic can be seen in the $AICc$ histograms showed in the foregoing sections at the same energies and angles, which can now be associated with the rise in the production of the considered resonances.

7 Measurement of the Differential Cross Section of the Reaction $\gamma p \rightarrow p\eta'$

In order to ensure that an analysis is performed properly it is helpful to compare the results to former published results, if possible. Therefore, the differential cross section for the η' is extracted and compared to a published result by the CLAS collaboration on the g11 data set ([39]).

In the first step the remaining background below the η' has to be subtracted using the aforementioned method. To improve the level of comparability between the published results and this work the background is subtracted with the η'as reference coordinate instead of the η. The steps taken will be described in the following section.

In the next step the extracted cross section will be showed weighted with the Q-factor derived from the η' as well as weighted with the Q-factors derived from the η.

7.1 Event Based Background Rejection

In order to improve the resolution of the η' visible in the $\pi^+\pi^-\eta$ mass a cut has been applied in the region from $0.5\,\mathrm{MeV/c^2}$ to $0.6\,\mathrm{MeV/c^2}$ on the missing mass of the $p\pi^+\pi^-$. Additionally to this the kinematically fitted four-vectors have been used in combination with a cut on the probability of $p > 0.01$. In figure 7.1 the invariant mass of $\pi^+\pi^-\eta$ is shown in the region of the η' mass. The Q-factors derived in the former chapters are not applied here. As one can see there is some background left below the signal. To extract a cross section it is necessary to know the exact number of events of the desired particle. The Q-factor method enables one to remove the background and obtain the number of η' events in this data sample.

For the application a certain set of non-reference coordinates has to be chosen. The ones used for the background reduction with the mass of η' as reference coordinate are shown in table 7.1. In contrast to the foregoing method the set of non-reference coordinates is reduced from eight to only two coordinates.

Table 7.1: Kinematic variables used in the background rejection with $m(\eta')$ as reference coordinate.

Quantity	Non-Reference-Coordinates
Beam Energy	E_γ
η' production angle	$cos(\theta_{\eta'}^{c.m.})$

These non-reference coordinates are used to calculate the distances of every event to every other event in phase space. After this calculation the 200 nearest events are selected. The number of nearest neighbors was derived by performing systematic studies of the
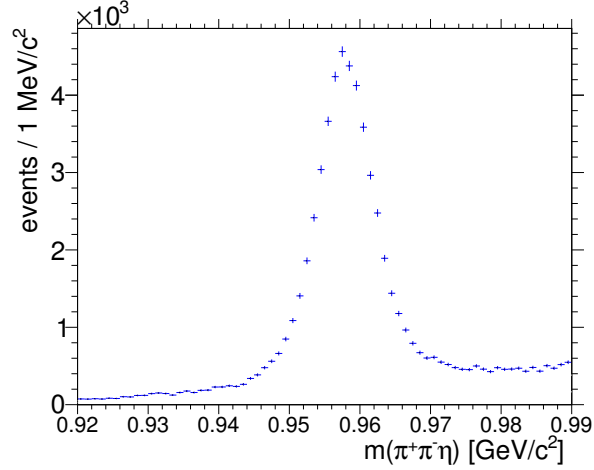
Figure 7.1: Invariant $\pi^+\pi^-\eta$ mass in the region of the η'.

fit quality with different numbers of events to be fitted. The number of 200 was chosen because it guaranteed a sufficiently small cell of phase space and an overall good fit quality of the fit to the reference coordinate.

The width of the η' is dominated by the detector resolution, because its natural width is only $\Gamma = 199\,\text{keV/c}^2$. Therefore, a Voigtian distribution is not necessary and a simple Gaussian was chosen as signal function and a first order Chebychev polynomial for background.

$$
\begin{aligned}
b(x) &= C_0 + C_1 x, \\
s(x) &= e^{\frac{(x-\mu)^2}{2\sigma^2}}.
\end{aligned}
$$

The mean of the Gaussian is allowed to vary between $\pm 1\,\text{MeV/c}^2$ and the width σ between $200\,\text{keV/c}^2$ and $20\,\text{MeV/c}^2$.

In order to show how well the background below the η' is subtracted it is best to look at the separation of background and signal in the invariant mass distribution of $\pi^+\pi^-\eta$ in figure 7.2a.

The Q weighted distribution has no background contribution any more and the smooth behavior of the background indicates a good identification of background and a proper assignment of the weights to the events respectively. This makes it possible to weight the differential cross section of $\gamma p \to p\eta'$ as well and normalize for the η' yield that way. More information about the extraction of the differential cross section can be found in section 6.1.

7.2 Normalization

As mentioned before the differential cross section can be calculated according to

$$
\frac{d\sigma}{d\Omega} = \frac{Y}{2\pi\,N_\gamma\,\rho\,l\,A_{CLAS}\,\Delta_{cos\theta_{CM}}\,\mathcal{B}}\ ,
$$

where Y is the yield of the desired particle (cf. section 7.3), N_γ is the number of photons hitting the target (cf. section 6.1.1), ρ and l are the density and length of the CLAS *g12* target (cf. section 6.1.2), A_{CLAS} is the acceptance of the CLAS detector (cf. section 7.4) and $\Delta_{cos\theta_{cm}}$ is the bin width of the distribution in cosine of the production angle in the center-of-mass frame.

The yield of the particle is corrected by the appropriate branching fractions $\mathcal{B}$. For η' this involves the branching fraction of η' decaying to $\pi^+\pi^-\eta$ and the branching fractions of η decaying into further states. The η branching fractions are not taken into the normalization because they are accounted for by simulating all strong contributing decay modes according to their branching fractions.

The η' fraction has to be taken into the normalization for the yield extraction with the Q-factor method with the η' as reference coordinate (section 7.1), because for this option the background below the η' seems to be properly removed, but it can happen that for example wrongly chosen η candidates form peaking background under the η' which can not be found by this yield extraction. More information can be found in section 4.

The yield extraction with method two, using the Q-factor method with the η as reference coordinate yields this advantage, for this see section 3.9.3 and section 4. Therefore, the branching fraction for η' decaying to $\pi^+\pi^-\eta$ has not be taken into the differential cross section normalization.

7.3 Yield Extraction η'

The background below the η' has been subtracted in two different ways, as explained in sections 7.1 and 3.9.3. For both ways of the Q-factor method the η' background is removed to a level of less than 5% of the signal. Therefore, the events weighted with Q yield more than 95% signal events. In this case one can simply take the sum of weights as yield for the calculation of the cross section

$$Y\left(\sqrt{s}, \theta_{CM}^{\eta'}\right) = \sum_i^N Q_i,$$

where Q_i are the probabilistic event weights and N is the number of all events.

In figure 7.2 the obtained distributions after the application of the different weights are shown. The left one illustrates the $\pi^+\pi^-\eta$ mass in the region of the η' weighted with the Q-factors derived by using this method to subtract the background while the η acted as reference coordinate. The right one shows the same distribution, but with the background subtraction where the η acted as reference coordinate.

The Q weighted distribution in both histograms depicts the signal yield, each events contribution weighted with its probabilistic event weight. In the left one there is nearly

Table 7.2: Reconstructed event number for η'.

Particle	$\mathcal{Y} \pm \sigma_{stat}$	
	Q-values η'	Q-values η
η'	51494 ± 226	48864 ± 161
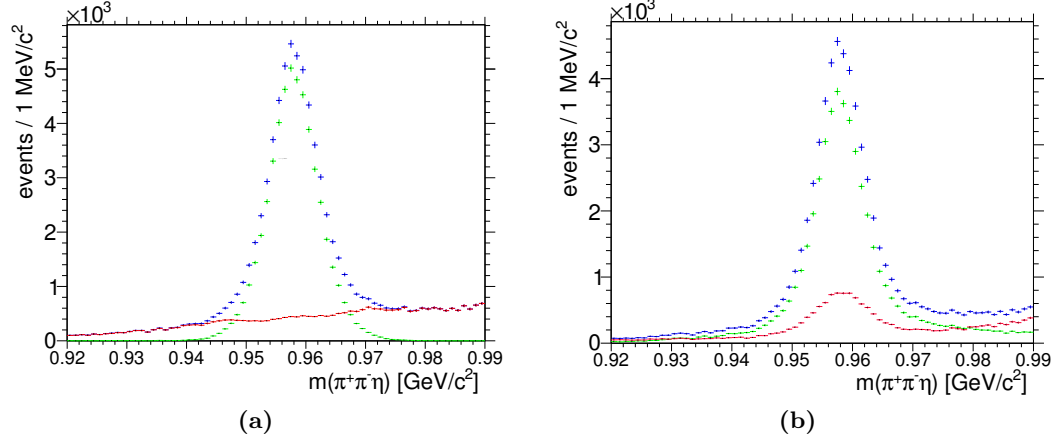
Figure 7.2: (a) Invariant mass of $\pi^+\pi^-\eta$ weighted with weights from Q-factor method with η' as reference (b) Same distribution, but Q-factor method with η as reference coordinate. Blue: unweighted spectrum, Green: Q weighted spectrum and Red: 1-Q weighted spectrum.

no background remaining while in the right there is a small number still present, but relative to the signal it is less than 5%. In table 7.3 the extracted number of η' events for both methods is presented.

For both methods a cross section can be extracted and is shown in section 7.5.

7.4 Acceptance Correction

To correct the η' cross section for the aforementioned efficiencies (section 6.1.3) we use Monte Carlo events generated for $\gamma p \to p\eta'[\pi^+\pi^-\eta]$ with the η decaying into the particles with the major branching fractions. For the η' channel 14 million events have been generated. Generated Monte Carlo events and accepted Monte Carlo events are treated with the same analysis procedure as the data except the probabilistic event weight method. They are divided in the same energy bins as the cross section and the production angle of η' is filled in histograms with the same binning as the data. In the next step the histograms of the accepted Monte Carlo data are divided by the raw Monte Carlo events.

These distributions are fitted with a third order polynomial to get an acceptance function for each energy bin dependent on the production angle. This enables us to derive an efficiency depending on the beam energy and production angle, $\epsilon(E_\gamma, \cos(\theta))$. Each events contribution to a distribution gets weighted with $1/\epsilon$.
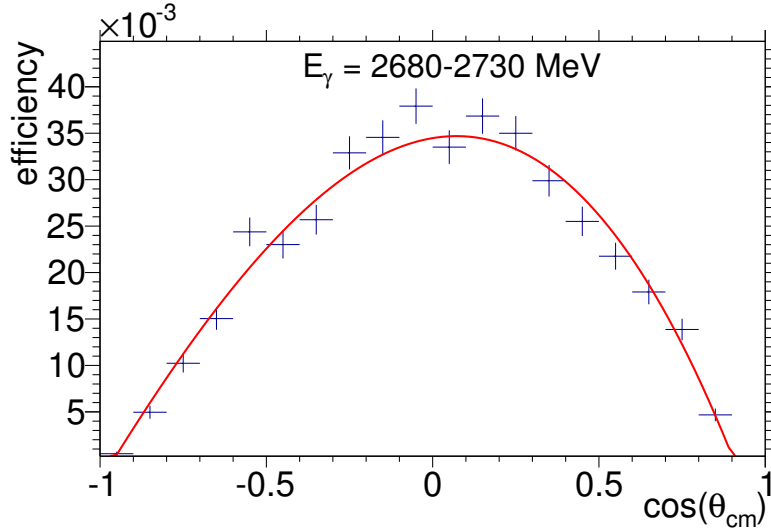
Figure 7.3: Acceptance for $\gamma p \to p\eta'$. The x-axis shows $cos(\theta_{\eta'}^{c.m.})$ and the y-axis the efficiency binned for a subrange in E_γ.

7.5 $\gamma p \to p\eta'$ Cross Section

This section will show the cross section of the reaction $\gamma p \to p\eta'$.

In this section the cross sections for the reaction $\gamma p \to p\eta'$ is shown. It is displayed weighted with the Q-factors obtained in this chapter as the former published results are weighted with Q-factors where the η' is the reference coordinate, too. Additionally the cross section is shown weighted with the Q-factors obtained in section 3.9.3 as this is the method chosen for the results of this work.

The differential cross section is divided in ranges of the cosine of the production angle of the meson with the bin width of 0.1. Additional to this the data are subdivided in bins of the center-of-mass energy W. Those bins are not equidistant in order to achieve a better comparability to the former results.

A result for the cross section $\gamma p \to p\eta'$ was published in [39] in 2009 by the CLAS collaboration. The former analysis was based on the *g11* data set and used the Q-factor method to reduce background below the η' as well as partial wave analysis methods to achieve a good acceptance correction. Therefore, the same Q-factor method has been conducted to have a good base for a comparison.

The Q-factor method with the η as reference coordinated was used, because we are interested in the higher mass states mostly.

The vertical bars on the points show the statistical uncertainty only. As mentioned above the cross section weighted with the two different sets of Q-factors should yield nearly the same result as the cross section is not dependent on the final state particles. It is to mention that the efficiency correction in [39] was made using a partial wave analysis.

In figure 7.4 the differential cross section with Q-factors obtained by using the η' as reference is shown.

Both results show a prominent peak in forward direction. For the most forward angles the
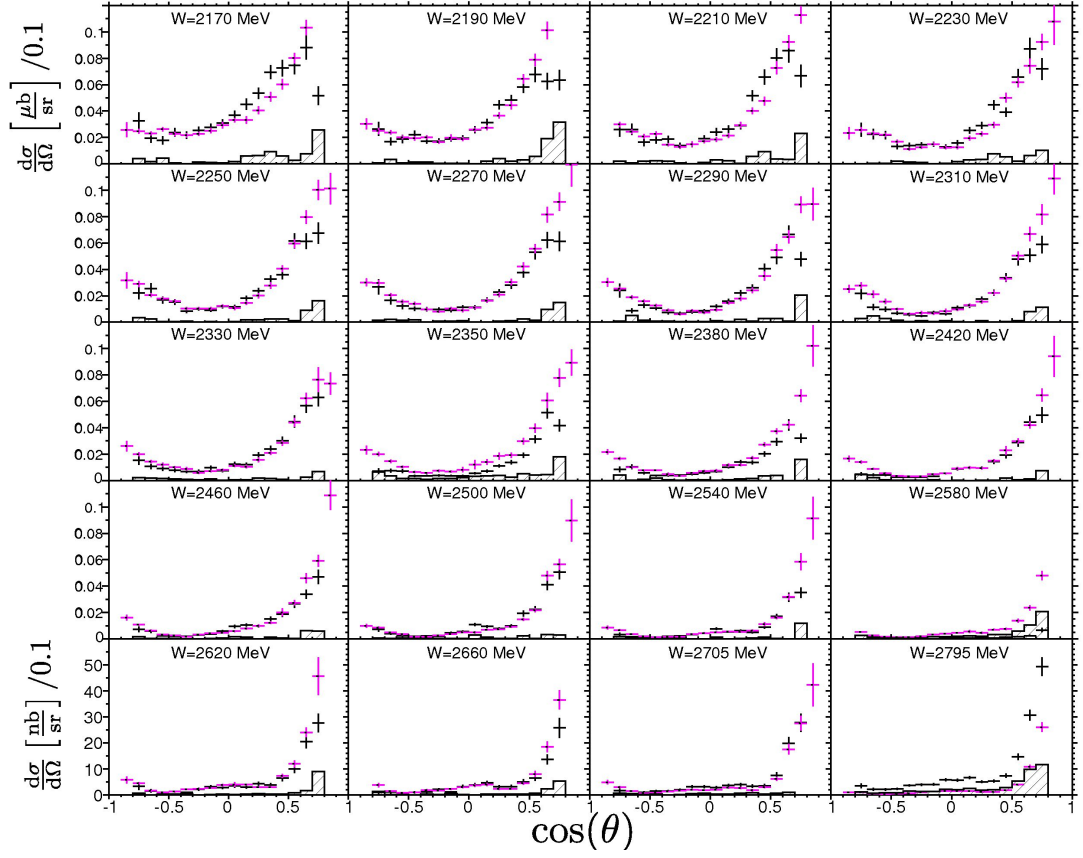
Figure 7.4: Differential cross section for the reaction $\gamma p \to p\eta'$ with Q-factors obtained from η'. The x-axis shows the cosine of the production angle. The y-axis shows the differential cross section in $\mu b/sr$ for the first 16 bins and for the last four in nb/sr. The black points are the result of this work and the magenta ones show the published results from the CLAS collaboration [39]. The black shaded histogram shows half the difference between the two cross sections.

data are missing because the forward region is not covered by the CLAS detector. The strong increase in cross section towards the forward angles might be due to a t-channel meson exchange. The cross section does show a smaller, but significant rise towards the backward angles, too, which is an indication for u-channel production processes. This leads to the assumption that there are baryon u-channel exchanges contributing. Around an energy of 2.46 GeV a hump in the transverse direction starts to rise which might be an evidence for the combination of baryon resonance production and t-channel meson exchange.

In comparison to the differential cross section of the $X(1280)$ both cross sections have a steep rise in forward direction in common, as well as the drop in the forward-most angular bin. The next thing they have in common is the drop down to nearly zero in the region perpendicular to the beam direction. In difference to the η' cross section the
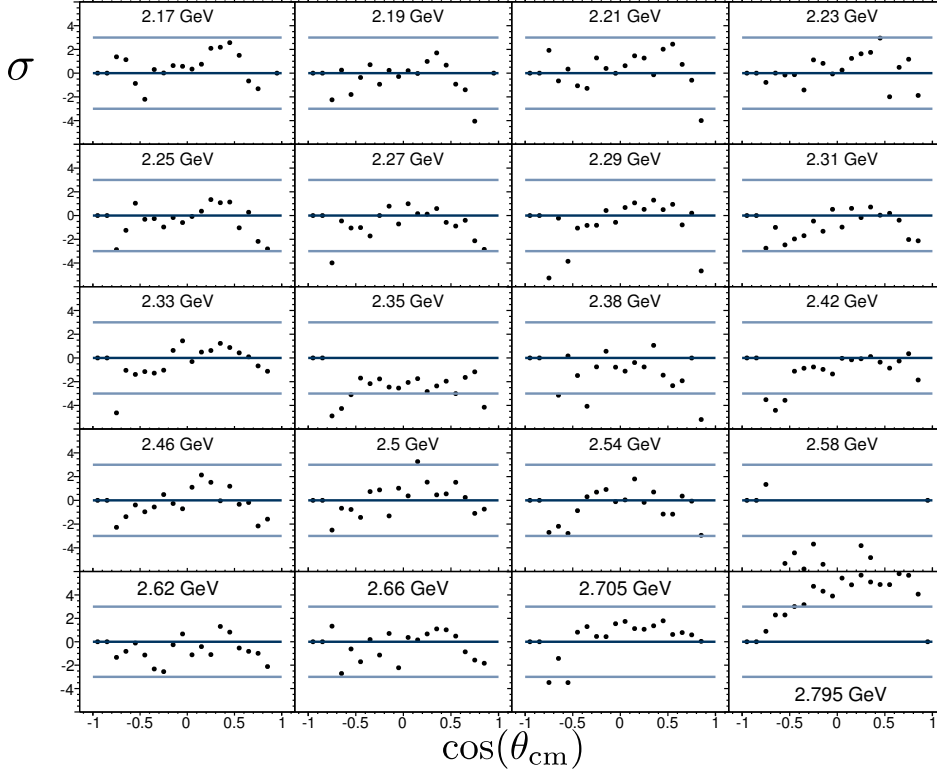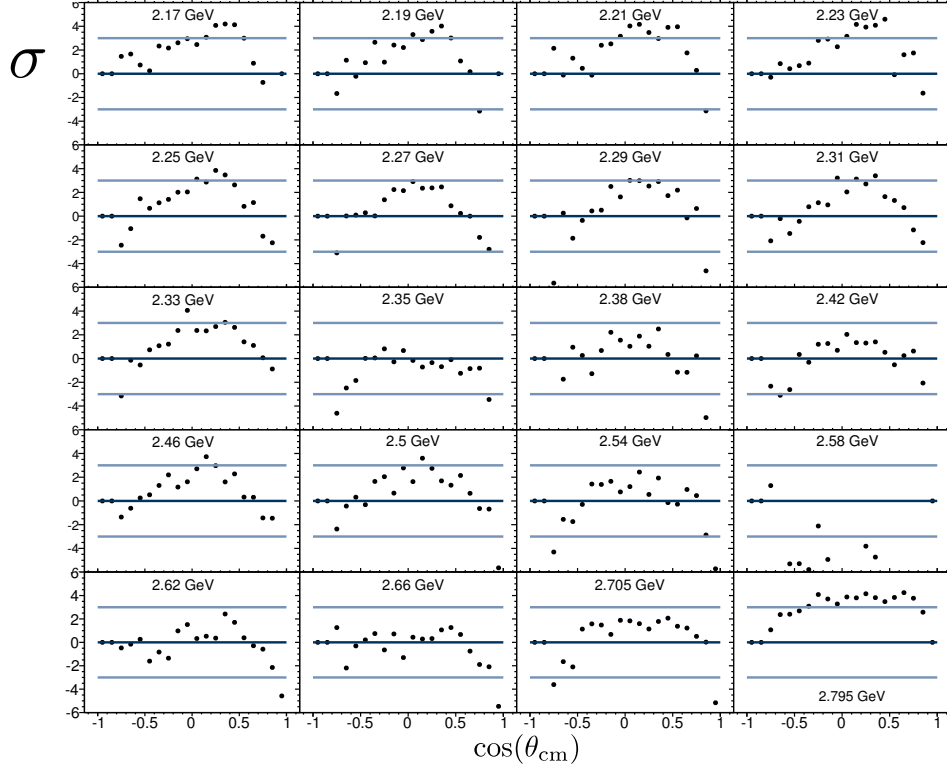
Figure 7.5: Difference between results of differential cross sections for $\gamma p \to p\eta'$ with Q-factors obtained from η'. The x-axis shows the cosine of the production angle. The y-axis shows the deviation in sigma. The dark blue line depicts a σ of zero whereas the light blue lines depict a σ of 3.

$X(1280)$ cross section does not show the rise towards the backward angles hinting on an u-channel process.

In figure 7.5 the deviation from the former results is shown, when the Q-factors are obtained from η as reference coordinate. The dark blue line is a guide for the eye to show where a σ of zero would be. The light blue lines show a σ of three. σ values of zero in the first two bins or the last bin are equal to empty bins and can be ignored. The deviation is calculated bin wise by taking the difference of the cross section in each bin and normalize it with the quadratic addition of the bin errors. It is visible that most of the bins are well within a three sigma deviation. Most of the deviations bigger than three sigma are in the most backward and forward directions.

The two cross sections are mostly consistent with each other. It is visible that for the lower energies a greater discrepancy from the former published cross section shows than for the high energy bins. The huge decrease in the range with a mean center-of-mass energy of $2.58\,\text{GeV}$ is due to broken PMTs in the tagging system. This leads to the reduction of the event rate in the order of a magnitude for these energies. Nevertheless our cross section is in a good agreement with the former published one in all other bins. The main deviations are in the forward-most and backward-most angles and might be
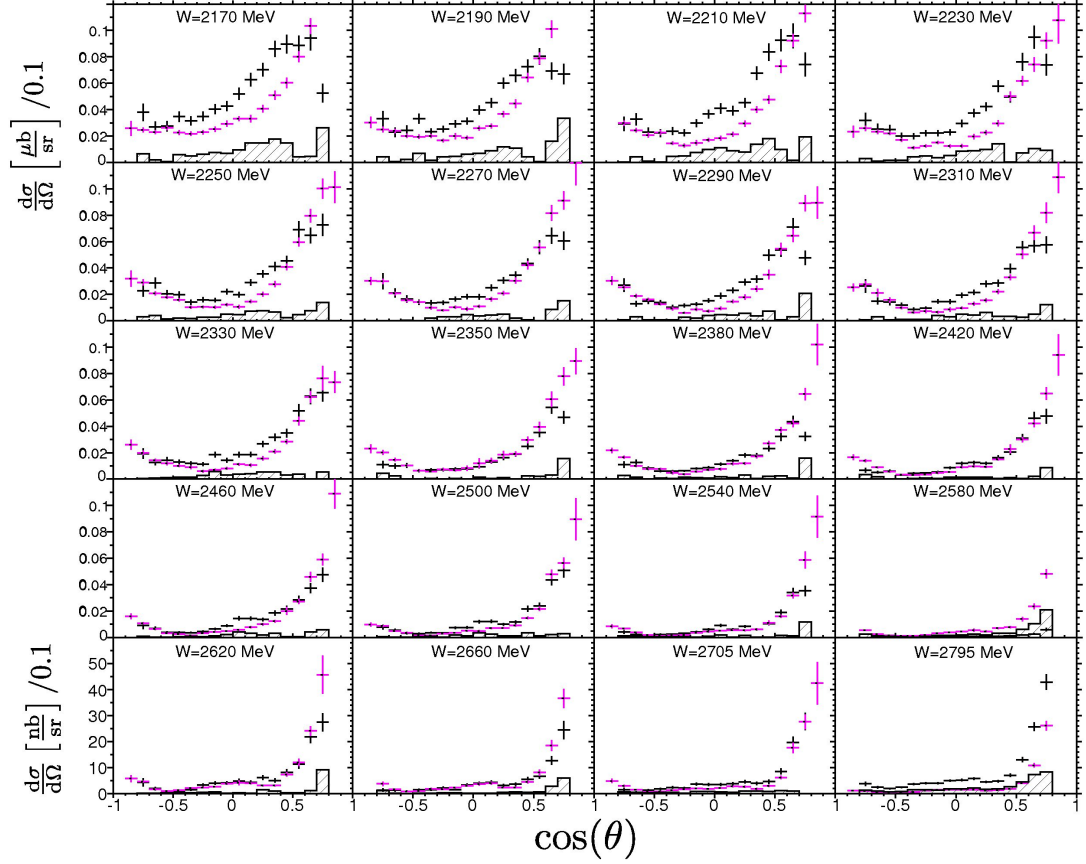
Figure 7.6: Differential cross section for the reaction $\gamma p \rightarrow p\eta'$ with Q-factors obtained from η. The x-axis shows the cosine of the production angle. The y-axis shows the differential cross section in $\mu b/sr$ for the first 16 bins and for the last four in nb/sr. The black points are the result of this work and the magenta ones show the published results from the CLAS collaboration based of g11 data [39]. The black shaded histogram shows half the difference between the two cross sections.

due to an insufficient efficiency correction. Overall it is made plain that the analysis procedure used for this results works well to confirm and match the published results.

In a second step it is important to prove that we can reproduce the former results also if the background is subtracted with the η as reference coordinate. The η' decays into two charged particles, which momenta and energies can be reconstructed precisely, and the η which can be reconstructed as missing particle only. This leads to the assumption that the main background contribution in the $\pi^+\pi^-\eta$ mass is caused by this reconstruction method.

Figure 7.6 shows the differential cross section for η', but with Q-factors obtained from the η. There are discrepancies for the low energy bins. The cross section tends to bend down in forward direction in contrast to the former results. The backward region is adequately good described. There are huge discrepancies for angles around $\cos(\theta)$ of zero. This can be explained in two ways. The first is that there is still background from events which

Figure 7.7: Difference between results of differential cross sections for $\gamma p \to p\eta$ with Q-factors obtained from η. The x-axis shows the cosine of the production angle. The y-axis shows the deviation in sigma. The dark blue line depicts a σ of zero whereas the light blue lines depict a σ of 3.

are no η', and therefore underlie a different production mechanism. This assumptions is contradictory to the results shown in figure 4.4, where it is shown that the peaking background is well described. Another explanation is that the background below the η', which is still there if one conducts the Q-factor method on the η', distorts the differential cross section. Possible background channels have been listed in section 4.

The main contribution was found in the decay $\eta' \to \pi^0\pi^o\eta(\pi^+\pi^-\pi^0)$. It is possible to interchange the neutral pions with the charged pions if the kinematic characteristics of the four particles are similar. Then the charged pions are mistaken as pions coming from the η' decay. The neutral pions are reconstructed as η which leads to a broadening of the signal and produces the horizontal band below the η'. This effect vanishes with higher beam energies. All distributions with a center-of-mass energy higher than 2.35 GeV show a fairly good consistency. This can be explained with a broadening of the available phase space, which leads to less background directly at the η' mass . For a last comparison we will show the deviation in each bin in center-of mass-energy and bins of $cos(\theta)$ in σ in Figure 7.7, which depicts the same behavior as discussed before. Besides the systematic deviation the overall deviation does not exceeds three σ in most cases.

The differential cross section depends on the production mechanism of a meson only and is independent of the final state of this meson. Nevertheless the cross section shows a

different behavior if the Q-factors are derived if the η or η' is used as reference coordinate. This difference could be explained with the possibility to transpose the neutral pions from the η' decay with the charged pions from the η decay, which has been proved by Monte Carlo studies. This is only one explanation and it might be possible that other competing reaction do form background below the η' as well. In any case the probabilistic event weight method with the η as reference coordinate seems to be capable to differentiate those events from events with the wanted decay chain. It can be assumed that the permutation is not possible for all kinematic situations and it might be energy dependent as well as dependent on the production angle. This is confirmed by the shape of the deviations. Those appear for certain angular regions as well as low energies. With rising energies the deviation decreases.

As a outcome one can state that the differential cross section has been reproduced to a good extent and matches best for the higher beam energies where the production of the states of interest starts.

8 Summary and Conclusion

The photoproduction of excited η resonances off protons is studied using data recorded with the CLAS detector at Jefferson Lab (Newport News, Virginia).

The main goal of this analysis is to shed further light on the nature of excited η mesons and their classification regarding the pseudoscalar meson nonet. The *g12* data set made it possible to extend the energy range for the measurement of a differential cross section of $\gamma p \to pX(1280)$ up to 5.5 GeV of beam photon energy.

Neither $f_1(1285)$ nor $\eta(1295)$ have been measured in photoproduction that far above their production threshold. In addition to the measurement of the $X(1280)$ it is possible to extract the yield and differential cross section of another enhancement at a mass of $1400\,\text{MeV/c}^2$ whose resonance parameters (m, Γ) are found to be consistent with the $\eta(1405)$.

The differential cross section of the reaction $\gamma p \to p\eta'$ is measured. A comparison with previous measurements reveals a good congruence and strengthens the liability of the applied methods used in this analysis.

8.1 Interpretation of Differential Cross Sections

The differential cross section of the reaction $\gamma p \to p\eta'$ is measured both in depending on the cosine of the polar production angle of the meson in the center-of-mass frame and on the center-of-mass energy.

Furthermore a probabilistic event weight method is applied to remove all of the background.

The shape of those distributions gives us a hint on the underlying processes contributing to the final state. The steep rise in the cross section at forward angles suggests a strong meson exchange t-channel process contributing. Also visible is a smaller rise in backward direction, which can be indicative for a u-channel process. The strength of the u-channel contribution is about an order of magnitude lower than the t-channel contribution. These results are compatible to a large extent to the results published by the CLAS collaboration based on the *g11* run data.

The differential cross sections of the $X(1280)$ and the η' are quite similar in shape, but not in absolute values. Near the production threshold the cross section is almost flat, which hints on $X(1280)$ produced in an s-channel process. With higher energies the t-channel production mechanism increases which is reflected in a steep rise towards forward angles. Unlike the η' cross section the $X(1280)$ distributions show no rise in the backward direction. Due to the lower statistics for the $X(1280)$ in comparison to the η', no final conclusion concerning this behavior can be made.

For the identity of the $X(1280)$ two resonances are possible candidates: either the $f_1(1285)$ or the $\eta(1295)$. The masses of both resonances are close together compared to their

intrinsic width, which makes a differentiation difficult. The quantum numbers of the resonance cannot be determined with this analysis due to large background contributions. The enhancement at an $\pi^+\pi^-\eta$ mass of about $1400\,\mathrm{MeV/c^2}$ might be identified with the $\eta(1405)$. The $\eta(1405)$ has never been measured before in photoproduction experiments or via $\gamma\gamma$ fusion. Based on several predictions the $\eta(1405)$ is discussed as a possible glueball candidate or as a state with gluonic degrees of freedom. It has been measured in so-called "gluon rich" environments only. No strong coupling of glueballs to photons is expected because they are electrically neutral. But glueballs can still be produced in second order processes. Unlike glueballs, states with gluonic degrees of freedom, like hybrids, are allowed to couple to photons as there are quarks present as well. The observation of an enhancement in the $\pi^+\pi^-\eta$ mass, which can be associated with the $\eta(1405)$, might be a hint that the $\eta(1405)$ is no pure glueball. In order to further clarify the nature of the $\eta(1405)$, one has to confirm the existence or non-existence of the $\eta(1295)$ and determine the gluonic content of the $\eta(1405)$.

The differential cross section of the $X(1400)$ is measured and it shows the same structure as the cross section of $X(1280)$. Near the production threshold, a flat distribution appears similar to the η' and $X(1280)$ differential cross sections, referencing an s-channel production mechanism. With increasing energy, an increase in forward direction becomes more and more evident, showing the increasing contribution of t-channel production.

8.2 $f_1(1285)$ or $\eta(1295)$

The enhancement with a mean mass of $1280\,\mathrm{MeV/c^2}$ can be observed in the $\pi^+\pi^-\eta$ mass spectrum. There are two candidate particles which can be associated with this resonance. The first is the pseudoscalar $\eta(1295)$ with $m = 1294 \pm 4\,\mathrm{MeV/c^2}$ and $\Gamma = 55 \pm 5\,\mathrm{MeV}$ reported by the PDG. The vector meson $f_1(1285)$ lies with a mass of $1281.9 \pm 0.5\,\mathrm{MeV/c^2}$ in the same mass region and features a width of $24.2 \pm 1.1\,\mathrm{MeV}$ reported by the PDG.

It is not possible to make an unambiguous statement about the nature of the resonance, but the mass and width of the enhancement can be interpreted in favor of the $f_1(1285)$ which is supported further by the decay angular distribution.

Mass and width of the enhancement at $1280\,\mathrm{MeV/c^2}$ are found to be $m = 1280.1 \pm 0.4\,\mathrm{MeV/c^2}$ and $\Gamma = 36.1 \pm 4.8\,\mathrm{MeV}$. The errors are purely statistical and derived from the fit.

The mass of the $X(1280)$ is in good agreement with the reported mass of the $f_1(1285)$. One has to take into account that the $\eta(1295)$ mass has been averaged from the different values determined by the contributing experiments with an accuracy of only $4\,\mathrm{MeV/c^2}$. Therefore, the mass of $f_1(1285)$ is only 3σ away from the $\eta(1295)$ mass, which makes it extremely difficult to differentiate the two states by mass only.

The intrinsic width of the $f_1(1285)$ has been reported in the range from $19 \pm 5\,\mathrm{MeV/c^2}$ to $55 \pm 18\,\mathrm{MeV/c^2}$ with varying accuracy, while the width of the $\eta(1295)$ has been measured in the range from $53 \pm 6\,\mathrm{MeV/c^2}$ to $66 \pm 13\,\mathrm{MeV/c^2}$ with only three data points. Therefore, we can state that the width of the $X(1280)$ is above the averaged width for the $f_1(1285)$ but well within the range of all measured values. It also is well below the lowest measured width of the $\eta(1295)$.

As another attempt to gain knowledge about the identity of the $X(1280)$, the decay

angular distribution of the $X(1280)$ is extracted and fitted with two hypotheses for either the decay of a pseudoscalar resonance or a vector resonance respectively. The hypothesis of an axial-vector meson decaying to $a_0(980)\pi$ is preferred, although the decay of a pseudoscalar meson cannot be ruled out.

Depending on the measured masses and widths, it is not possible to rule out either the $f_1(1285)$ or the $\eta(1295)$. But with regard to the fitted mass and width the $f_1(1285)$ is more likely. We can state the same for the fits on the decay angle distributions. Due to the high level of background with respect to the signal yield, it is difficult to extract a clean set of events. Nevertheless, the decay angular distributions favor the vector meson hypothesis.

Appendices

Table Differential Cross Section $X(1280) \to \pi^+\pi^-\eta$

W [MeV]	$\cos(\theta_{cm})$	$\frac{d\sigma}{d\Omega}\left[\frac{nb}{sr}\right]$	$\sigma_{stat}\left[\frac{nb}{sr}\right]$	W [MeV]	$\cos(\theta_{cm})$	$\frac{d\sigma}{d\Omega}\left[\frac{nb}{sr}\right]$	$\sigma_{stat}\left[\frac{nb}{sr}\right]$
2400	-0.9	11.6032	5.77756	2900	-0.9	0.789461	0.200199
2400	-0.7	5.82411	0.764506	2900	-0.7	1.0053	0.119574
2400	-0.5	7.69778	0.739502	2900	-0.5	0.925828	0.125317
2400	-0.3	3.84189	0.324283	2900	-0.3	0.703341	0.0943373
2400	-0.1	6.50077	0.285962	2900	-0.1	0.841342	0.0978813
2400	0.1	7.92182	0.32214	2900	0.1	1.67243	0.1042
2400	0.3	8.94779	0.337109	2900	0.3	2.89158	0.148294
2400	0.5	10.4855	0.499599	2900	0.5	4.49196	0.170357
2400	0.7	10.7255	0.716845	2900	0.7	10.8427	0.321401
2400	0.9	2.69316	1.46687	2900	0.9	21.7024	0.625035
2500	-0.9	12.3433	1.55182	3000	-0.9	1.31686	0.358764
2500	-0.7	3.85166	0.357195	3000	-0.7	1.33089	0.217272
2500	-0.5	3.66638	0.280661	3000	-0.5	0.889764	0.180966
2500	-0.3	3.88427	0.215924	3000	-0.3	0.786674	0.130427
2500	-0.1	4.76609	0.221989	3000	-0.1	0.883713	0.11818
2500	0.1	6.46397	0.244082	3000	0.1	1.71402	0.152432
2500	0.3	6.46309	0.226336	3000	0.3	3.43223	0.249251
2500	0.5	10.9062	0.343777	3000	0.5	5.5355	0.243449
2500	0.7	13.8811	0.58232	3000	0.7	15.3237	0.454772
2500	0.9	5.27345	1.12837	3000	0.9	30.0921	1.29538
2600	-0.9	0.787543	0.290701	3100	-0.9	0.800551	0.353131
2600	-0.7	0.974461	0.111874	3100	-0.7	0.976442	0.203601
2600	-0.5	1.09161	0.101888	3100	-0.5	0.771537	0.128944
2600	-0.3	1.14118	0.111811	3100	-0.3	0.559393	0.128793
2600	-0.1	1.56758	0.108151	3100	-0.1	0.411599	0.0966924
2600	0.1	1.43385	0.109337	3100	0.1	1.302	0.126333
2600	0.3	2.22412	0.16492	3100	0.3	2.1764	0.17742
2600	0.5	3.50395	0.155163	3100	0.5	5.08951	0.228295
2600	0.7	3.22021	0.197978	3100	0.7	14.0114	0.41628
2600	0.9	7.94601	0.889171	3100	0.9	31.1235	1.00358
2700	-0.9	0.702442	0.225571	3200	-0.9	0.842126	0.311381
2700	-0.7	0.97634	0.135633	3200	-0.7	0.815588	0.159151
2700	-0.5	1.43444	0.113729	3200	-0.5	0.38363	0.120531
2700	-0.3	1.34331	0.103537	3200	-0.3	0.409728	0.0889874
2700	-0.1	1.35502	0.106854	3200	-0.1	0.3136	0.0785704
2700	0.1	1.69577	0.142514	3200	0.1	0.387869	0.0787731
2700	0.3	2.89295	0.147411	3200	0.3	1.22489	0.122199
2700	0.5	5.02346	0.182492	3200	0.5	2.59436	0.183345
2700	0.7	7.08608	0.225723	3200	0.7	10.2474	0.400631
2700	0.9	11.18	0.703533	3200	0.9	26.1498	0.779023
2800	-0.9	0.807047	0.180468	3300	-0.9	0.759249	0.272877
2800	-0.7	1.2097	0.141875	3300	-0.7	0.550878	0.124821
2800	-0.5	1.04604	0.106405	3300	-0.5	0.202837	0.0796903
2800	-0.3	1.3827	0.108693	3300	-0.3	0.2054	0.0712405
2800	-0.1	1.41855	0.107439	3300	-0.1	0.184588	0.0470849
2800	0.1	1.91672	0.126223	3300	0.1	0.225642	0.0564891
2800	0.3	4.1983	0.175864	3300	0.3	0.508355	0.0786247
2800	0.5	5.24363	0.225429	3300	0.5	1.6763	0.15831
2800	0.7	12.1565	0.344888	3300	0.7	6.32835	0.373938
2800	0.9	18.3367	0.675208	3300	0.9	21.7837	0.705718

Table Differential Cross Sections $X(1400) \rightarrow \pi^+\pi^-\eta$

W [MeV]	$cos(\theta_{cm})$	$\frac{d\sigma}{d\Omega}$ $\left[\frac{nb}{sr}\right]$	σ_{stat} $\left[\frac{nb}{sr}\right]$
2450	-0.9	132.756	18.2598
2450	-0.7	8.62431	6.00243
2450	-0.5	29.6865	4.61511
2450	-0.3	14.6714	4.01102
2450	-0.1	27.6934	3.99416
2450	0.1	29.7307	4.45242
2450	0.3	38.0883	5.1153
2450	0.5	47.5137	5.25954
2450	0.7	14.9775	6.94371
2450	0.9	1.38796	8.48623
2650	-0.9	0.000327653	0.794476
2650	-0.7	1.69765e-05	0.247296
2650	-0.5	9.40595	2.24216
2650	-0.3	18.6794	2.20805
2650	-0.1	14.782	2.24614
2650	0.1	16.4614	2.55811
2650	0.3	3.83776e-06	0.0578239
2650	0.5	60.9051	4.29896
2650	0.7	66.143	4.63536
2650	0.9	40.8119	5.20097
2850	-0.9	9.51278e-05	0.0526525
2850	-0.7	5.52222	3.04211
2850	-0.5	2.93576	2.41306
2850	-0.3	5.31791	2.1336
2850	-0.1	5.45118	2.13719
2850	0.1	10.9563	3.0269
2850	0.3	5.19344	3.51599
2850	0.5	41.368	3.82206
2850	0.7	53.8679	6.2439
2850	0.9	21.227	5.35478
3050	-0.9	6.25382e-06	0.374761
3050	-0.7	4.16943	2.24882
3050	-0.5	5.06668	2.00423
3050	-0.3	3.72529e-06	0.0128944
3050	-0.1	3.00149	1.19957
3050	0.1	2.55447	1.39967
3050	0.3	3.99215	2.25688
3050	0.5	10.8857	2.61194
3050	0.7	43.684	4.11109
3050	0.9	9.47447	4.34086
3250	-0.9	0.758758	5.38537
3250	-0.7	1.11895	2.46355
3250	-0.5	0.280689	1.70177
3250	-0.3	2.96728	1.20778
3250	-0.1	2.26766e-06	0.0111123
3250	0.1	1.1355	1.14923
3250	0.3	0.849316	2.05583
3250	0.5	1.77074	2.53812
3250	0.7	51.9445	4.55549
3250	0.9	74.0293	7.15577

List of Figures

List of Tables

Bibliography

[1] A. Chodos, R. L. Jaffe, K. Johnson, C. B. Thorn, and V. F. Weisskopf. New extended model of hadrons. *Phys. Rev. D*, 9:3471–3495, Jun 1974.

[2] Masaharu Iwasaki, Shin-Ichi Nawa, Takayoshi Sanada, and Fujio Takagi. Flux tube model for glueballs. *Phys. Rev. D*, 68:074007, Oct 2003.

[3] K. A. Olive et al. Review of Particle Physics. *Chin. Phys.*, C38:090001, 2014.

[4] Hai-Yang Cheng, Chun-Khiang Chua, and Keh-Fei Liu. Revisiting scalar glueballs. *Phys. Rev. D*, 92:094006, Nov 2015.

[5] Frank E. Close and Andrew Kirk. The mixing of the $f_0(1370)$, $f_0(1500)$ and $f_0(1710)$ and the search for the scalar glueball. *Physics Letters B*, 483(4):345 – 352, 2000.

[6] Claude Amsler and Frank E. Close. Is $f_0(1500)$ a scalar glueball? *Phys. Rev.*, D53:295–311, 1996.

[7] Donald H. Miller, Suh Urk Chung, Orin I. Dahl, Richard I. Hess, Lyndon M. Hardy, Janos Kirz, and Werner Koellner. $K\overline{K}\pi$ resonance at 1280 mev. *Phys. Rev. Lett.*, 14:1074–1077, Jun 1965.

[8] C. d'Andlau, J. Barlow, and A. M. Adamson. Evidence for a Nonstrange Meson of Mass 1290 MeV. *Phys. Lett.*, 17:347, 1965.

[9] D. Barberis et al. A measurement of the branching fractions of the $f_1(1285)$ and $f_1(1420)$ produced in central pp interactions at 450 GeV/c. *Physics Letters B*, 440(1–2):225 – 232, 1998.

[10] M. Acciarri et al. Light resonances in $K_s^0 K^{\pm}\pi^{\pm}$ and $\pi^+\pi^-\eta$ final states in $\gamma\gamma$ collisions at lep. *Physics Letters B*, 501(1–2):1 – 11, 2001.

[11] N. R. Stanton, P. Brockman, J. A. Dankowych, K. W. Edwards, J. Gandsman, D. Legacey, R. S. Longacre, J. F. Martin, P. M. Patel, A. J. Pawlicki, J. D. Prentice, E. Shabazian, T. S. Yoon, and C. Zanfino. Evidence for axial-vector and pseudoscalar resonances near 1.275 gev in $\eta\pi^+\pi^-$. *Phys. Rev. Lett.*, 42:346–349, Feb 1979.

[12] J. J. Manak and et al Adams. Partial-wave analysis of the $\eta\pi^+\pi^-$ system produced in the reaction $\pi^- p \to \eta\pi^+\pi^- n$ at 18GeV/c. *Phys. Rev. D*, 62:012003, Jun 2000.

[13] A.V. Anisovich, D.V. Bugg, N. Djaoshvili, C. Hodd, J. Kisiel, L. Montanet, A.V. Sarantsev, and B.S. Zou. Resonances in $\overline{p}p \to \eta\pi^+\pi^-\pi^+\pi^-$ at rest. *Nuclear Physics A*, 690(4):567 – 594, 2001.

[14] J. E. Augustin, G. Cosme, F. Couchot, F. Fulda, G. Grosdidier, B. Jean-Marie, V. Lepeltier, G. Szklarz, D. Bisello, G. Busetto, A. Castro, L. Pescara, P. Sartori, L. Stanco, Z. Ajaltouni, A. Falvard, J. Jousset, B. Michel, and J. C. Montret. Partial-wave analysis of dm2 collaboration data in the $\eta(1430)$ energy range. *Phys. Rev. D*, 46:1951–1958, Sep 1992.

[15] P. H. Baillon et al. Further Study of the e-Meson in Antiproton Proton Annihilation at Rest. *Nuovo Cim.*, A50:393–421, 1967.

[16] A Bertin eta al. A search for axial vectors in $p\bar{p} \to \overline{K}^{\pm} K^0_{miss} \pi^{\pm} \pi^+ \pi^-$ annihilations at rest in gaseous hydrogen at ntp. *Physics Letters B*, 400(1–2):226 – 238, 1997.

[17] D. L. Scharre et al. Observation of the Radiative Transition $\psi \to \gamma E(1420)$. *Phys. Lett.*, B97:329, 1980.

[18] Jefferson Laboratory. The jlab picture exchange.

[19] D.I. Sober and et. al. Hall Crannell. The bremsstrahlung tagged photon beam in hall b at jlab. *Nuclear Instruments and Methods in Physics Research Section A: Accelerators, Spectrometers, Detectors and Associated Equipment*, 440(2):263 – 284, 2000.

[20] Steve Christo. The g11a target cell, https://userweb.jlab.org/ christo/g11a

[21] Y.G. Sharabian, M. Battaglieri, V.D. Burkert, R. De Vita, L. Elouadrhiri, et al. A new highly segmented start counter for the CLAS detector. *Nucl.Instrum.Meth.*, A556:246–258, 2006.

[22] B.A. Mecking et al. The CEBAF Large Acceptance Spectrometer (CLAS). *Nucl.Instrum.Meth.*, A503:513–553, 2003.

[23] M.D. Mestayer, D.S. Carman, B. Asavapibhop, F.J. Barbosa, P. Bonneau, et al. The CLAS drift chamber system. *Nucl.Instrum.Meth.*, A449:81–111, 2000.

[24] E.S. Smith et al. The time-of-flight system for clas. *Nuclear Instruments and Methods in Physics Research Section A: Accelerators, Spectrometers, Detectors and Associated Equipment*, 432(2?3):265 – 298, 1999.

[25] G. Adams et al. The clas cherenkov detector. *Nuclear Instruments and Methods in Physics Research Section A: Accelerators, Spectrometers, Detectors and Associated Equipment*, 465(2?3):414 – 427, 2001.

[26] J. T. Goetz. Ξ *Hyperon Photoproduction from Threshold to 5.4 GeV with CEBAF Large Acceptance Spectrometer.* dissertation, University of California Los Angeles, 2010.

[27] M. Amarian et al. The clas forward electromagnetic calorimeter. *Nuclear Instruments and Methods in Physics Research Section A: Accelerators, Spectrometers, Detectors and Associated Equipment*, 460(2–3):239 – 265, 2001.

[28] E. Pasyuk. Energy loss corrections for charged particles in clas. *CLAS-NOTE*, (016), 2007.

[29] g12 run group. G12 procedures. https://clasweb.jlab.org/rungroups/g12/wiki/index.php/, July 2015.

[30] M Williams, M Bellis, and C A Meyer. Multivariate side-band subtraction using probabilistic event weights. *Journal of Instrumentation*, 4(10):P10003, 2009.

[31] J. Ball and E. Pasyuk. Photon flux determination through sampling "out-of-time" hits with the hall b photon tagger. *CLAS-NOTE*, (002), 2005.

[32] C. Bookwalter. *g12 analysis procedures, statistics and systematics.* 2014.

[33] R.Bradford and R.A. Schumacher. Liquid hydrogen density in the g1c clas cryotarget. *CLAS-NOTE*, (003), 2002.

[34] J. Hord R.D. McCarthy and H.M.Roder. Selected properties of hydrogen (engineering design data). *NBS monograph*, 1981.

[35] Michael. C. Kunkel. *Photoproduction of π^0 on Hydrogen with CLAS from 1.1 GeV - 5.45 GeV using $e^+e^-\gamma$ decay.* Dissertation, Old Dominion University, 2008.

[36] F. James and M. Roos. Minuit: A System for Function Minimization and Analysis of the Parameter Errors and Correlations. *Comput. Phys. Commun.*, 10:343–367, 1975.

[37] M. Battaglieri N. I. Kochelev and R. De Vita. Exclusive photoproduction of f1 (1285) meson off the proton in kinematics available at the jefferson laboratory experimental facilities. *Phys. Rev. C*, 80:025201, Aug 2009.

[38] K. Nakayama and H. Haberzettl. Analyzing $\eta^{'}$ photoproduction data on the proton at energies of 1.5˘2.3 gev. *Phys. Rev. C*, 73:045211, Apr 2006.

[39] M Williams et. al. Differential cross sections for the reactions $\gamma p \to p\eta$ and $\gamma p \to p\eta'$. *Phys. Rev. C*, 80:045213, Oct 2009.

List of Acronyms

DAQ Data Acquisition System
EMC Electromagnetic Calorimeter
CEBAF Continuous Electron Beam Accelerator Facility
CLAS CEBAF Large Acceptance Spectrometer
JLab Thomas Jefferson National Accelerator Facility
TASC Total Absorption Shower Counter
TOF Time-Of-Flight
ST Start Counter
TDC Time-to-Digital Converter
ADC Analog-to-Digital Converter
DC Drift Chambers
CC Čerenkov counter
FPGA Field Programmable Gate Array

Acknowledgments

Lebenslauf

Name	Cathrina Sowa
Geburtstag	21.02.1988
Geburtsort	Dortmund
Eltern	Angelika Sowa geb. Manegold Jürgen Sowa

Studium

10.2012–01.2016
Wissenschaftlicher Mitarbeiter an der Ruhr-Universität Bochum
Promotion am Lehrstuhl für experimentelle Hadronenphysik
unter Leitung von Prof. Dr. Ulrich Wiedner
Mitglied der RUB Research School

11.2010–09.2012
Studium der Physik (Master of Science) an der Ruhr-Universität Bochum
Masterarbeit am Lehrstuhl experimentelle Hadronenphysik, Experimentalphysik I
Thema: *Entwicklungen zur Slow-Control des $\overline{P}ANDA$ Systems*

09.2007–11.2010
Studium der Physik (Bachelor of Science) an der Ruhr-Universität Bochum
Bachelorarbeit am Lehrstuhl experimentelle Hadronenphysik, Experimentalphysik I
Thema: *Messung des temperaturabhängigen Dunkelstroms von Vakuum-Photoröhren*

Schulbildung

2000–2007
Städtisches Gymnasium Kamen
Abschluss: Allgemeine Hochschulreife (Abitur)
1998–2000
Heisenberg Gymnasium Dortmund

1996–1998
Dietrich-Boenhoeffer-Schule Dortmund
1994–1996
Harkort-Grundschule Dortmund

Versicherung gemäß § 7 Abs. 2 Nr. 6 PromO 2011

Hiermit versichere ich, dass ich meine Dissertation selbstständig angefertigt und verfasst und keine anderen als die angegebenen Hilfsmittel und Hilfen benutzt habe. Meine Dissertation habe ich in dieser oder ähnlicher Form noch bei keiner anderen Fakultät der Ruhr-Universität Bochum oder bei einer anderen Hochschule eingereicht.

_____

Cathrina Sowa